

J. P. Vuik

Structural Optimization of the Monopile Installation Frame Design

Delft University of Technology



Structural Optimization of the Monopile Installation Frame Design

By

J. P. Vuik

Submitted in partial fulfilment of the
requirements for the degree of

Master of Science

in

CIVIL ENGINEERING

–

STRUCTURAL ENGINEERING TRACK

at the Delft University of Technology,
to be defended publicly on Friday February 23, 2018 at 15:00 PM.

Thesis committee:

Prof. dr. ir M. V. Veljkovic

Ir. R. Abspoel

Ir. M. A. N. Hendriks

Ir. A. Shahbazkhani

Steel- and Composite Structures, TU Delft

Steel- and Composite Structures, TU Delft

Computational Modelling of Structures, TU Delft

Seaway Heavy Lifting B.V.

This thesis is confidential and cannot be made public until February 23, 2021.

An electronic version of this thesis is available at <http://repository.tudelft.nl/>.

Preface

This thesis is the finalization of my master thesis of the study Structural Engineering at Delft University of Technology, faculty of Civil Engineering and Geoscience. The work was performed from June 2017 to February 2018. The objective of this thesis was to obtain a design of the critical section of the monopile installation frame which is optimized for the fatigue load case.

The objective of my thesis would not have been reached without the help of others. I would like to express my sincere gratitude towards my committee members, prof. dr. ir. M. V. Veljkovic, dr. ir. R. Abspoel and dr. ir. M. A. N. Hendriks, for their guidance and support during this master thesis. Additionally, my special thanks go out to ir. A. Shahbazkhani for his daily support and guidance throughout my thesis.

Also, I would like to thank Seaway Heavy Lifting for the opportunity to graduate within the company. I especially would like to thank Martijn Lenting for his help and support with the use of ANSYS. Furthermore, I want to thank all Seaway Heavy Lifting employees and my fellow graduate students for their interest and contribution to my thesis.

Finally I would like to thank my family and friends for their continuous support and patience throughout my time in Delft and during my thesis.

J. P. Vuik

Delft, February 2018

Summary

Wind energy plays an important role in the global energy supply and is obtained by wind turbines placed on- and offshore. The expected growth of offshore wind farms will generate a lot of work in the future. Seaway Heavy Lifting is an offshore company which offers Engineering, Procurement, Construction and Installation (EPCI) solutions worldwide for oil, gas and renewables projects.

Offshore wind turbines are most commonly placed on a monopile foundation. The installation of monopile foundations used for offshore wind turbine farms is the main part of the projects Seaway Heavy Lifting is executing. The installation of monopiles is done using an installation vessel, which needs to be anchored during installation. The anchoring is done in order to cooperate with external forces on the side shell due to the installation of the monopile. The installation of the monopile is done using a frame which is connected to the side shell of the vessel. In order to stay competitive in the business, the company has been doing research to how to decrease the amount of installation time of their projects. It is concluded that profit can be gained by reducing the necessary time to anchor the installation vessel.

To install monopiles without anchoring the vessel, the monopile installation frame (MIF) was designed. The MIF can be placed onto the seabed after which the monopile can be hoisted inside of the frame. The frame will support the monopile during hammering. No external forces will be acting on the side shell of the vessel when using the MIF during hammering, which rules out the need for anchoring the vessel. Instead of anchoring, dynamic positioning will be used. Since the installation of monopiles will occur in different water depths, the MIF needs to be modular. An extension piece will be used in order to change the height of the frame.

The goal of this thesis is to obtain a structural optimized design of the MIF. The connections needed to connect and disconnect the extension piece are critical sections of the MIF. During the lifetime of the MIF, fatigue due to waves, wind and current loading will play a role. Therefore, this thesis has focused on the structural optimization of the connection with respect to fatigue loading. A bolted flange connection will be used in order to connect the members, which will be machined and then welded to the tube end. An initial geometry of the connection was designed with help of design rules stated by ir. M. Seidel.

The finite element program ANSYS will be used for the calculation of stress distributions. The decision was made to verify ANSYS, which was done by studying the accuracy of ANSYS, its way

of working and to get used to the program. The verification has been done using a reference project.

The fatigue analysis of the connection started first of all with a global load analysis. This was done with help of the program SACS, which uses wave heights and wind speeds together with currents data as input. A calculation model of the MIF was built in SACS. Once the input was completed, the internal forces of the MIF were calculated. The global load analysis is necessary in order to obtain the loads in the members that will be connected by the bolted flange connection. These loads were used as input for ANSYS.

To check whether the initial design could be used as a starting point, the 3 failure modes of a bolted flange connection have been explained and verified for the initial design. Once it was verified, it was used as input in ANSYS in order to study the stress distribution of the model. The initial geometry has a negligible radius between the tube and the flange of the connection. Therefore, it was expected that a high concentration of stresses would occur in the junction between the tube and the flange of the connection. In order to find the stress concentration factor (SCF) in this junction, the maximum stress occurring in the junction needs to be divided by the stress applied to the tube.

Once the SCF was known the fatigue analysis could be performed. The fatigue analysis was done for two details: the junction between the tube and the flange and the welded connection between the tube and the machined part. Firstly, the amount of actual cycles was calculated for a certain time period with help of the wave scatter diagram, after which the corresponding stress ranges during these cycles was obtained. The stress ranges were multiplied with the SCF for the tube-to-flange junction, the SCF was obtained using ANSYS. Once the stress ranges were known, the amount of cycles until failure was calculated using S-N-curves that fit the two studied details. The actual damage to the structure was determined by dividing the actual number of cycles happening by the amount of cycles until failure. With the damage known for a certain time period, the life time of the structure was calculated.

The MIF will be used for a period of more or less 8 years, so the design lifetime was set at 9 years. The initial geometry had an extremely low lifetime. Therefore, the connection needed to be optimized in order to improve the lifetime. The optimization of the connection was done by increasing the radius of the tube-to-flange junction to lower the SCF. A lower SCF value resulted in a longer lifetime. The design has been optimized until an optimum radius of 36 mm was found. The final design has a lifetime of 9 years.

Table of Contents

Preface	3
Summary	4
Table of Contents	6
List of Figures	10
List of Abbreviations	12
1 Introduction.....	13
1.1 Seaway Heavy Lifting	13
1.2 Objective	14
1.3 Research Questions	14
1.4 Approach.....	14
2 Background Information.....	16
2.1 Wind Energy.....	16
2.1.1 Global.....	16
2.1.2 European Union.....	16
2.1.3 Expected Growth European Union.....	17
2.2 Offshore Wind Energy	18
2.2.1 General Background.....	18
2.2.2 Different Foundations Offshore Wind Turbines	19
2.2.3 Monopiles in Offshore Industry	20
2.2.4 Procedure of Installation Monopiles	21
2.2.5 Reduction of Installation Time.....	23
2.2.6 Stationkeeping of Heavy Lift Vessel on Dynamic Positioning.....	23
2.2.7 Installation of Monopiles on Dynamic Positioning	24
2.3 Monopile Installation Frame.....	28
2.3.1 General Introduction	28
2.3.2 Design Requirements MIF	29
2.3.3 Built-Up MIF	29
2.3.4 Transportation and Installation MIF.....	31
2.4 Introduction to Thesis Subject.....	33
2.4.1 General Introduction	33

2.4.2	Critical Section MIF	33
3	State of Art Bolted Flange Connection	35
3.1	Introduction Bolted Flange Connection	35
3.1.1	Statically and Dynamically Loaded Bolted Flange.....	36
3.1.2	Failure Modes Bolted Flange Connection	38
3.2	Fatigue Behavior Bolted Flange Connection	39
3.2.1	Welded Bolted Flange Connection.....	39
3.2.2	Machined Bolted Flange Connection	40
3.2.3	Fatigue Behavior Bolt	41
3.2.4	Geometry Characteristics Bolted Flange.....	42
4	Verification ANSYS.....	44
4.1	Introduction.....	44
4.2	Verification Model	44
4.2.1	Geometry.....	44
4.2.2	Mesh Settings.....	45
4.2.3	Stress Concentration Factor	46
4.3	Comparison of Stress Concentration Factors.....	48
5	Structural Optimization.....	49
5.1	Introduction.....	49
5.2	Flowchart Optimization Process.....	50
6	Global Load Analysis	51
6.1	Types of Loading MIF	51
6.1.1	Dead Loads	51
6.1.2	Environmental Loads	51
6.2	Load Scenarios.....	52
6.2.1	Ultimate Load Case	53
6.3	Hydrodynamic Loads	54
6.3.1	Wave Loads	54
6.3.1.3	Determination of Wave Loads	56
6.3.2	Morison's Load Formula	58
6.3.3	Currents Loads	59
6.4	Wave Breaking	59
6.5	Wave Slamming	60
6.6	Wind Loads	61
6.7	Load Combinations.....	62
6.8	Loads Applied on the Connection	63

7	Verification Failure Modes	64
7.1	Initial Geometry	64
7.2	Failure Modes Bolted Flange Connection	65
7.2.1	Failure Modes A, B and C.....	65
7.2.2	Failure Modes D and E	68
8	Fatigue Lifetime	71
8.1	Introduction.....	71
8.2	Structural Detail Category.....	72
8.2.1	Derivation Structural Detail Category Tube-to-Flange Junction.....	73
8.2.2	Structural Detail Category Tube-to-Tube Connection.....	76
8.3	Stress Concentration Factor	77
8.4	Wave Scatter Diagram.....	82
8.5	Actual Cycles.....	83
8.6	Stress Ranges	83
8.7	Cycles to Failure.....	84
8.8	Damage and Lifetime.....	85
8.9	Optimization Fatigue Lifetime	86
8.10	Validation Failure Modes Final Model	88
8.10.1	Geometry Final Design	88
8.10.2	Material Properties	89
8.10.3	Calculation Ultimate Force.....	89
8.10.4	Verification Final Design	91
9	Results and Discussion.....	93
9.1	Results	93
9.1.1	Geometry Final Design	93
9.1.2	Fatigue Life Time.....	94
9.1.3	Failure Modes.....	95
9.2	Discussion	95
10	Conclusions and Recommendations	96
10.1	Conclusions	96
10.2	Recommendations.....	97
11	Bibliography	99
12	Appendix	104
12.1	Design Loads MIF	104
12.1.1	Variable Loads.....	104
12.1.2	Wave Loads	104

12.1.3	Morison's Load Formula Parameters	107
12.1.4	Wind Loading	112
12.1.5	Lifting and Positioning Dynamic Loads	112
12.1.1	Load Combinations.....	114
12.1.2	Load Combinations.....	115
12.2	Model Verification	116
12.2.1	Chabrolin and Ryan.....	116
12.3	ANSYS Model Details.....	116
12.4	Failure Modes.....	117
12.4.1	Validation Failure Modes Initial Geometry.....	117
12.5	Fatigue Analysis	121
12.5.1	SCF Refinement.....	121
12.5.2	Wave Scatter Diagram.....	124
12.5.3	Equivalent Wave Heights and Periods.....	125
12.5.1	Example Calculation Lifetime.....	125

List of Figures

Figure 4-1 - Global Cumulative Installed Wind Capacity 2001 – 2016 [7].....	16
Figure 4-2 - Wind Energy On- and Offshore in European Union [7].....	17
Figure 4-3 - Water Depths and Distances to Shore of European Wind Farms [7].....	18
Figure 4-4 – Offshore Wind Turbine on Monopile Foundation [85].....	19
Figure 4-5 - Different Foundations: Monopile, Tripod, Tripile, Jacket [58].....	19
Figure 4-6 –Types of Foundations [7]	20
Figure 4-7 - Gravity Based Foundation [88]	20
Figure 4-8 - Floating Foundation [89].....	20
Figure 4-9 - Upending Cradle and the Outrigger [53]	21
Figure 4-10 - Hydraulic Arm with Roller Head [56]	22
Figure 4-11 – Duration Times for Different Activities [57]	23
Figure 4-12 - Dynamic Positioning System [66].....	24
Figure 4-13 - Concept Design for Compensated Outrigger [51]	25
Figure 4-14 – Vibro-hammer on Crane Hook [54]	26
Figure 4-15 – Preliminary Design of Monopile Installation Frame [20].....	27
Figure 4-16 – Preliminary Design of Monopile Installation Frame [20].....	28
Figure 4-17 – Monopile Gripper [20]	30
Figure 4-18 - Lifting of Monopile Installation Frame [20].....	31
Figure 4-19 – Installation Step-by-Step [20].....	32
Figure 4-20 - Integrated Noise Mitigation System [20]	32
Figure 4-21 - Members to be Connected by Bolted Flange Connections	34
Figure 5-1 - Bolted Flange Connection with Fastening Tool [22]	35
Figure 5-2 - Stress Transmission in Case of Compression	36
Figure 5-3 - Stress Transmission in Case of Tension.....	36
Figure 5-4 - Statically Loaded Bolted Flange Connection.....	37
Figure 5-5 - Dynamically Loaded Bolted Flange Connection.....	37
Figure 5-6 - Failure Mode A [24]	38
Figure 5-7 - Failure Mode B [24]	38
Figure 5-8 - Failure Mode C [24]	39
Figure 5-9 - Welded Tube-to-Flange Connection	40
Figure 5-10 - Machined tube-to-Flange Connection	41
Figure 5-11 - Bolted Flange Position [24].....	42
Figure 5-12 - Geometry Characteristics Bolted Flange [24].....	42
Figure 6-1 – Side View Bolted Flange Connection	44
Figure 6-2 - Mesh of Model Reference Project [25].....	45
Figure 6-3 - Mesh of Verification Model	45
Figure 6-4 - Stress Distribution in the Verification Model.....	46
Figure 6-5 – Values of Stresses in the Tube-to-Flange Junction	46
Figure 6-6 - Stresses per Point as given in Figure 6-5	47
Figure 7-1 - Flowchart Optimization Process	50
Figure 8-1 - Load Scenarios.....	53
Figure 8-2 - Ranges of Validity for Various Wave Theories [30]	57
Figure 8-3 – Direction of Environmental Load Conditions Acting on the MIF	62

Figure 8-4 - Evaluated Members.....	63
Figure 9-1 - Failure Mode A [24]	65
Figure 9-2 - Failure Mode B [24]	66
Figure 9-3 - Failure Mode C [24]	68
Figure 9-4 - Failure Mode D [24]	69
Figure 9-5 - Failure Mode E [24]	70
Figure 10-2 - Junctions of the Connection.....	72
Figure 10-1 - Machined Part	72
Figure 10-3 - Structural Detail Category 160 [36].....	73
Figure 10-4 - Structural Detail Category 140 [36].....	73
Figure 10-5 - Surface Roughnesses per Modification Process.....	75
Figure 10-6 - Structural Detail Category 71 [36].....	76
Figure 10-7 - Locations Connection Members	77
Figure 10-8 - Pressure Applied to the Model in ANSYS	78
Figure 10-9 - Stress Distribution for Tensile Loading	79
Figure 10-10 - Stress Distribution for Tensile Loading – Radius Tube-to-Flange Junction	80
Figure 10-11 - Influence of Mesh Refinement on SCF- Tension.....	81
Figure 10-12 - Influence of Mesh Refinement on SCF - Compression	82
Figure 10-13 - Stress Ranges (MPa)	84
Figure 10-14 - S-N-Curves [36].....	85
Figure 10-15 - Geometry Details.....	86
Figure 10-17 - Influence SCF - Tension on Lifetime.....	87
Figure 10-16 - Influence Radius on Stress Concentration Factor	87
Figure 11-1 - Geometry Characteristics Bolted Flange Connection [24].....	93
Figure 11-2 - Geometry Final Design	94
Figure 13-1 - Ranges of Validity for Various Wave Theories [30].....	106
Figure 13-2 - Drag Coefficient for Fixed Circular Cylinder for Steady Flow in Critical Flow Regime for Various Roughnesses [30].....	110
Figure 13-3 - Heave and Pitch [62]	112
Figure 13-4 - Stress Distribution with Element Size of 5 mm.....	121
Figure 13-5 - Stress Distribution with Element Size of 1.25 mm.....	122
Figure 13-6 - Stress Distribution with Element Size of 2.5 mm.....	122
Figure 13-7 - Stress Distribution with Element Size of 0.625 mm.....	123
Figure 13-8 - Wave Scatter Diagram.....	124

List of Abbreviations

T&I	= Transport and Installation
EPCI	= Engineering, Procurement, Construction and Installation
MIF	= Monopile Installation Frame
SCF	= Stress Concentration Factor
FEM	= Finite Element Method
WT	= Wind Turbine
OWT	= Offshore Wind Turbine

1 Introduction

This chapter states a company profile after which the objective of the thesis, the research questions and the approach will be stated and explained.

1.1 Seaway Heavy Lifting

Seaway Heavy Lifting is a leading offshore contractor in the global Oil & Gas and Renewables industry offering tailored Transport and Installation (T&I) and Engineering, Procurement, Construction and Installation (EPCI) solutions. Seaway Heavy Lifting operates globally focusing on the North Sea, Mediterranean, America's, Africa, Asia Pacific and Middle East. In the last years, Seaway Heavy Lifting has become increasingly active in the renewables industry. Their expertise is based on more than 150 successfully executed oil and gas installation projects, from the North Sea and Black Sea to the Gulf of Mexico, Barents Sea, Malaysia and offshore India.

Seaway Heavy Lifting offers EPCI services for wind farm foundations, mostly monopiles, for the renewable energy industry worldwide. Following the consolidation of parent company Subsea 7's renewable energy business into Seaway Heavy Lifting, they now undertake major offshore wind projects on an EPCI basis. In addition, they also offer a full marine service, from T&I of foundation structures to cable installation, wind turbine generator installation and overall project management.

The company owns and operates two heavy lift vessels: Stanislav Yudin and Oleg Strashnov. The lift capacities of these vessels are respectively 2500 Mt and 5000 Mt. In addition to these vessels, Seaway Heavy Lifting owns high quality support equipment, including rigging, hammers and a wide variety of pile handling tools. Currently, the company has the capacity to install over 250 Wind Turbine Generators annually. [1]

The main part of the projects that Seaway Heavy Lifting executes consists of the installation of monopiles. The installation is done by one of the heavy lift vessels. During the installation, the vessel needs to be anchored after which the monopile can be placed in a frame connected to the side shell of the vessel. When the monopile is inside of the frame, it can be hammered into the soil. In order to stay competitive in the business, Seaway Heavy Lifting has been doing research to how they can decrease the duration of the installation process.

It has been concluded that the installation duration can be drastically decreased if the vessel doesn't have to be anchored during the installation process. This has as result that the installation process will be done using the MIF. The MIF will be placed onto the seabed after which a monopile

will be placed inside of the MIF. Once the monopile is inside of the MIF, it can be hammered into the soil. The MIF will be a modular structure that will be used in different water depths. The height of the MIF can be changed by the use of an extension piece that can be connected and disconnected relatively easy.

1.2 Objective

The objective of this thesis is to obtain a design of the critical section of the MIF which is optimized for the fatigue load case. This design will be obtained taking into account both static and cyclic loads.

1.3 Research Questions

The following questions will be answered throughout the thesis in the respective chapters:

Chapter 7 - Verification Failure Modes

- Which failure mode of the three known failure modes for bolted flange connections is governing?

Chapter 8 - Fatigue Lifetime

- What is the influence of the mesh size on the accuracy of the SCF?
- How does the SCF influence the design of the bolted flange with respect to the fatigue life of the flange?

1.4 Approach

First of all, chapter 2 focuses on background information regarding the thesis and the subject of this thesis. The background information gives an introduction to the wind energy market in general and the offshore wind energy market in more detail. Also, the subject of the thesis is introduced more detailed after which an elaborate description of the MIF is given.

Chapter 3 is a state of the art of steel-to-steel connections in general and bolted flange connections in detail. In the state of art, an introduction is given for bolted flange connections together with the theory used in the thesis to obtain an initial geometry. Besides, the distribution of stresses through a bolted flange is explained. To derive the stress distribution in the critical section of the MIF, a numerical model in ANSYS is made.

Chapter 4 focuses on the verification of ANSYS. The verification was done by remodeling a stated model given in a reference project. Then, the same properties and loads have been applied to the model after which the results have been compared to the results of the reference project. Once the comparison between the given results and the calculated results in ANSYS was satisfying, the verification was completed.

Chapter 5 explains the structural optimization which is done in the chapters that follow. For the structural optimization, first of all the load cases and load scenarios are given and explained in the global load analysis in chapter 6. Also, the theory behind the different types of loading is explained.

In order to reach the proposed objective, an initial geometry was obtained in chapter 7, after which this initial geometry was verified with respect to the three failure modes for bolted flanges. In this manner, the governing failure mode was determined. The initial geometry was verified to be sure it meets the design requirements. Once this was verified, the initial geometry was used as a starting point for the fatigue analysis.

Chapter 8 focuses on the determination and the optimization of the fatigue life for the flange of the connection. First of all, the structural detail classes were determined, which stated the S-N-curve for the fatigue analysis. Then, the stress concentration factor in the radius of the tube-to-flange joint of the initial geometry was obtained using ANSYS. Also, the influence of the mesh size on the values of the SCF has been researched.

With help of the wave scatter diagram the number of actual cycles is determined as well as the equivalent wave heights and equivalent wave periods. The stress ranges that occur in the members during these equivalent wave height and periods have been found using the equivalent wave heights and periods as input in SACS. The maximum occurring stress ranges were used to find the amount of cycles to failure. With the number of actual cycles and the number of cycles to failure known, the damage for a certain time period has been calculated, which determines the life time.

The life time has been optimized by lowering the SCF, which was done by increasing the radius of the tube-to-flange junction. The optimization resulted in an optimum value for the radius of 36 mm. Both the influence of the radius on the SCF and the influence of the SCF on the lifetime of the tube-to-flange junction have been researched.

2 Background Information

This chapter contains an introduction to the thesis subject. First of all, the wind energy market is discussed which is followed by a discussion of the role of offshore wind energy. A brief introduction to the monopile installation frame is given in section 2.3 which is followed by an introduction to the subject of this thesis is given in 2.4.

2.1 Wind Energy

Wind energy plays an important role in the global energy supply and its role is still growing, see Figure 2-1. The technology of using wind as an energy source made its first steps centuries ago. Development of this technology took place in the last century, leading to a rapid grow of the world's wind power generation capacity in the last decade.

2.1.1 Global

Globally, the total renewable capacity in 2016 was 1849 GW of which 487 GW consisted of wind energy. [2] During 2016, the growth of cumulative capacity was approximately 13%. The growth of the global cumulative capacity is expected to continue during the period 2017 - 2021 with an average of 11%. [3]

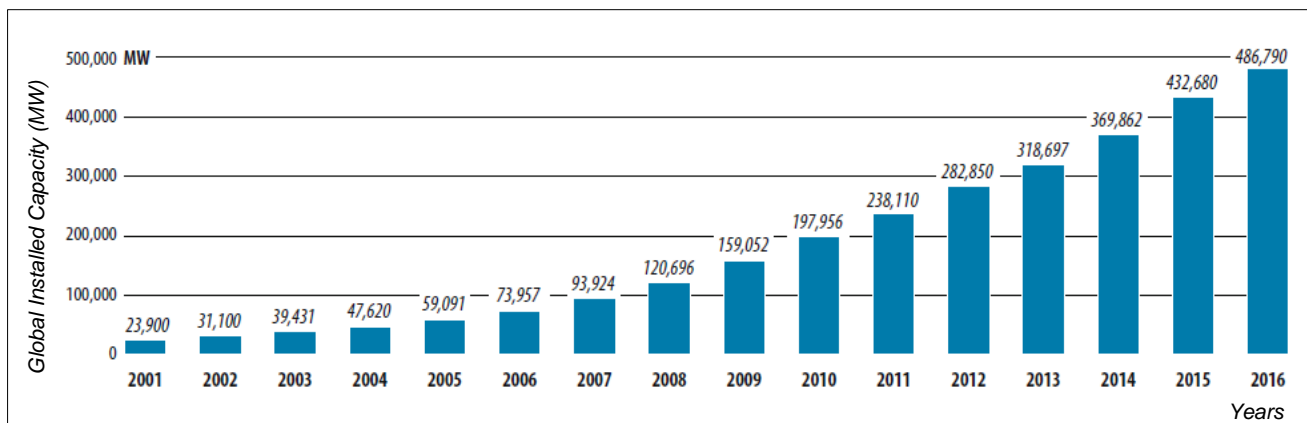


Figure 2-1 - Global Cumulative Installed Wind Capacity 2001 – 2016 [7]

2.1.2 European Union

The European Union has a significant share in the global installed wind capacity. One of the driving forces in Europe behind the promotion and development of sustainable energy supply is the European Wind Energy Association, now WindEurope. [4]

2 - Background Information

At the end of December 2016, the European Union had installed 32% of the global cumulative installed wind capacity. This installed capacity was both installed offshore, 12%, and onshore, 88%. [3] The growth of installed wind capacity is partly caused by an in 2014 set target of the European Union. The target is to have 27% of the total energy consumption covered by renewable energy in 2030. [5] Wind energy will contribute the most to this percentage, with a share of at least 21%. [6]

2.1.3 Expected Growth European Union

The growth of wind energy on- and offshore is given in Figure 2-2. Due to new investments, the growth of the offshore installed capacity is expected to continue at least until 2018. After 2018, the number of projects will fall due to the finish of the National Renewable Energy Action Plans (NREAPs) of European member states. These NREAPs were made under the current Renewable Energy Directive for a period up to 2020. By 2020 the total European offshore wind capacity is expected to be 24.6 GW. [7] It is expected that the growth of offshore wind farms will continue after 2018 due to technical developments and rapid decreasing installation costs of offshore wind farms. [8]

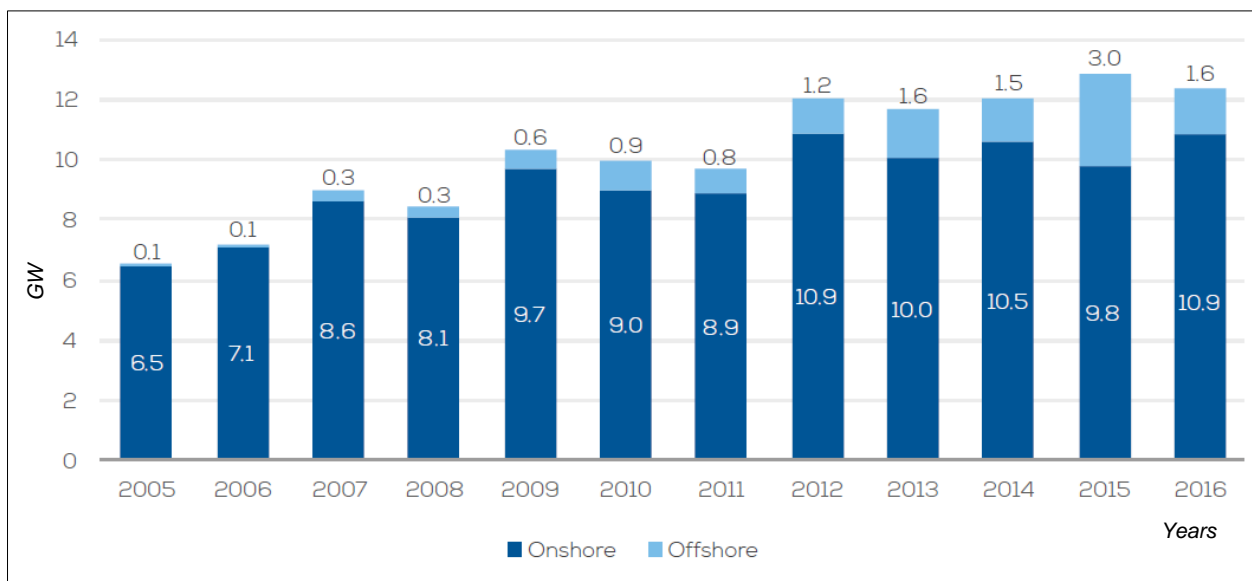


Figure 2-2 - Wind Energy On- and Offshore in European Union [7]

2.2 Offshore Wind Energy

Since onshore space for windfarms becomes scarce, the design and installation of offshore windfarms has become an increasingly attractive option. Due to investments and technical developments, an increase of offshore wind farm projects is expected. WindEurope expects that offshore wind will produce 7% to 11% of the European Union's electricity demand by 2030. [9]

2.2.1 General Background

Offshore wind energy has advantages over onshore wind energy. Due to stronger winds offshore, the productivity is higher compared to onshore wind farms. Also, issues of visual impact and noise can be eliminated by installing wind farms offshore. This elimination of issues makes it possible to use different designs for the wind turbines in order to increase their efficiency.

However, some disadvantages can be named. Maintenance or repair issues take longer to be solved due to bad accessibility of windfarms and are therefore more costly. Improving the accessibility of wind farms can decrease the costs for maintenance or repairs. Besides, the offshore conditions require higher investments in towers, foundations and underwater cabling. These offshore conditions also result in a more difficult and expensive installation of the windfarms. Improving the installation conditions and installation time will improve the profitability of the windfarms. [10]

In 2016, the European offshore wind industry has installed in total 1558 MW of new capacity, 338 offshore wind turbines in six windfarms. The average water depth of the European offshore wind farms was 29.2 meters and the average distance to shore of the projects was 43.5 kilometers; see Figure 2-3.

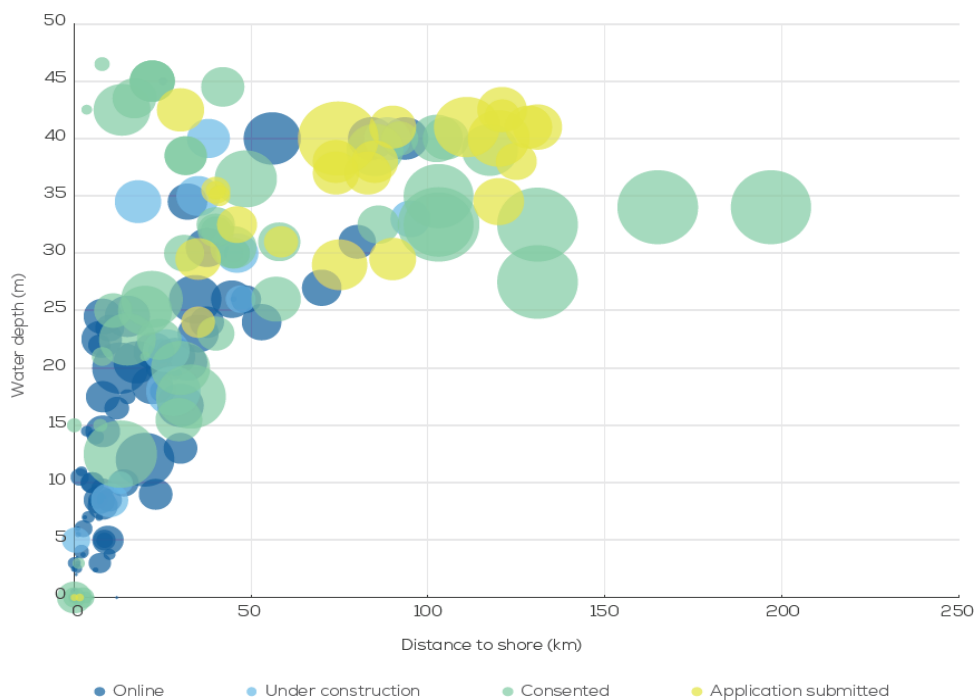


Figure 2-3 - Water Depths and Distances to Shore of European Wind Farms [7]

2.2.2 Different Foundations Offshore Wind Turbines

The built-up of an offshore wind turbine is given in Figure 2-4 and exists of a wind turbine, a transition piece and a monopile foundation. Different foundations can be used depending on the depth in which the wind turbines are placed, see Figure 2-5. The wind turbine is connected to the foundation with help of a transition piece, visible in Figure 2-4. After placing the transition piece on the foundation, the connection between foundation and the transition piece is grouted.

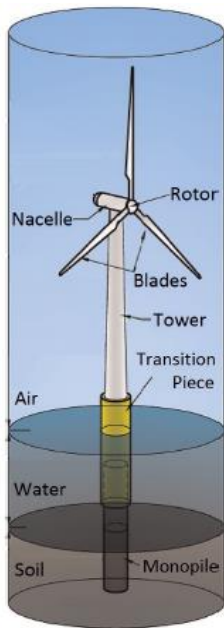


Figure 2-4 – Offshore Wind Turbine on Monopile Foundation [85]

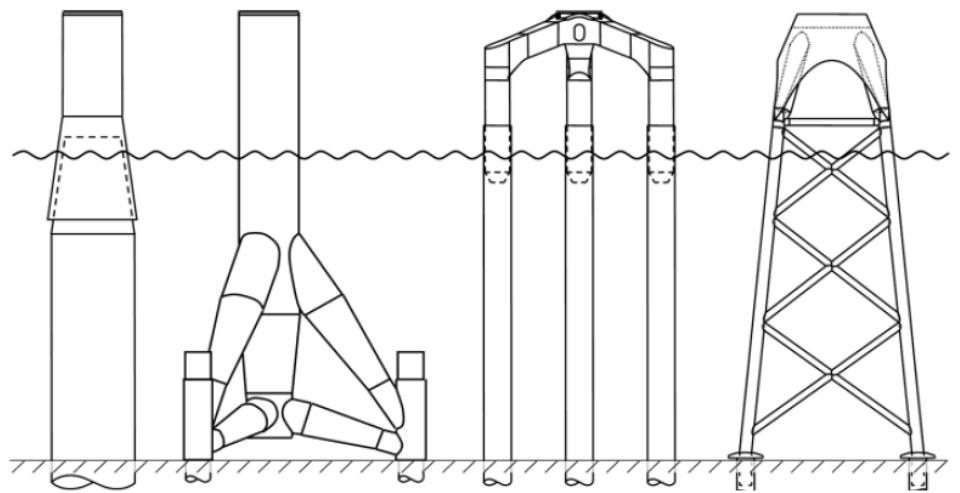


Figure 2-5 - Different Foundations: Monopile, Tripod, Tripile, Jacket [58]

2.2.3 Monopiles in Offshore Industry

The focus in this thesis will be on the monopile foundation and its installation, since the monopile foundation is at the moment the most popular foundation in the offshore industry. As can be seen in Figure 2-6 almost 81% of the used foundations in 2016 were monopiles. The monopile, tripod, tripile and jacket foundations have been displayed in Figure 2-5. The gravity based foundation is shown in Figure 2-7 and the floating foundation in and Figure 2-8.

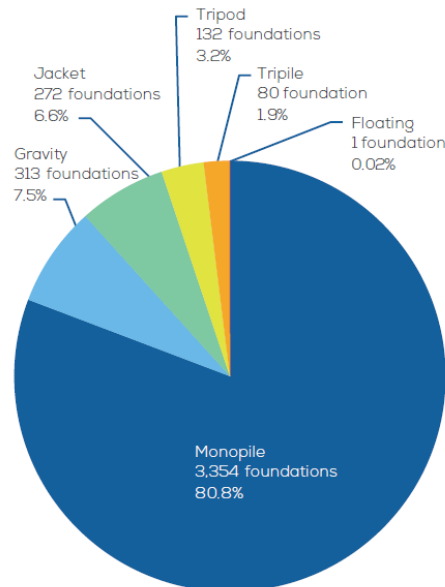


Figure 2-6 –Types of Foundations [7]

The design of monopiles is simple and therefore easy and relatively cheap to manufacture a series of monopiles compared to other used foundations. Besides, monopiles can be installed in almost all kinds of soil, due to the used installation techniques and shape of the monopile. However, a disadvantage of monopiles is that for greater depths monopiles are less profitable, due to larger amounts of steel and more complex installation procedures. [11]



Figure 2-7 - Gravity Based Foundation [88]



Figure 2-8 - Floating Foundation [89]

2.2.4 Procedure of Installation Monopiles

A component of Seaway Heavy Lifting's work is the transport and installation of monopiles and the transition pieces. The transport and installation process exists of several steps which will be discussed in the following sections.

2.2.4.1 Transportation and Arrival

The monopiles and the transition pieces have to be transported to the offshore location by a heavy lift vessel. The monopiles are stored horizontally in a frame and the transition pieces are vertically stored on the deck of the vessel. The sailing routes and duration of the transport are dependent of the weather forecast. It could also be possible the vessel needs to seek shelter, which happens in case of storms. This means the vessels sails back to the harbor. This decision will be made using the weather forecast. [12]

When the vessel arrives at the offshore location, it needs to be anchored. Both vessels, Oleg Strashnov and Stanislav Yudin, use an 8-point mooring system. The execution of the anchoring is done by two Anchor Handling Tugs (AHTs). The AHT drops the anchor at a designated location, after which the anchor wire is tightened by winches on the heavy lift vessel. [13]; [14]



Figure 2-9 - Upending Cradle and the Outrigger [53]

2.2.4.2 Installation of Monopiles

After anchoring the vessel, the installation of the monopiles starts. To install the monopiles they first have to be positioned in a frame, in order to lift them into an almost vertical position. This frame is further referred to as 'upending cradle'. The upending process with the cradle will be done with help of an upending tool. The upending process is displayed in Figure 2-9. After the upending of the cradle, the monopile will be hoisted out of the cradle into an opened outrigger which is located on the outer side of the vessel, see Figure 2-9. The outrigger is used to ensure the stability and the required verticality of the monopile during installation. [12]

The outrigger is a steel frame with a hinged door and it houses all necessary equipment to handle monopiles. The outrigger door is closed when the monopile is inside after which hydraulic arms inside the outrigger clamp the monopile to keep it in place, see Figure 2-9. When the outrigger door is closed, the hoisting equipment can be removed. After removal of the equipment, the monopile is hammered into the soil to the final penetration depth by a hydraulic hammer.

The verticality of the monopile during hammering is checked with help of measuring systems. On the inside of the outrigger, horizontal hydraulic arms are installed on which at each end a roller head is present. These roller heads transfer loads from the hydraulic arms to the monopiles in order to correct the verticality of the monopiles during hammering when necessary, see Figure 2-10. The hydraulic arms inside of the outrigger are controlled manually. The maximum allowed inclination of the monopile is 0.5° . [15] After an inspection of the installed monopile, the installation is completed.



Figure 2-10 - Hydraulic Arm with Roller Head [56]

2.2.5 Reduction of Installation Time

To get an insight in the duration of the installation process of monopiles and transition pieces, the average time used for anchoring, installation of the monopiles and the transition pieces, grouting of the connection and for picking up the anchors installation durations of Seaway Heavy Lifting's 'Sheringham Shoal' project is used, see Figure 2-11. During the 'Sheringham Shoal' project, 66 monopiles, 71 transition pieces and 2 substation topsides were transported and installed by Seaway Heavy Lifting.

The duration of running and picking up of the anchors takes approximately 43% of the total duration of installation; see Figure 2-11. Therefore, the most time-winning option is to avoid the use of anchors during the installation process.

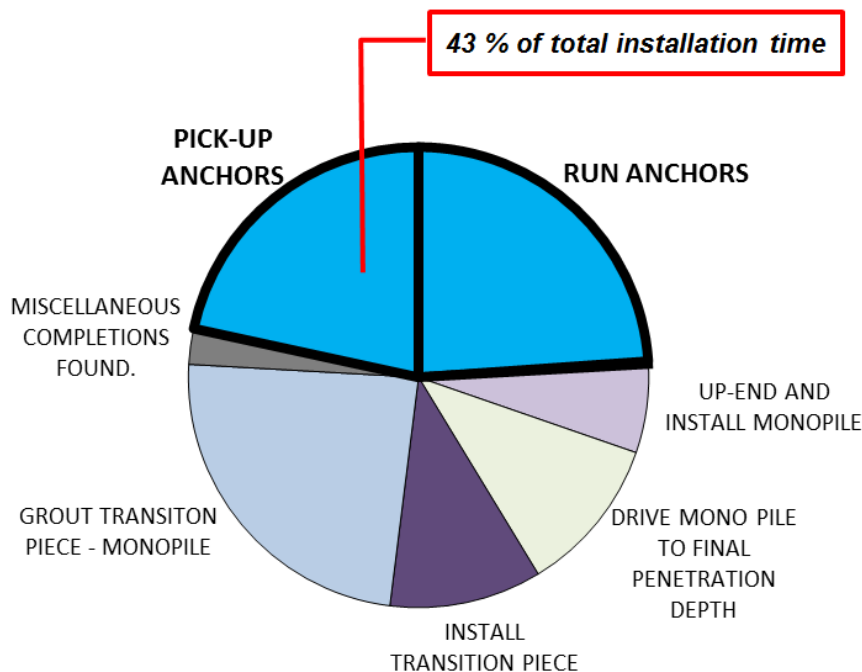


Figure 2-11 – Duration Times for Different Activities [57]

2.2.6 Stationkeeping of Heavy Lift Vessel on Dynamic Positioning

During the installation of monopiles, the heavy lift vessel has to maintain its position to be able to execute the installation activities. In case the vessel is not anchored, Dynamic Positioning is used to ensure the vessel's position. The dynamic positioning system is a computer controlled system that maintains the vessel's position automatically by using the propellers and thrusters of the vessel; see Figure 2-12. The system instructs almost instantly the thrusters to react to wind speed changes and wind direction changes, but changes of the current force are updated relatively slowly.

2 - Background Information

The necessary information for dynamic positioning is provided by, amongst other things, reference sensors, wind sensors, motion sensors and gyrocompasses. [16] The DP-3 system needs a minimum water depth of around 20 meters. When the monopiles are getting bigger, this minimum required depth should be taken in to account.

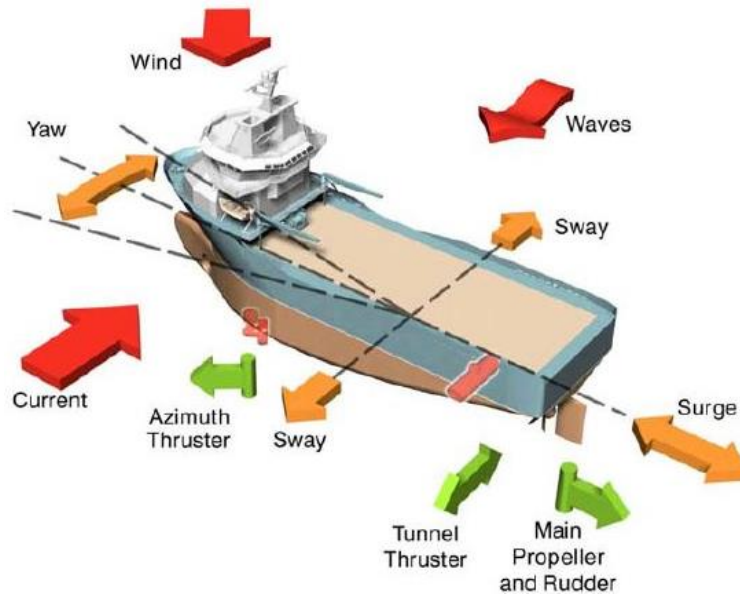


Figure 2-12 - Dynamic Positioning System [66]

The heavy lift vessel 'Oleg Strashnov' is equipped with a DP-3 system, which means that the system provides automatic and manual positioning and heading control under specified maximum environmental conditions, during and following any single fault, including the loss of a compartment due to fire or flood. [17]

2.2.7 Installation of Monopiles on Dynamic Positioning

An important issue to take into account when looking at different installation options is that monopiles aren't stable at self-penetration depth. This means that the installation option is required to:

- Keep the monopile stable during the installation process
- Ensure that the monopile's inclination is within the required limits at final penetration depth (0.5°). [18]

With these requirements taken into account, three different ways of installing monopiles on dynamic positioning can be distinguished:

1. Installation of monopiles with the use of a smart outrigger (comparable to current method)
2. Installation of the monopiles by using the crane of the heavy lift vessel and vibration hammer
3. Installation of monopiles with a Monopile Installation Frame (MIF) [18]

Installation with Smart Outrigger

One of the three possibilities is to continue the installation of monopiles with the outrigger as is done now, but on dynamic positioning instead of using anchors. There are a few challenges the dynamic positioning system has to face during this type of installation. When the monopile is placed inside of the outrigger, it generates an external load on the side shell of the vessel. When the monopile is lowered into the seabed, it attracts large current forces. During this installation, a smart outrigger will be used which is able to correct the monopile's inclination automatically when necessary.

Some dynamic positioning systems, for instance the systems used on pipe-lay vessels, have 'external force compensation'. This enables the dynamic positioning system to recognize the presence of external loads. However, at the moment this function is not available yet at the 'Oleg Strashnov'. The dynamic positioning system will most likely not be able to work with the external load due to the monopile. Hence, this installation option is not possible yet, but it is a promising option.

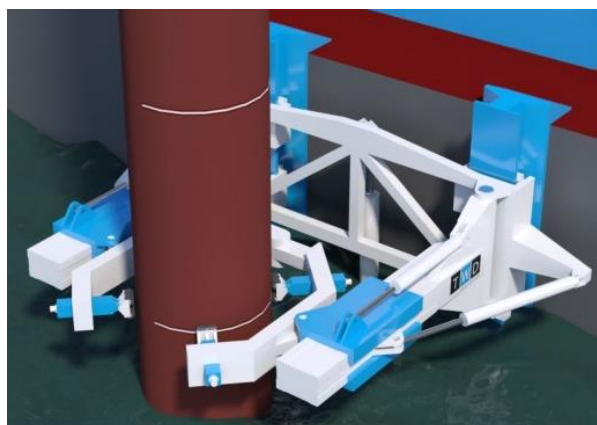


Figure 2-13 - Concept Design for Compensated Outrigger [51]

If adjustments are made to the dynamic positioning system, the above stated problems could be solved. One option to improve the response of the dynamic positioning system is to add 'external force compensation' software to the dynamic positioning system. Another option could be to measure the forces on the outrigger and feed them back to the system, which could improve the system response time. This option needs a lot of research and testing before it can be executed offshore. Also, in order to be able to correct the monopile's inclination, the outrigger should be improved; see Figure 2-13. [19]

Installation by Vibrating Hammer on Crane Hook

The second option is to use the crane of the heavy lift vessel with a vibro-hammer connected to the hook, see Figure 2-14. After connecting the hammer to the monopile, the monopile can be vibrated to self-stability or final penetration depth. The dynamic positioning system can be switched to 'Heavy Lifting Mode' (HLM) in order to keep the vessel stable and at position during hoisting operations by the crane. The hook of the crane can be used to exert inclination forces onto the monopile to correct its inclination if necessary. Due to limited angles of the hoist wires, there are restrictions to this exertion of inclination forces. Besides, it must be taken into account that the hoisting equipment will be damaged by horizontally tensioning the hoisting wires while correcting the inclination.

Although the method is relatively simple, it isn't a favorable option due to several disadvantages. A big disadvantage of the vibro-hammer at this moment is that the vibro-hammer is not able yet to vibrate a monopile to its final penetration depth. This means that at some point, the hydraulic hammer has to take over the installation in order to drive the monopile to its final penetration depth. Besides this disadvantage of the vibro-hammer, the method itself has disadvantages as well. First of all, the axial forces required for the pile penetration versus the tension in the cables might have the consequence that there will not be total control during the installation. Besides, there is no possibility for a physical inclination backup system, unless it is hammer mounted.

This installation method is not favorable at the moment. It is unknown if it is possible to effectively control the monopile by crane. Also, the crane has angular limits which have not been explored yet. To improve this option, research and tests must be executed in order to improve the disadvantages of the installation option.

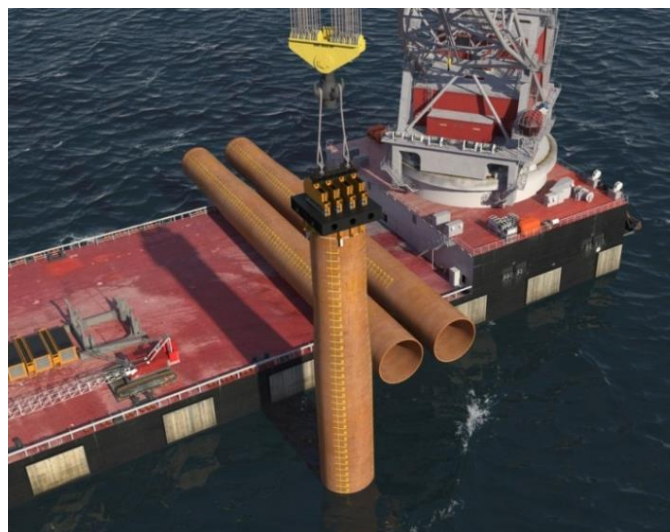


Figure 2-14 – Vibro-hammer on Crane Hook [54]

Installation with Monopile Installation Frame

The third option to install monopiles when using dynamic positioning is to use a Monopile Installation Frame (MIF), see Figure 2-15, which can be preplaced onto the scour matress on the seabed. The monopile can then be hoisted into the frame and then be driven into the seabed. On top of the frame a safety door is installed, which will be closed in order to keep the monopile inside of the frame.

While driving the monopile into the soil, the installation frame can exert inclination forces by using its hydraulic cylinders inside of the monopile gripper on top of the frame in order to secure the monopile's verticality requirements. The main advantage of this method compared to the outrigger option, is the absence of external loads on the vessel's side shell. This means that, when using the monopile installation frame, no 'external force compensation' software is required for the dynamic positioning system. When hoisting the frame onto the soil the 'heavy lifting mode' has to be activated.



Figure 2-15 – Preliminary Design of Monopile Installation Frame [20]

The MIF has some disadvantages, for instance that it has to be preinstalled and removed respectively prior and after each installation which results in extra lifts. After the installation of the monopile, the frame can be removed and transported to the next location. The removal of the monopile installation frame will go in two steps: first, the safety door will be opened after which the frame can be towed a bit sideways. When the frame is moved away from the monopile, it can be hoisted upwards and fixed to the side shell. Furthermore, the frame will be a large and complex

structure which will limit the space on the deck of the heavy lift vessel for monopiles and transition pieces. Besides, possible damage to scour mattresses must be accounted for.

Although there are some disadvantages, the main advantage is that no adjustments of the dynamic positioning system are necessary. The dynamic positioning system can compensate for the lifting operation of the frame. Also, the monopile will be installed by a hydraulic hammer, so it will be installed at final penetration depth. Therefore, this thesis will focus on the monopile installation frame, since it is the most favorable option available for installing monopiles on dynamic positioning.

2.3 Monopile Installation Frame

This section provides general information about the monopile installation frame and will state the main requirements to the frame.

2.3.1 General Introduction

As earlier stated, the MIF can be used to install monopiles on the dynamic positioning. A preliminary design of the frame is shown in Figure 2-16.

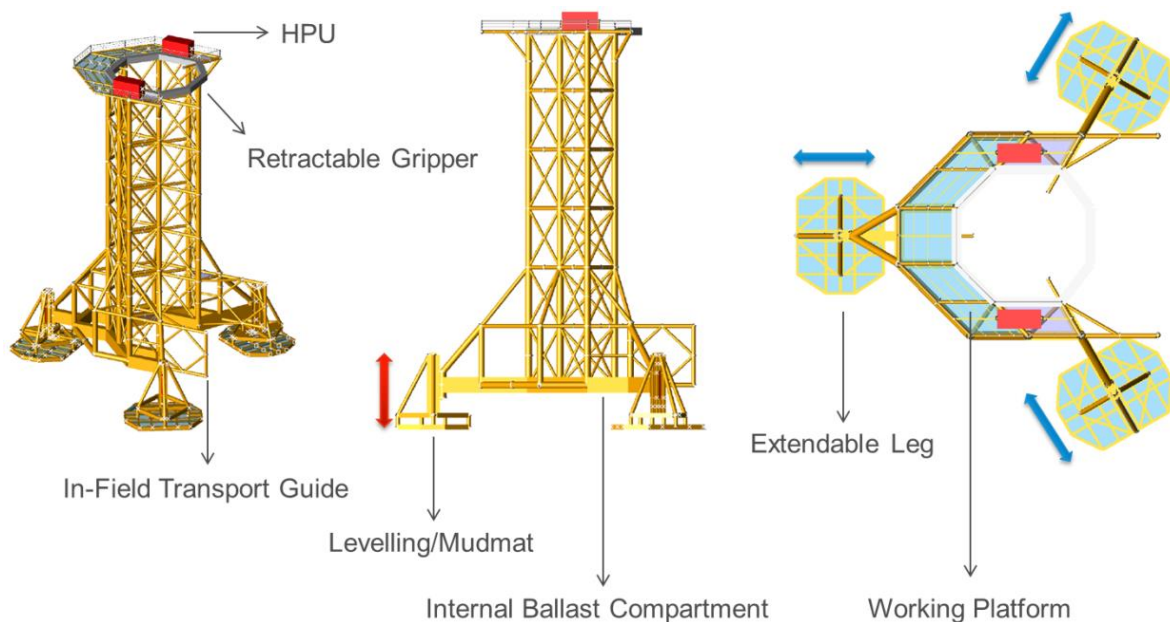


Figure 2-16 – Preliminary Design of Monopile Installation Frame [20]

2.3.2 Design Requirements MIF

Some main requirements of the design of the MIF have been formulated and are summarized in Table 2-1.

Table 2-1 - Design Requirements Monopile Installation Frame [20]

Description	Value
Weight of MIF (dry in air)	800 Mt
Ballast weight capacity (max.)	500 Mt
Modular height	35 m – 50 m
Mean footprint diameter	45 m
Operational $H_{\text{significant}}$	2.5 m
Standalone MIF survival $H_{\text{significant}}$	6 m
Max. bottom diameter MP	10 m
Min. bottom diameter MP	7 m
Max. MP weight	2500 Mt
Max. height MP	95 m

2.3.3 Built-Up MIF

The preliminary design of the MIF contains several points of interest. Each of them will be briefly discussed.

2.3.3.1 Centre of Gravity

An important part of the design of the frame is the location of the Centre of Gravity (CoG). In order to keep the lifting operations of the frame relatively simple, it is important that the CoG is at the geometrical center point of the structure. If the CoG is in the geometrical center point, it is possible to lift the structure with a 2-point lifting arrangement.

2.3.3.2 Retractable Legs

The monopile installation frame will be designed with three extendable telescopic configuration legs. Each leg is connected to a mudmat. With the possibility of adjusting the legs, it is possible to use the frame in different situations. This makes the frame an interesting investment for the company, since it can be used during different projects.

2.3.3.3 Retractable Monopile Gripper

At the highest level of the installation frame is a retractable monopile gripper installed. When the monopile is positioned inside of the gripper, retractable hydraulic cylinders hold the monopile stable above its target area, as is shown in Figure 2-17. During hammering of the monopile, verticality correction can be done by the hydraulic cylinders if necessary. In the monopile gripper is a safety door installed, as seen in the design of the outrigger. This safety door will be closed once the monopile has entered. Extra clearance for the installation of the transition piece can be provided by retracting the monopile gripper.

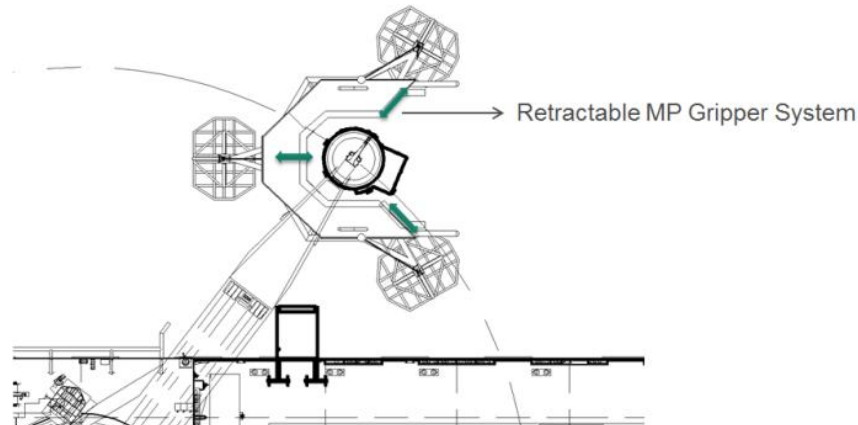


Figure 2-17 – Monopile Gripper [20]

2.3.3.4 Levelling of the MIF

In order to control the levelling of the frame, a hydraulic jacking system is used. This system is used within each leg in between the structure and the connection point to the mudmat. The result is that each mudmat can be settled independently onto the seabed. The frame will be placed onto the scour matress on the seabed which is placed in order to protect the monopile. The monopile gripper on top of the installation frame, which can be seen in Figure 2-16, will be the base reference for the inclination control of the monopile. Inclination measurements of the frame will be executed at its highest level in order to eliminate manufacturing and tolerance errors. Consequently, a reliable initial verticality of the monopile is granted.

2.3.4 Transportation and Installation MIF

The transportation of the installation frame and the installation of monopiles with the frame will be discussed.

2.3.4.1 Transportation and In-Field Storage MIF

The monopile installation frame can be transported to the projects location on the heavy lift vessel or on a construction barge. The frame will be located in the field at its stand-by position(s). It is possible to store the MIF in standalone condition on the seabed in designated locations. The designed survival sea state is $H_s = 6.00$ m with gust wind velocity according to Det Norske Veritas (DNV).

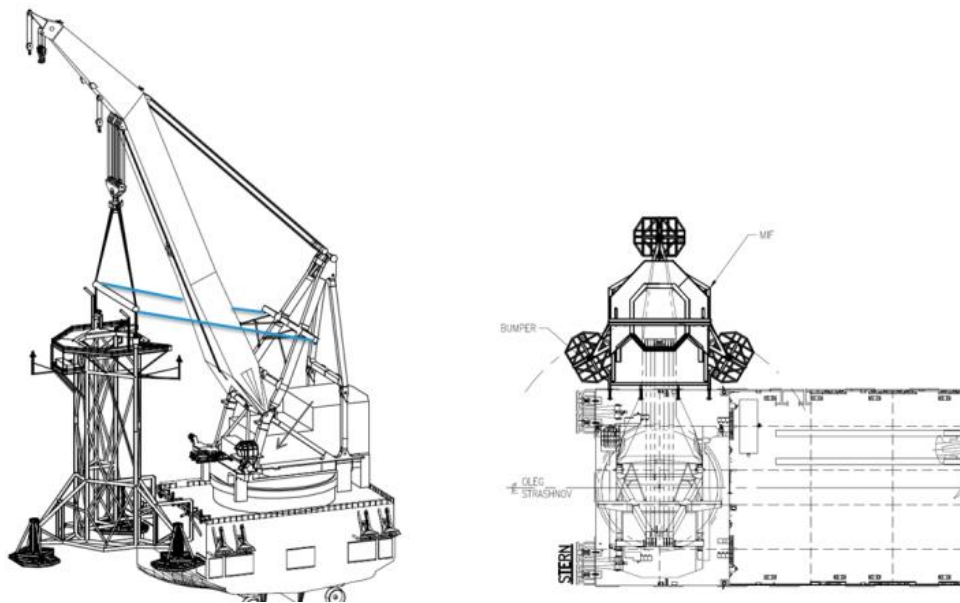


Figure 2-18 - Lifting of Monopile Installation Frame [20]

After the installation of a monopile, the frame will be transported in the field to the next installation site. To transport the installation frame in the field, it will be hoisted by the crane and will be supported at the vessel's side shell. To control the lifting process and to tension the frame against the side shell of the vessel, two tugger lines can be engaged, see Figure 2-18. This configuration provides the maximum workability for the transportation.

2.3.4.2 Installation of Monopile Using MIF

The installation of a monopile with the installation frame is comparable to the installation with an outrigger, with the exception of the positioning and levelling of the installation frame. To ensure stability and the right reference level of the frame, it needs to be levelled before the start of the monopile installation process. After the positioning and levelling of the frame, the monopile will be guided into the frame and will be centralized, after which the safety door will be closed. Then, the monopile can be driven into the soil to its designated final penetration depth.

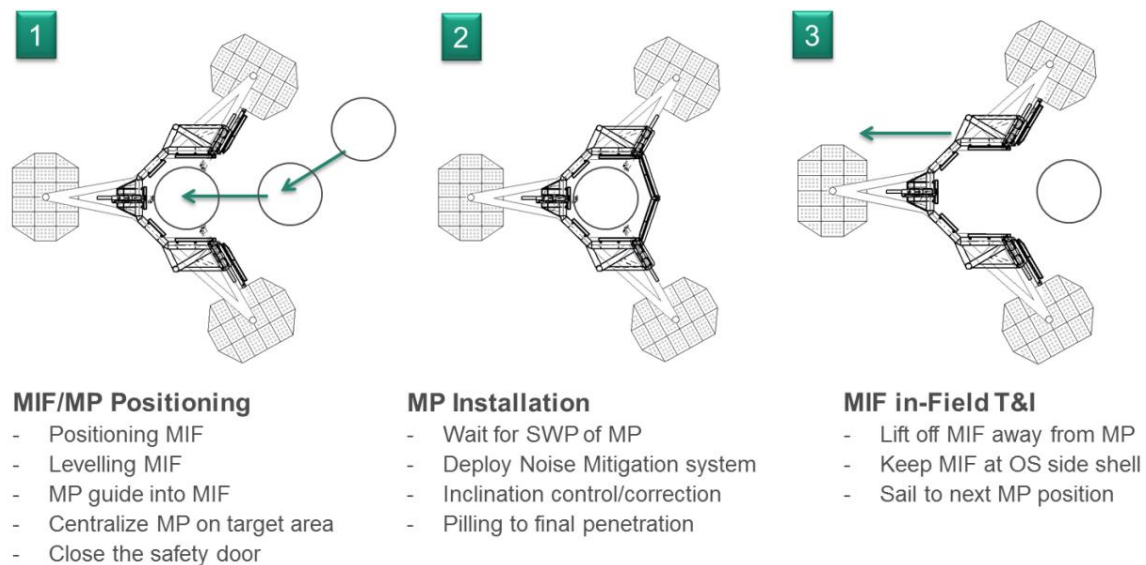


Figure 2-19 – Installation Step-by-Step [20]

After installation of the monopile, the frame will be removed from the site and will be transported to the next installation location. The removal of the frame will be done in two steps: first, the safety door will be opened after which the frame can be towed a bit sideways. When the frame is moved away from the monopile, it is hoisted upwards and fixed to the side shell. The installation process is shown step-by-step in Figure 2-19.

2.3.4.3 Integrated Noise Mitigation System

It is a possibility to, either permanently or temporarily, implement noise mitigation systems, such as HSD, AdBm or bubble curtains, Figure 2-20.

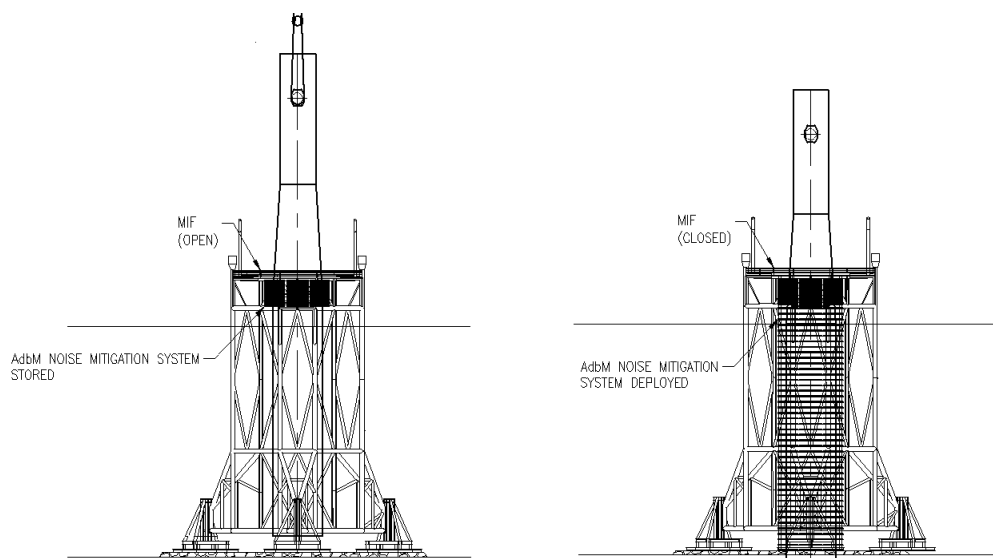


Figure 2-20 - Integrated Noise Mitigation System [20]

2.4 Introduction to Thesis Subject

This section gives a general introduction to the subject of the thesis.

2.4.1 General Introduction

As earlier stated the offshore wind industry is expected to continue its growth. Expected is that the capacity of the offshore wind turbines will increase, together with the depth of the water in which the wind turbines are placed. The depth in which the windfarms are installed is increasing towards 40 meters and more; see Figure 2-3. The growing capacity of the wind turbines and the increase of depth result in the necessity of bigger monopiles.

Seaway Heavy Lifting executes both the transportation and installation of monopiles and transition pieces. It is also expected is that the monopile sizes will increase. The Danish company MTHøjgaard has studied the viability of bigger monopiles, so called XL monopiles, in 35 meters water depth with a 6 MW turbine. This study resulted in the identification of XL monopiles as the best solution for offshore wind turbine foundations up to 35 meters water depth. The XL monopiles can have diameters up to 10 meters and can be installed in depths between 18 to 35 meters. [21]

In order to stay competitive, Seaway Heavy Lifting should account for future installations of larger monopiles in deeper water depths. Because of the expected growth of the offshore wind market, Seaway Heavy Lifting is exploring improvement options to increase the efficiency of the installation process of monopiles. The most promising option is to reduce the installation duration of the monopiles. This will be achieved by installing monopiles on dynamic positioning using the monopile installation frame.

The MIF will be a modular structure, which means that it will be possible to change the height of the frame for various water depths. This will be achieved by the use of an extension piece that can be placed into or removed from the frame. The connections used to connect and disconnect the extension piece are expected to be the most critical sections of the frame regarding the fatigue lifetime. Therefore, during this thesis the subject will be the optimization of the critical section of the MIF.

2.4.2 Critical Section MIF

It is assumed by Seaway Heavy Lifting that the connections between the members will be made using bolted flange connections. This is an often used method and is therefore chosen to be the most convenient. The bolted flange connections will be used to connect the members to each other when no extension piece is used, and to connect the members to the extension piece.

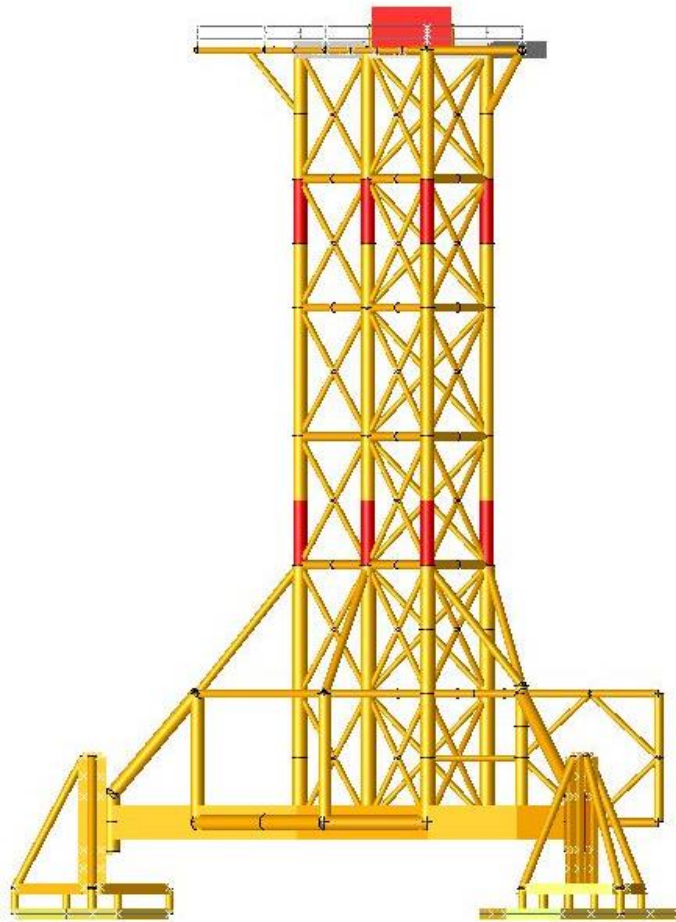


Figure 2-21 - Members to be Connected by Bolted Flange Connections

The members that will be connected by bolted flanges have been given a red color in Figure 2-21. In this figure, the MIF is shown with the extension piece. The bolted flange connections used in the frame will be made of machined parts. This means that the flange and part of the tube will be machined. The piece will then be welded to the member. Once complete, the members can be connected by bolts.

The junction between the flange of the connection and the tube part of the connection is sensitive to stress concentrations. Stresses need to ‘travel through’ this junction, which in case of a sharp angle will lead to high stress concentrations. Therefore, during this thesis the tube-to-flange junction will be studied. It is known the stress concentration in the junction will have a severe impact on the lifetime of the structure. Therefore, the tube-to-flange junction will be optimized with respect to the fatigue load case. This will lead to a final, optimized design of the critical section of the MIF.

3 State of Art Bolted Flange Connection

The state of art introduces the bolted flange connection and states the design rules for bolted flange connections. The MIF is designed as a modular structure, using an extension piece to change its height. The connection and disconnection of the extension piece needs to be relatively easy. Therefore, the choice has been made to connect the extension piece to the members with use of a bolted flange connection. Bolted flange connections are a well-known practice and thus often used in structures.

3.1 Introduction Bolted Flange Connection

Bolted flange connections are an often used practice in pipelines and structures, see Figure 3-1. Most common is that the flange is connected to the tube by a weld. However, Seaway Heavy Lifting wants to machine the bolted flange connection, which has as a result that the weld can be placed in a less critical section. The bolted flange connection can be used for all types of diameters. In the MIF, the bolted flange connection will be used to connected members with a diameter of 914 mm.



Figure 3-1 - Bolted Flange Connection with Fastening Tool [22]

3.1.1 Statically and Dynamically Loaded Bolted Flange

The bolted flange connection can be placed in members that are loaded statically or dynamically, see Figure 3-4 and Figure 3-5. Static loaded connections will mostly be loaded in compression due to the self-weight. Dynamically loaded connections will undergo both compression and tension loading and static loading due to self-weight. The stress transmission through a bolted flange connection loaded in compression is different from the transmission of tension stresses, which has been shown in respectively Figure 3-2 and Figure 3-3. As can be seen in Figure 3-3, a concentration of stresses occurs in the junction between the tube and the flange.

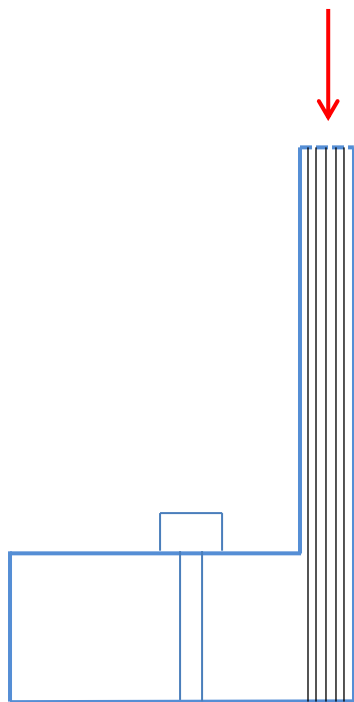


Figure 3-2 - Stress Transmission in Case of Compression

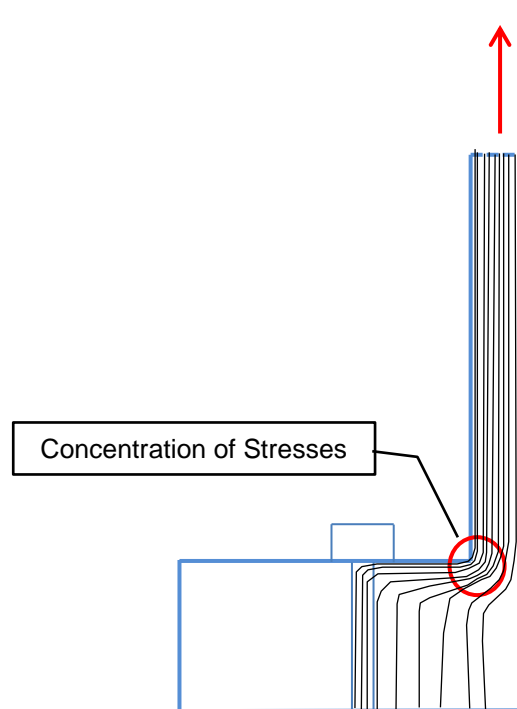


Figure 3-3 - Stress Transmission in Case of Tension

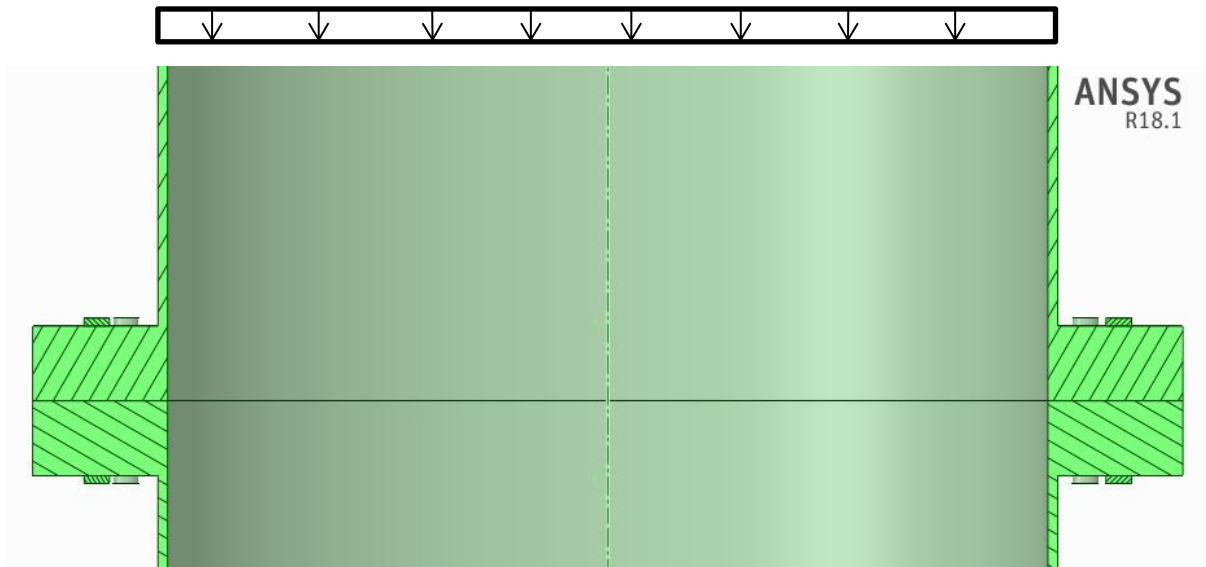


Figure 3-4 - Statically Loaded Bolted Flange Connection

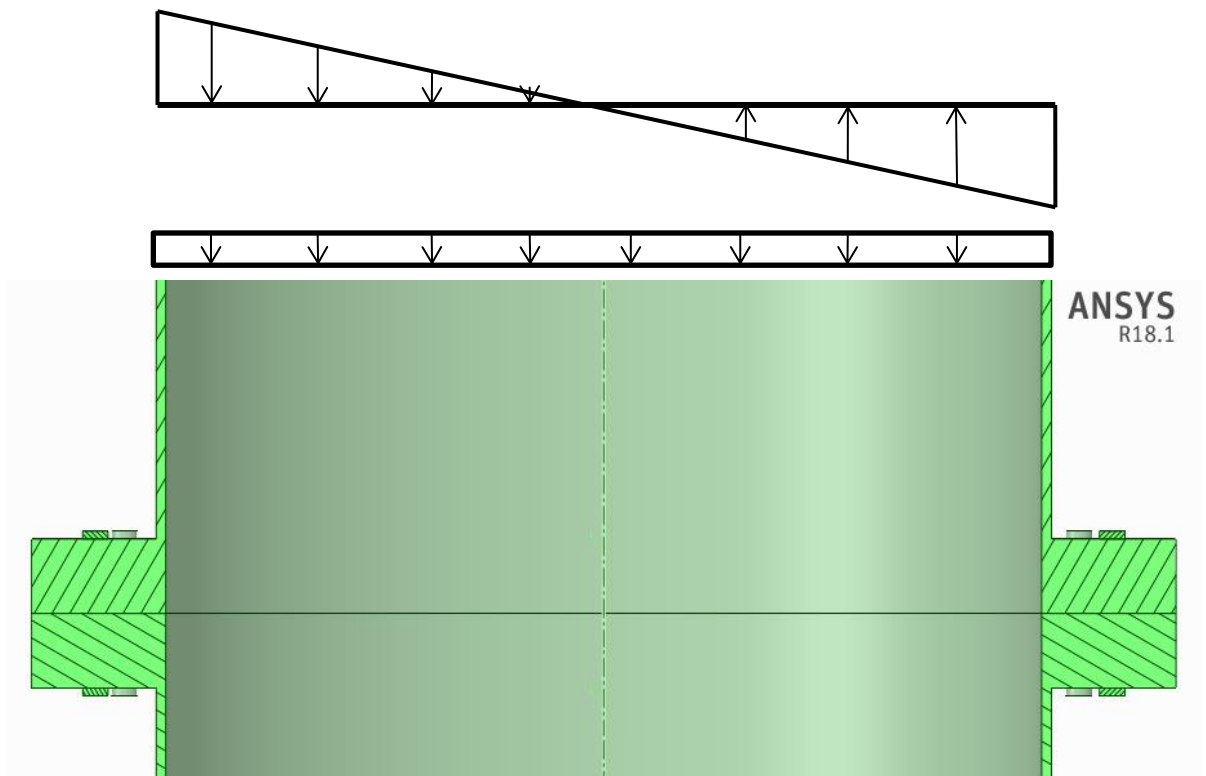


Figure 3-5 - Dynamically Loaded Bolted Flange Connection

3.1.2 Failure Modes Bolted Flange Connection

In order to check the structural safety of a bolted flange design, the different failure modes that are stated in literature can be used. Three different failure modes for the bolted flange connection can be distinguished and are explained below:

1. Failure Mode A

Failure mode A focuses on failure of the bolt and therefore assumes a very stiff flange and a relatively weak bolt, see Figure 3-6.

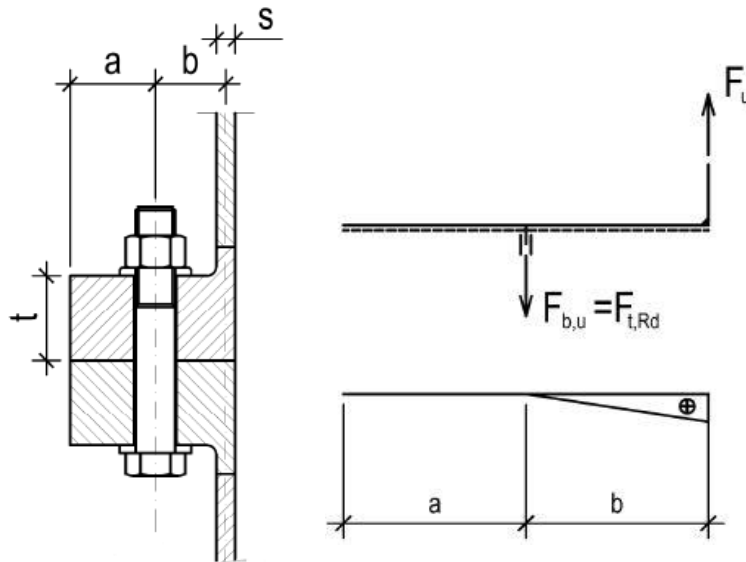


Figure 3-6 - Failure Mode A [24]

2. Failure Mode B

Failure mode B focuses on bolt failure and the formation of a plastic hinge in the shell, which can occur simultaneously; see Figure 3-7.

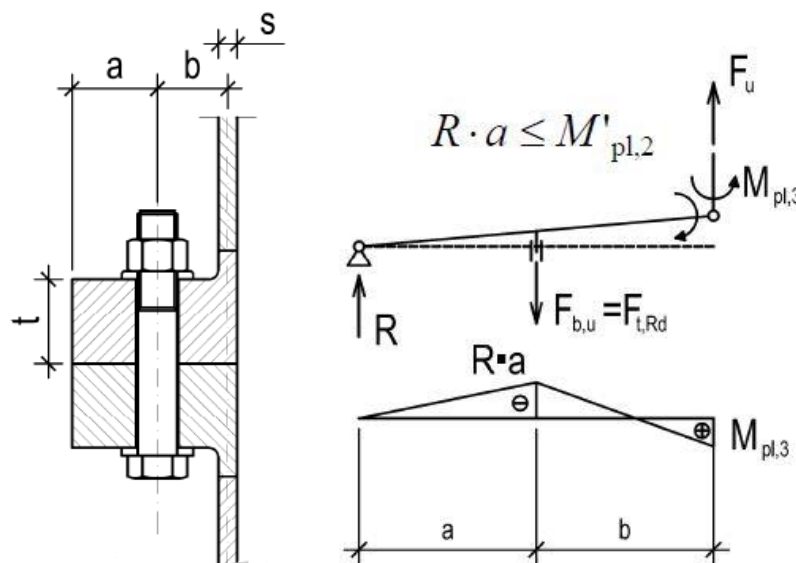


Figure 3-7 - Failure Mode B [24]

3. Failure Mode C

Failure mode C focuses on the formation of plastic hinges in both the shell and in the flange at the centerline of the bolt; see Figure 3-8.

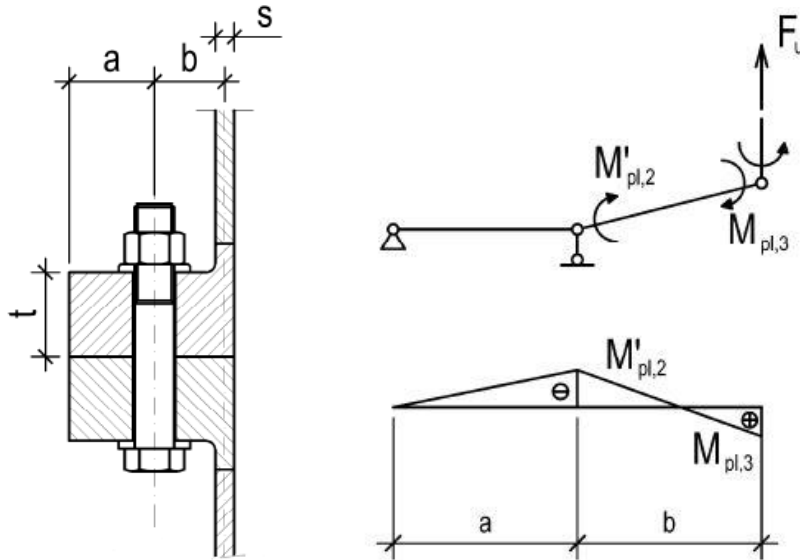


Figure 3-8 - Failure Mode C [24]

3.2 Fatigue Behavior Bolted Flange Connection

The fatigue behavior of bolted flange joints is highly influenced by the way the stresses are transmitted through the joint. Also, joints using pretension bolts have favorable fatigue behavior compared to joints using non-pretensioned bolts. The most favorable bolted flange connection therefore uses pretensioned bolts and has a relatively smooth transmission of stresses through the connection. Important for the smooth transmission of stresses is the junction between the tube of the member and the flange of the connection. In this junction a high concentration of stresses is expected, which makes the junction a critical section with respect to fatigue.

3.2.1 Welded Bolted Flange Connection

The bolted flange connection can be made using a circumferential weld. This weld is placed in order to connect the flange to the tube, see Figure 3-9. The use of a weld has a significant influence on the stress distribution in the connection. The welding of two members has an influence on the strength properties of the member material. The heat from the welding process and the cooling process afterwards causes the change of the microstructure and the strength properties of the material. The zone around the weld, the heat affected zone, is where the properties of the material are changed compared to the rest of the section. The amount of changes depends on the weld material used and the base material that is welded.

The weld will be constructed in such a way that the stress transmission will go smoother, but still not be optimal. Both the changes of material properties and the influence of the configuration of the weld on the stress distribution in the connection have as a consequence that the tube-to-flange junction is a critical section with respect to fatigue. In order to improve the fatigue life, the weld should be grinded afterwards to achieve the smooth transmission. [23]

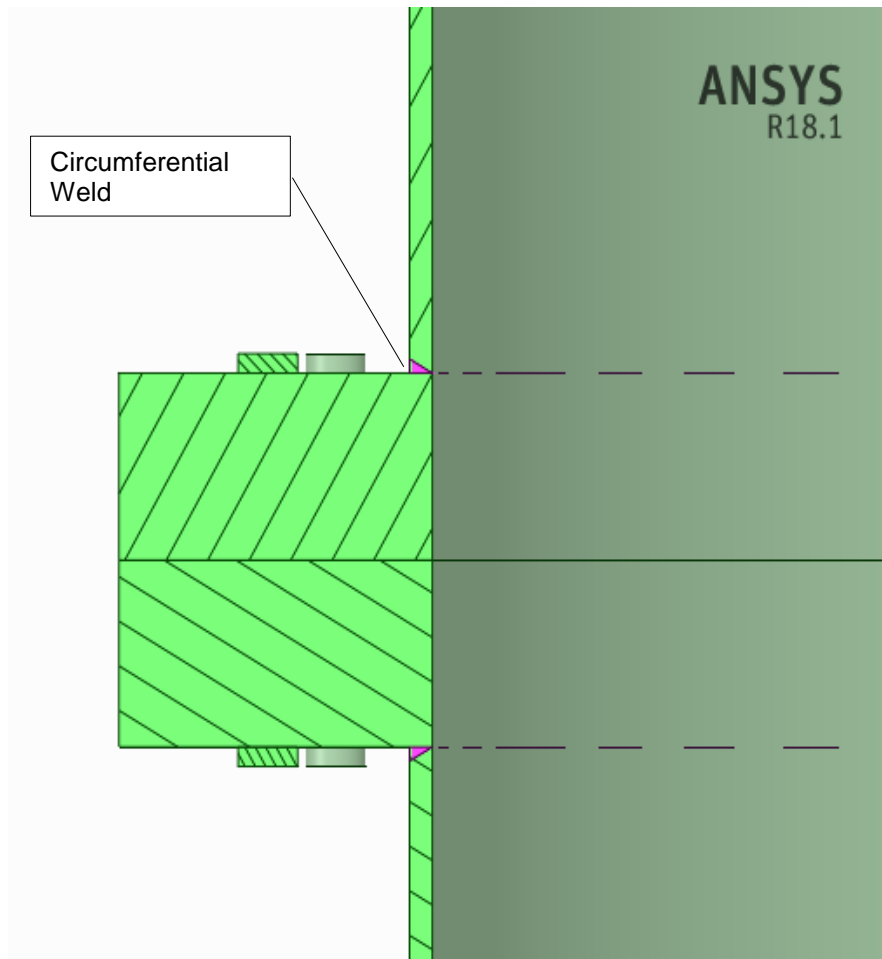


Figure 3-9 - Welded Tube-to-Flange Connection

3.2.2 Machined Bolted Flange Connection

The bolted flange connection can also be produced by machining. In this case, the connection is manufactured from a thick steel plate of which certain edges are removed by 'scraping' them away. In this manner a very smooth tube-to-flange junction can be realized. This junction doesn't need to be grinded afterwards, as is the case when using a welded tube-to-flange junction. It is found that the magnitude of the radius of the tube-to-flange junction, as shown in Figure 3-10, has an influence on the stress distribution through the connection. If the radius is almost non-existent, the change from flange to tube will be abrupt which leads to a concentration of stresses on the surface of the junction. If the radius of the junction is increased, a smooth transmission of the stresses is expected which will lead to a lower concentration of stresses in the junction. The lower the concentration of the

stresses is, the higher the fatigue life will be. This makes the machined flange, although expensive, favorable over the relatively simple welded bolted flange connection. [23]

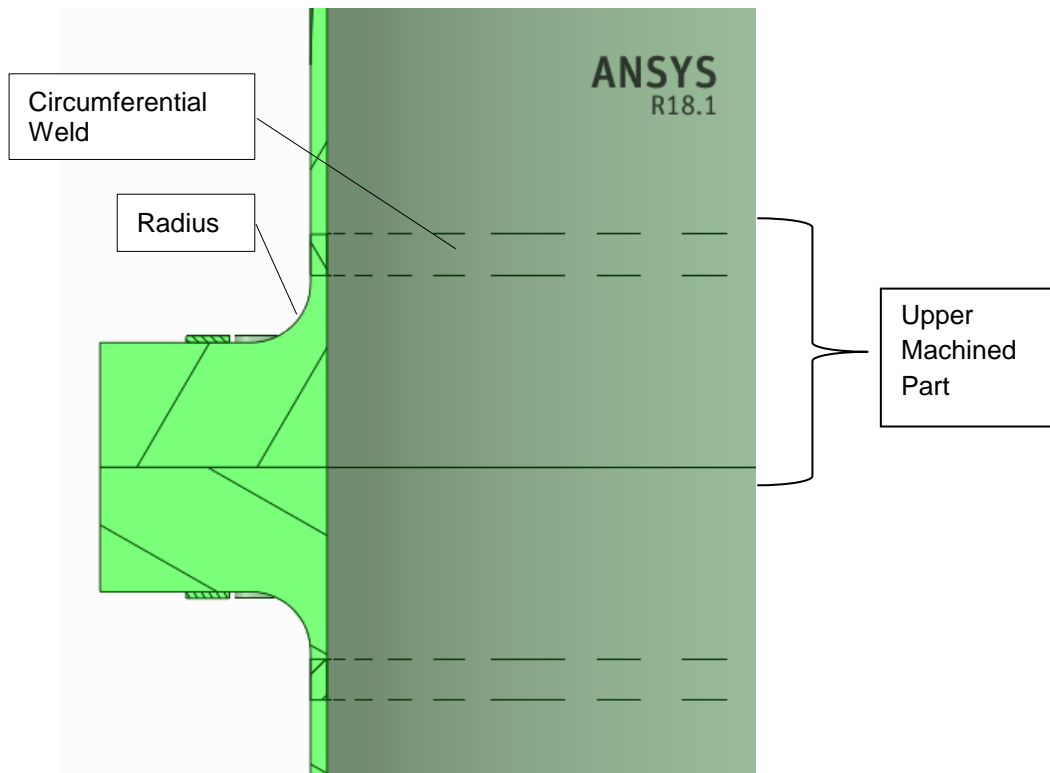


Figure 3-10 - Machined tube-to-Flange Connection

3.2.3 Fatigue Behavior Bolt

Bolts used in bolted flange connections are usually pretensioned. This pretension load is applied to the bolt before any other loading is applied to the connection. Most commonly, the bolt is pretensioned up to 70% of its ultimate strength. The pretensioning of the bolt has as a result that the bolt will not loosen under tensional loading, as long as this loading is lower than the applied pretension. Due to the pretensioning of the bolt, the bolt will not be exposed to the full amplitude of cyclic tension loading. This has as a result that a bolt has an increased fatigue life once pretensioned.

In this thesis, the fatigue behavior of the bolt has not been studied. The bolt is assumed to be of a sufficient quality and grade for the connection. Also, the bolt can be changed quite easily, which won't have a significant influence on the geometry of the connection and therefore not on the fatigue life either. [24]

3.2.4 Geometry Characteristics Bolted Flange

In order to be able to start the optimization of the connection with respect to the fatigue load case, geometry characteristics of the bolted flange should be available. Therefore, research has been done to find applicable design rules for bolted flange connections in order to calculate an initial geometry.

The paper: '*Zur Bemessung geschraubter Ringflanschverbindungen von Windenergieanlagen*' written by ir. M. Seidel [24] states design rules for bolted flanges. These rules are designed as starting points for the design of wind turbine tubes, which have the bolted flange on the inside of the tube, see Figure 3-11. The design rules are designed for a situation in which fatigue plays a big role. Wind turbines undergo fatigue loading due to the rotation of the blades. This means that the initial geometry for the MIF will be designed taking into account fatigue loading. The bolted flange connection of the MIF will be on the outside of the tube.

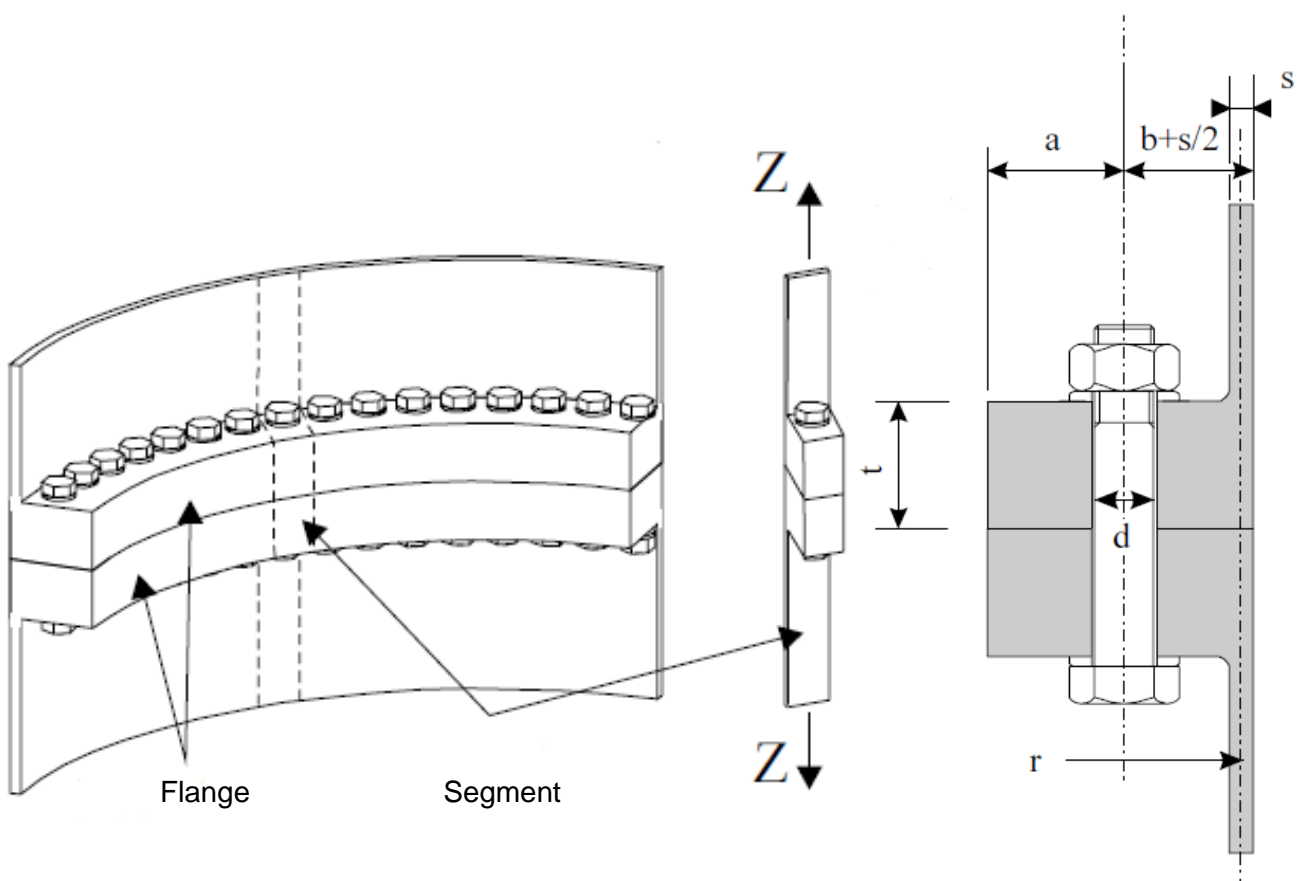


Figure 3-11 - Bolted Flange Position [24]

Figure 3-12 - Geometry Characteristics Bolted Flange [24]

3.2.4.1 Design Rules Seidel

The stated design rules by Seidel, which use the configuration shown in Figure 3-12, are as follows:

- $b + \frac{s}{2} \leq 2d$
- $a \geq 1.45 * \left(b + \frac{s}{2}\right)$
- $t \geq 1.5d$ but:
 - $t \geq 4 * s$ when $\frac{r}{s} \geq 50$
 - $t \geq 3 * s$ when $\frac{r}{s} = 100$
 - $t \geq 2 * s$ when $\frac{r}{s} \geq 200$
- $\frac{c}{d_{bolt}} \leq 2 * \frac{d}{s}$ but:
 - $c \geq 65 \text{ mm}$

In which:

$$r \text{ [mm]} = \frac{1}{2} * (d_{outer,tube} - s)$$

$d_{outer,tube}$ [mm] = outer diameter of the tube

$$c \text{ [mm]} = \frac{(d_{outer,flange} - s) * \pi}{n_{bolts}}$$

$d_{outer,flange}$ [mm] = outer diameter of the flange

However, there is a minimum requirement that the detail b has to meet. This is summarized for bolt type M24, quality 8.8, in Table 3-1.

Table 3-1 - Minimum Requirement b [24]

Detail	Minimum (mm)
b-s/2	40

4 Verification ANSYS

The MIF will be designed as a modular structure. Therefore, the joints between the tubular members must be easy to connect and disconnect. The bolted flange connection is an often used practice for the connection of tubular members and will therefore be used in this study. The connection will be optimized for fatigue loading due to environmental loading and hammering of the monopile.

4.1 Introduction

The optimization of the bolted flange connection will be done with a finite element model made in ANSYS. In order to verify the ANSYS model, the stress distribution in the connection is studied. The stresses in the connection will concentrate in the junction between the tube and the flange. With the maximum stress in the junction and the nominal stress in the tube the stress concentration factor (SCF) can be determined. The SCF value obtained from the ANSYS model is compared with stated SCF values from the reference project that is stated in Reference [25].

4.2 Verification Model

In order to verify the FEM method that will be used, a simplified model of a part of the bolted flange connection has been built. The model exists of the flange of the connection and part of the tube. The geometry of the model has been built according to given geometry, mesh sizes and constraints. The load that has been applied to the model has a value of 1 MPa.

4.2.1 Geometry

The geometry of the verification model is similar to the given geometry in the reference project; see Table 4-1, to get results that can be compared. [25] Since the bolted flange joint is symmetric, only the upper half of the connection has to be modelled.

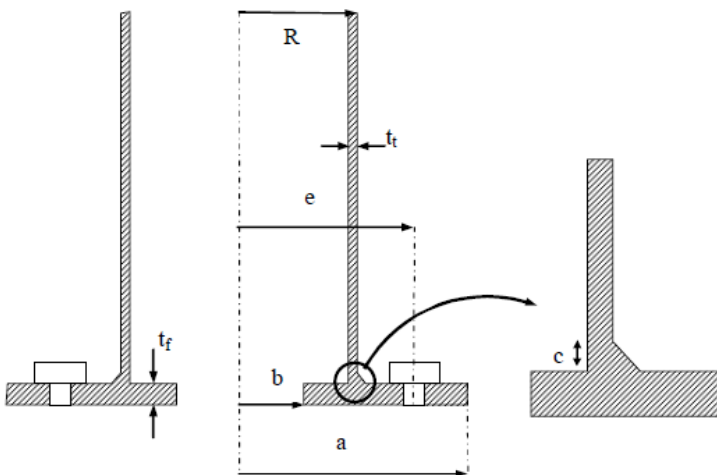


Figure 4-1 – Side View Bolted Flange Connection

Table 4-1 - Details of Connection

Detail	Size
a (mm)	458.5
e (mm)	422.5
R (mm)	374.75
b (mm)	368.5
t _f (mm)	40
t _t (mm)	12.5
Bolt Type	M24
Amount of bolts	24
Diameter Bolt Hole (mm)	26

4.2.2 Mesh Settings

The settings of the mesh that have been used are based on the mesh settings stated in the reference project, see Figure 4-2. For the bolt a sweep method has been used. The used mesh size in the reference project is quite big which has as a consequence that the stress values aren't reliable. The mesh made in the verification model is shown in Figure 4-3.

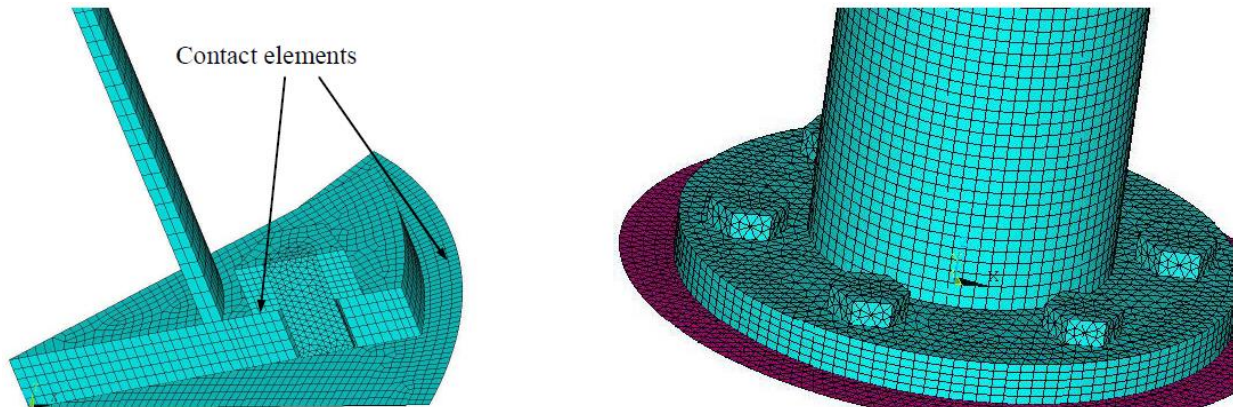


Figure 4-2 - Mesh of Model Reference Project [25]

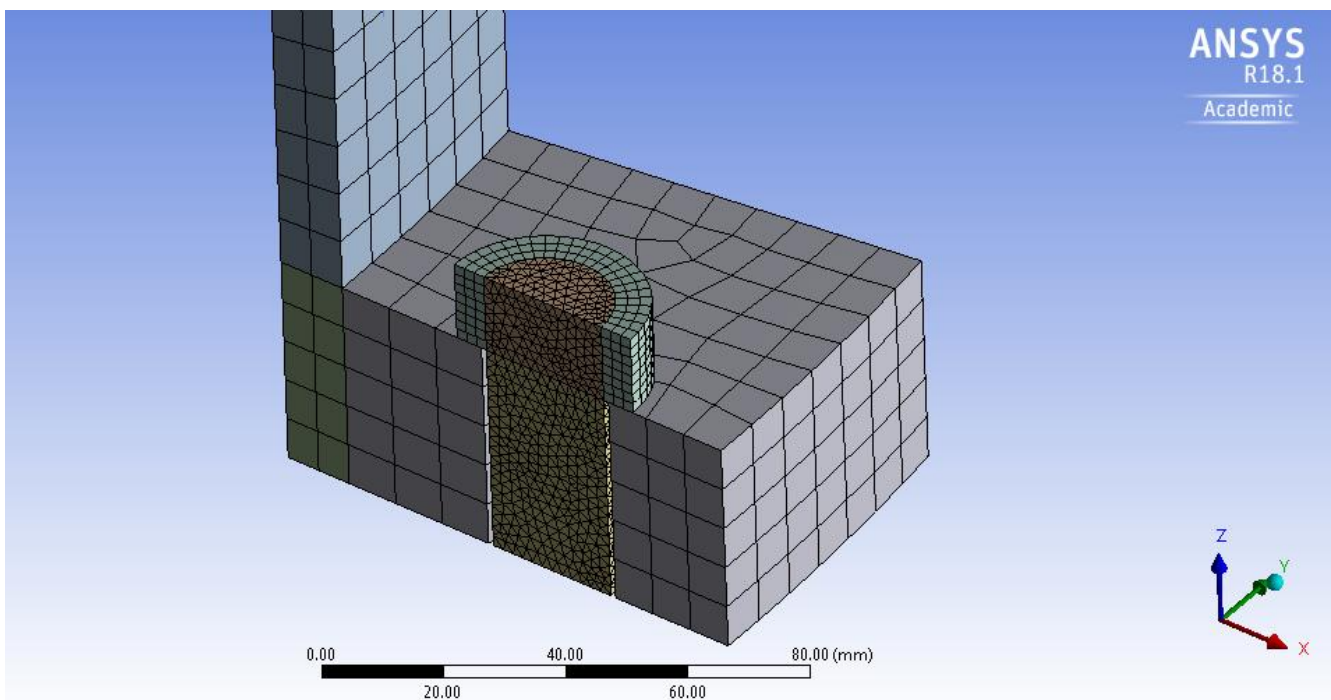


Figure 4-3 - Mesh of Verification Model

4.2.3 Stress Concentration Factor

The stress distribution of the verification model is obtained by using ANSYS and displayed in Figure 4-4. With this stress distribution, the stress concentration factor can be determined and compared with the given SCF numbers, see Table 4-2.

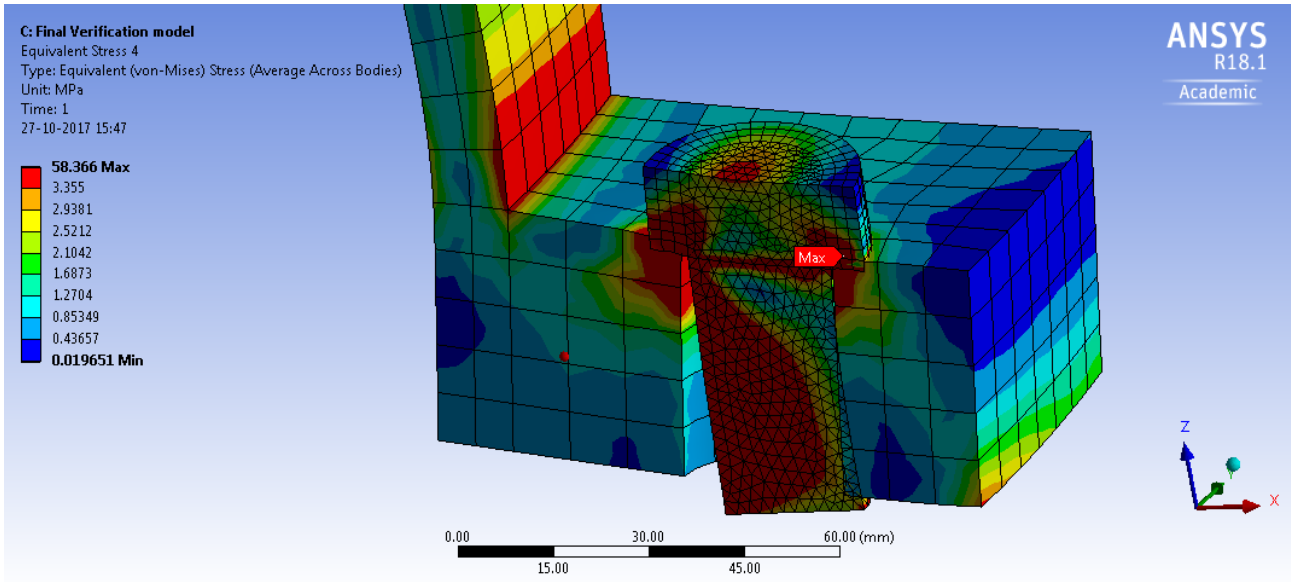


Figure 4-4 - Stress Distribution in the Verification Model

The stress concentration factor is obtained along the tube-to-flange junction, as is shown in Figure 4-5. By obtaining the stresses in the points 1 to 7 and dividing these by the applied stress (1 MPa), the SCF is obtained. The values per point are displayed in the graph in Figure 4-6.

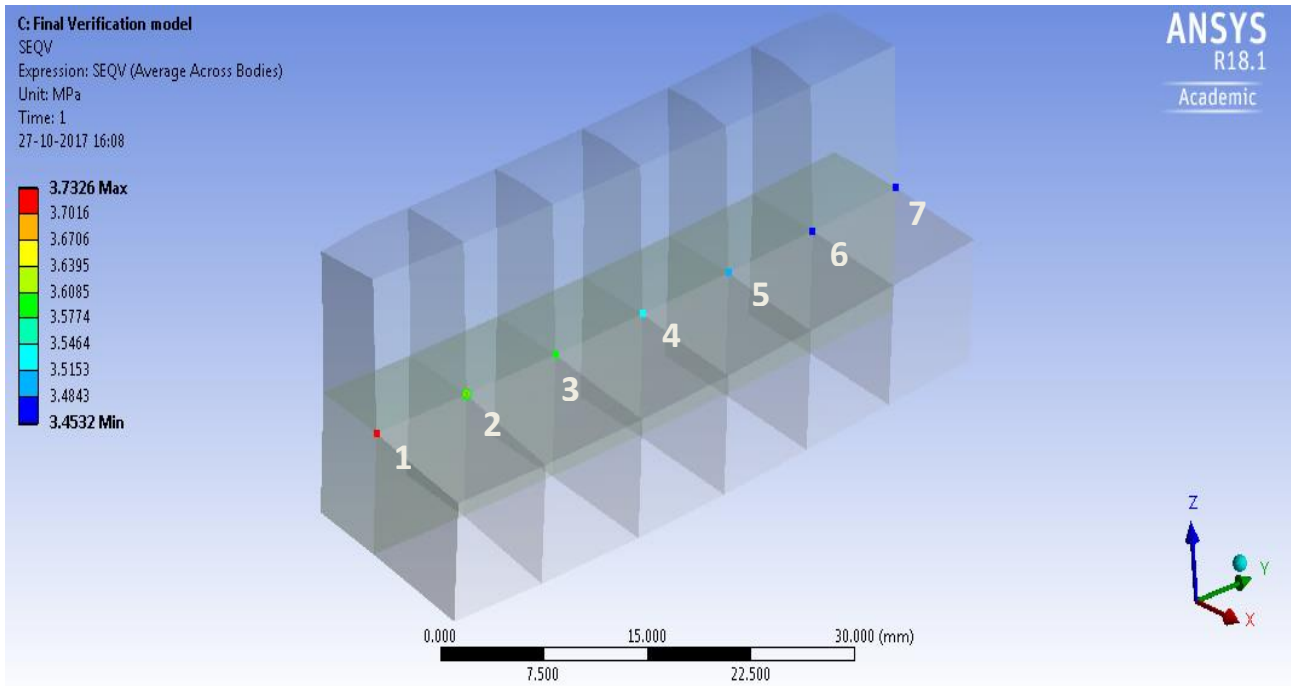


Figure 4-5 – Values of Stresses in the Tube-to-Flange Junction

The tension applied to the model equals 1 MPa, which means that the stresses in the edge have to be divided by 1 MPa to obtain the SCF. The average SCF obtained by this method in the tube-to-flange junction is 3.57.

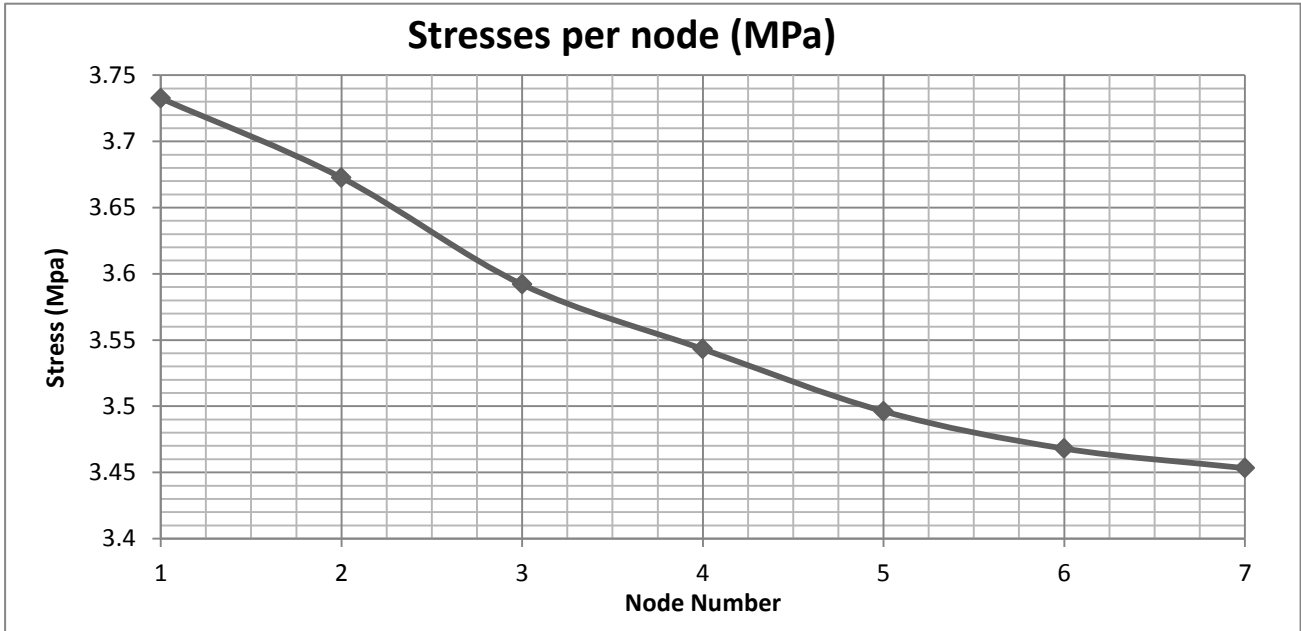


Figure 4-6 - Stresses per Point as given in Figure 4-5

In the reference project, the stress concentration factors per used calculation method have been given. These are shown in Table 4-2. [25] For the verification, model ‘S-7’ has been used.

Table 4-2 - Stress Concentration Factors Reference Project [22]

Connection and R/t_t	Ratio of Bolt force to tube tensile force : $\tan \phi$				SCF at the weld toe				
	Test result	3D FEM	Cao & Bell	Authors	3D FEM	Cao & Bell	Authors	Chabrolin & Ryan	
S-1	11	1,35	1,37	1,54	1,47	2,22	2,27	2,53	2,77
S-2		1,45	1,48	1,61	1,57	3,24	2,98	3,18	3,81
S-3		1,27	1,28	1,36	1,37	2,30	2,22	2,35	2,77
S-4		1,63	1,54	1,64	1,73	2,93	3,18	3,03	3,29
S-5	105	-	2,05	2,15	2,09	2,39	1,63	2,63	1,52
S-6	63	-	2,13	2,14	2,05	2,98	2,14	3,23	1,92
S-7	30	-	1,87	2,01	1,86	3,97	3,38	4,50	2,71
S-8	23	-	1,76	1,92	1,74	4,40	3,87	4,92	3,04
S-9	30	-	1,64	1,70	1,61	3,10	2,73	3,76	2,71

4.3 Comparison of Stress Concentration Factors

In order to verify the ANSYS model that has been made and the model of the reference, the SCF values are compared. The results are given in Table 4-3.

Table 4-3 - Stress Concentration Factor Values

Method	SCF-Value [-]
Cao and Bell	3.38
Chabrolin and Ryan	2.71
3D-FEM Model Authors	3.97
Verification Model ANSYS	3.57

As can be seen in Table 4-3 there are some differences between the results obtained by the different methods. The method of Cao and Bell is based on experimental results, which results in a bit of difference between the SCF's obtained by Cao and Bell and obtained by Finite Element Programs. However the SCF of Cao and Bell and the 3D-FEM model of the authors are comparable with the SCF obtained from the verification model. The differences between the values are small and can be lead back to modelling differences.

However, the SCF obtained by Chabrolin and Ryan is quite different compared to the other values. Chabrolin and Ryan, see 12.2.1, determine the SCF by use of a formula that does not include any forces. This makes their method quite inaccurate and therefore their SCF value is the most different from the other SCF values. Consequently it can be said that the verification model is verified.

5 Structural Optimization

The following chapter describes the structural optimization process for the connection and the different steps of this process. A global introduction for the optimization is given in the following section, followed by a flowchart.

5.1 Introduction

The structural optimization for the fatigue load case of the connection is done in several steps. These steps can be divided in a part considering the static loading onto the complete MIF structure, a part considering the resistance of the bolted flange connection with respect to static loading and a part considering the cyclic resistance of the flange of the connection applied in the MIF.

First of all, a global load analysis needs to be done, as described in chapter 6. This global load analysis can be used to determine an initial geometry and to determine the ultimate load case. A first assumption for the geometry is necessary in order to design a model in ANSYS.

With the initial geometry and the ultimate load case known, a verification of the failure modes can be done. If the results for the failure modes aren't satisfying, the initial geometry should be changed. If the results are satisfying, a model in ANSYS can be made. This model is based on the initial geometry and the applied loads will be based on the ultimate load case.

Once the model has been built and the forces have been applied, a finite element calculation can be executed. This calculation will give a clear overview of the stress distribution in the model. From this stress distribution, the stress concentration factor (SCF) in the tube-to-flange joint can be determined. The SCF will be used in the fatigue analysis and will have a significant impact on the fatigue life.

The fatigue analysis is done using a wave scatter diagram and the SCF as input. The fatigue analysis will result in a target life for the connection. If this target life is less than 20 years, the SCF has to be optimized in order to increase the target life. If the target life is higher than 20 years, the connection needs to be validated once more with respect to the failure mode. If this validation gives satisfying results, the final design has been obtained.

The complete process is displayed with help of a flowchart in Figure 5-1.

5.2 Flowchart Optimization Process

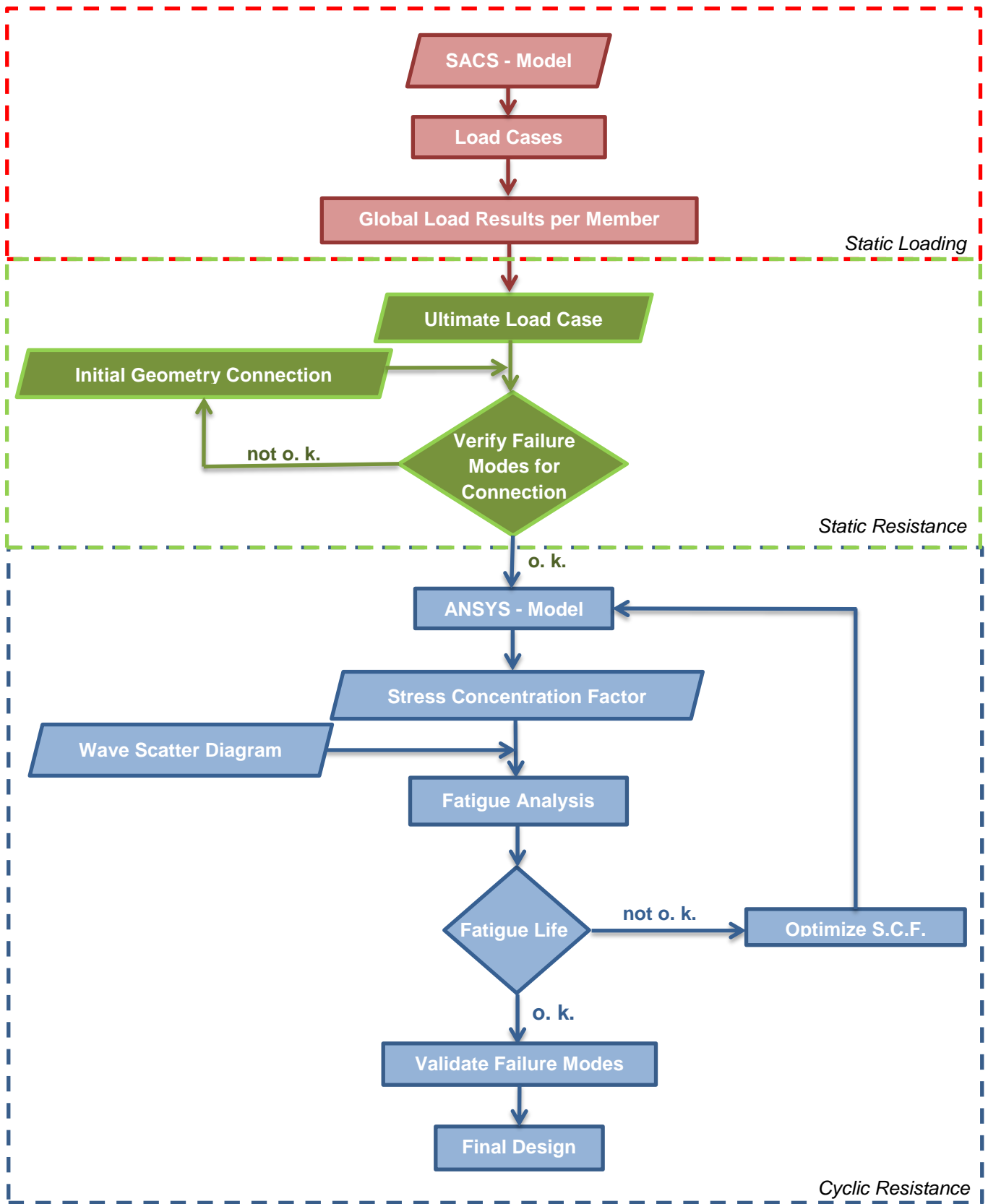


Figure 5-1 - Flowchart Optimization Process

6 Global Load Analysis

This chapter discusses the load scenarios and load cases that have to be considered during the design process of the monopile installation frame (MIF). Besides, the different types of loading are discussed in detail. Parameters used for the different types of loading are stated and explained in Appendix 12.1. Furthermore the different load combinations that have been applied are stated.

6.1 Types of Loading MIF

The loads acting on the monopile installation frame can be divided into three main types of loading: dead loads, live loads and environmental loads. However, live loads will not be considered for the MIF load analysis since the loads have a marginal contribution compared to the dead and environmental loading.

6.1.1 Dead Loads

Dead load includes the dry-weight of all structures, equipment, ballast weight and additional provisions. Dead weight has to be closely monitored and weight contingencies shall be taken into account. The contingencies are discussed in the Design Requirements, given in Reference [26]. The design requirements have stated that the monopile installation frame shall not exceed the dry-weight requirement of 800 Mt. [27]; [26]

6.1.2 Environmental Loads

As prescribed in 'Det Norske Veritas' all environmental phenomena which may contribute to structural damages shall be considered. The following environmental loads are discussed:

- Hydrodynamic loads induced by waves and currents
- Wind loads

The environmental loads acting on the monopile installation frame will be discussed in the following sections. [27]; [26]

6.2 Load Scenarios

In order to design the installation frame and to observe its reaction forces, load scenarios have to be formulated. The different load scenarios are illustrated in Figure 6-1.

The MIF has to be designed to withstand loads induced by environmental conditions during operational and survival conditions in the following three main scenarios:

1. MIF with Monopile During Operational Conditions

During this load scenario the environmental conditions will be within the allowed working conditions, which are discussed in 0 . During this scenario, a monopile will be present in the frame. For the monopile wind loads, wave loads and loads due to currents have to be taken into account typical for the field in which the MIF is used.

The governing load case during this scenario is when during installation the operational load conditions have the maximum allowed values. These conditions are the most severe conditions the structure has to be able to withstand during operation and are therefore the governing load case in this scenario.

2. MIF without Monopile During Stand-Alone Conditions

During the stand-alone scenario the MIF will be left alone in the field when it is not needed for a few weeks or months. The MIF has to survive on its own, since the vessel is not nearby.

The governing load case during this scenario is when the environmental load conditions get severe, for example during a heavy storm. In that case, the structure has to withstand high environmental loads, maximum wave height and high wind speeds. The vessel is not nearby, so the structure cannot be lifted on deck or a construction barge. This means that the MIF has to survive on its own during stand-alone conditions. [26]

3. MIF with Monopile at Refusal Condition with Intermediate Penetration During Survival Conditions

The possibility exists that during the driving of the monopile, failure of equipment occurs. In that case the vessel has to leave the installation site to travel back to shore to get the equipment repaired or replaced. When the vessel has left the installation site, the MIF stands alone and has to survive with a relatively unstable monopile inside of the frame.

Prior to the installation of a monopile, the weather forecast for the coming days is checked. If heavy weather is expected, the installation process will be postponed to prevent survival conditions to

happen during the installation process. When equipment needs onshore repairs, the vessel has to return to the offshore installation site in a certain time period, usually 2 to 3 days. Since the duration of the absence of the vessel is short, it can be guaranteed that the environmental conditions do not exceed the survival conditions.

The governing load case during this scenario is when during the refusal state the significant wave height is 3.50 meters. The conditions that occur when the significant wave height reaches 3.50 meters are the most severe conditions the structure has to be able to withstand while a monopile is present in the MIF.

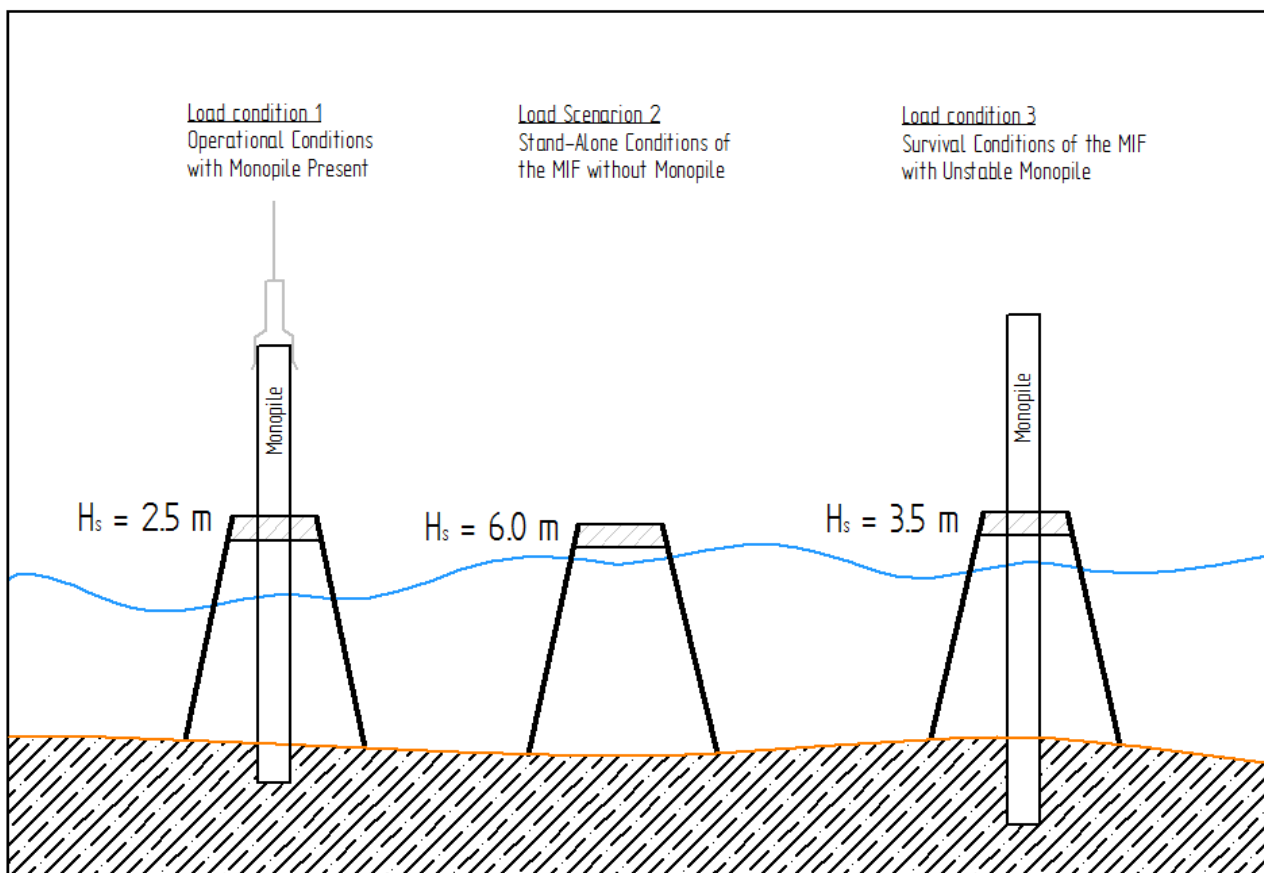


Figure 6-1 - Load Scenarios

6.2.1 Ultimate Load Case

In order to determine the ultimate load case for the MIF, a global load analysis has been done with help of the calculation program SACS. In this program, the structure can be built after which different environmental load cases can be applied. This includes wind loadings, wave loadings and current loadings. After running the calculation, the forces inside all members can be obtained. In this manner it has been determined that the governing ultimate load case is during operational conditions.

During operational conditions, there is a monopile present in the frame which doesn't have a big penetration into the soil, see Figure 6-1. This means that all wave, currents and wind loading will be transferred to the MIF.

During the survival case, there is also a monopile present in the frame. However, it can be assumed that the monopile has a bigger penetration compared to the penetration during operational conditions. In the survival load case, part of the loading will be transferred to the soil. This means that the loading on the frame will be less.

During the stand-alone load case, no monopile is present. This means that the MIF will not have a big surface area. This has as a consequence that the loading due to wind, waves and currents will be much less compared to the situations when a monopile is present in the frame.

6.3 Hydrodynamic Loads

Different hydrodynamic loads act on the structure. The most interesting zone of the MIF is the part of the structure which is in the 'splash zone'. The 'splash zone' includes the part of the structure from above the mean water level down to where the structure is completely submerged. [28]

6.3.1 Wave Loads

The total force due to wave loads consists of three important parts: the inertia force, the drag force and the wave slamming force. In order to calculate the inertia and the drag force, Morison's Load Formula can be used. The wave slamming force has to be calculated separately and must be added to the inertia and drag force in order to obtain the total wave load onto a structure. The procedure of calculation of the wave loads in combination with current is done in the following sections according to ISO-19902. [29]

6.3.1.1 Wave Theories

First of all, the applicable wave theory must be determined in order to calculate the wave loads. This determination is necessary to be able to calculate important wave parameters including for instance wavelengths and particle velocities.

The determination of the applicable wave theory can be done with *Det Norske Veritas*. [30] For the determination of the applicable wave theory, three wave parameters have to be calculated. These wave parameters determine which wave theory to apply in a specific situation. The parameters are the wave height H , the wave period T and the water depth d and are used to define three non-dimensional parameters that determine ranges of validity of different wave theories. [30]

1. Wave steepness parameter

$$S [-] = 2\pi * \frac{H}{g * T^2} \tag{6-1}$$

In which:

$H [m]$ = trough – to – crest wave height

$g \left[\frac{m}{s^2} \right]$ = acceleration of gravity

$T [s]$ = wave period

2. Shallow water parameter

$$\mu [-] = 2\pi * \frac{d}{g * T^2} \tag{6-2}$$

In which:

$d [m]$ = mean water depth

3. Ursell number

$$U_R [-] = \frac{H * \lambda^2}{d^3} \tag{6-3}$$

In which:

$\lambda [m]$ = wave length = $c * T$

$c \left[\frac{m}{s} \right]$ = phase velocity

The given water depths, wave heights and wave periods are stated in 12.1.2.1 and 0. With these values, the three parameters can be calculated. For the determination of the valid wave theory only the wave steepness parameter and the shallow water parameter are necessary. The calculations are done for deep water and for both the operational condition and the survival condition. Water depth is considered to be deep when the following condition is met:

$$d > \frac{\lambda}{2} \tag{6-4}$$

6.3.1.2 Determination of Applicable Wave Theory

In order to determine the applicable wave theory Figure 6-2 has been used, see also 12.1.2.5. The horizontal axis states values for the shallow wave parameter and the vertical axis states values for the wave steepness parameter. In Table 6-1, the different values are displayed.

Table 6-1 - Determination Applicable Wave Theory

Condition	H_{max}/T^2	d_{20}/T^2	d_{42}/T^2
Operational	0.098	0.42	0.88
Survival	0.097	0.30	0.62
Standalone	0.20	0.36	0.75

As can be seen in Figure 6-2 with the given values for the depth, wave height and wave period we have to account for the third or the second-order Stokes wave theory.

6.3.1.3 Determination of Wave Loads

Slender bodies, which can be termed as 'hydrodynamic transparent' have no significant influence on the wave field. In the case of slender bodies, forces induced by waves can be calculated using Morison's Load Formula. [31]

According to *Det Norske Veritas*, Morison's Load Formula is applicable when the wavelength is larger than five times the diameter, or another cross-sectional dimension, of the member. [30]

Thus:

$$\lambda > 5 * D$$

6-5

In which:

D [m] = diameter of typical cross – sectional dimension

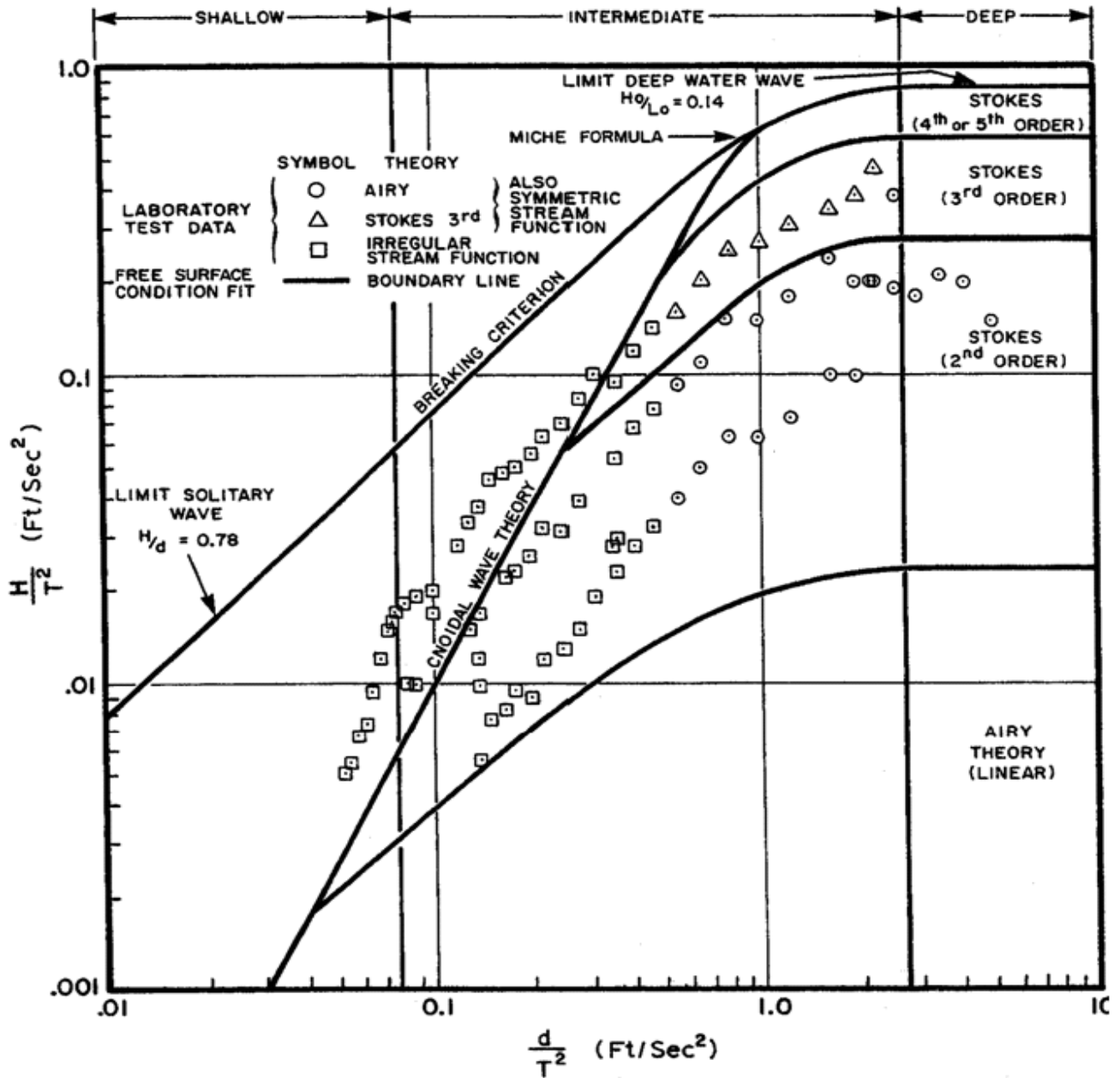


Figure 6-2 - Ranges of Validity for Various Wave Theories [30]

6.3.2 Morison's Load Formula

Morison's Load Formula will be used to calculate the loads due to the waves. This formula is the sum of an inertia force proportional to the local flow acceleration and a drag force being

$$F_{waves} \left[\frac{N}{m} \right] = F_{inertia} + F_{drag} \quad 6-6$$

proportional to the square of the flow velocity. Morison's Load Formula is given as follows:

The formula can be separated in two parts: the inertia force $[N]$ and the drag force $[N]$. [32]; [30]

1. Inertia force

$$F_{inertia} \left[\frac{N}{m} \right] = C_m * V * \rho * \frac{du}{dt} \quad 6-7$$

In which:

C_m [-] = inertia coefficient

V [m^3] = volume of the body

ρ [$\frac{kg}{m^3}$] = mass density of the fluid

$\frac{du}{dt}$ [$\frac{m}{s^2}$] = horizontal wave – induced water particle acceleration

2. Drag force

$$F_{drag} \left[\frac{N}{m} \right] = \frac{1}{2} * \rho * C_d * A * u * \left| \sqrt{((\varphi_{spreading} * u + BF * U)^2 + \varphi_{spreading} * v^2)} \right| \quad 6-8$$

In which:

$\varphi_{spreading}$ [-] = directional wave spreading factor

u [$\frac{m}{s}$] = horizontal wave – induced water particle velocity

BF [-] = current blockage factor

U [$\frac{m}{s}$] = current velocity at depth where 'u' is being determined

v [$\frac{m}{s}$] = vertical wave – induced water particle velocity

C_d [-] = drag coefficient

6.3.3 Currents Loads

The loading due to currents does not require extra calculations, since the force due to the currents is included in the Morison Load Formula. The total velocity in the Morison Load Formula includes both the wave velocity and the currents velocity. An extra calculation of the currents load would therefore lead to an overestimation of the loads. [32]; [33]

The following data is provided of the currents:

Table 6-2 - Currents Data

Elevation	Maximum Current [m/s]
Surface	1.2
80% of water depth	1.1
50% of water depth	1.05
20% of water depth	0.9
10% of water depth	0.8
0.01% of water depth	0.6

6.4 Wave Breaking

When taking into account wave loads, the loading due to the breaking of waves has to be taken into account as well. The breaking of waves can generate high impact loadings. Breaking of waves occurs when the wave gains more energy, gets unstable and dissipates the energy in the form of turbulence. Breaking of waves depends on the water depth, the wave height, the sea bed slope, the wave period and the steepness of the wave. [34]

The steepness of a wave can be calculated by multiplying the amplitude 'a' of the wave by the wave number 'k'. The typical steepness of a breaking wave has a value of $a \cdot k \sim 0.42$. [35] To determine whether or not it is necessary to include loadings due to wave breaking, the steepness of the waves is calculated. The values for the steepness of the waves have been summarized in Table 6-3. Since these values are lower than 0.42, it is not necessary to include wave breaking loads.

Table 6-3 - Wave Steepness

Conditions	Maximum Steepness of the Waves
Operational	$a \cdot k = 0.20$
Stand Alone	$a \cdot k = 0.19$
Survival	$a \cdot k = 0.34$

6.5 Wave Slamming

Although the breaking of waves does not occur, wave slamming always occurs when waves are present since wave slamming is induced by a change in added mass. In the splash zone, submerged structural members are vulnerable to wave impact due to the wave slamming. The force coefficients in Morison's Load Formula cannot describe the impact force of a very short duration, typically in the order of milliseconds. Therefore it is necessary to add an extra term to the Morison's Load Formula to include the impact force effect. [34]

The wave slamming force $[N/m]$ can be calculated using the following formula:

$$F_s \left[\frac{N}{m} \right] = \frac{1}{2} * \rho * C_s * D * v^2 \quad 6-9$$

In which:

$C_s [-]$ = *slamming force factor*

$v \left[\frac{m}{s} \right]$ = *relative velocity between water and member normal to the member surface*

For waves slamming onto a vertical slender structure, the following equation can be used to determine the slamming force factor, or slamming coefficient:

$$C_s(s) [-] = 5.15 * \left(\frac{D}{D+19*s} + \frac{0.107*s}{D} \right) \quad 6-10$$

In which:

$s [m]$ = *penetration distance*

At the start of impact: $C_s(0) = 5.15$. The formula given in 6-10 shall only be applied during penetration of the wave surface, which means: $0 < s < D$. When the cylinder is fully submerged: $C_s(D) = 0.8$. [30]

6.6 Wind Loads

Wind loads on structures are time dependent loads, due to fluctuations in the wind velocity. The wind velocity varies with the elevation, so the height of the structure has to be taken into account. The governing situation regarding wind loads will occur when the monopile has just been hoisted into the frame. At that moment, the monopile will have to resist the highest wind loading during the entire installation process.

To calculate the wind loads on the structure, the following formulas can be used:

$$q_{wind} \left[\frac{N}{m} \right] = \frac{1}{2} * \rho_a * U_T^2 \quad 6-11$$

In which:

$$q_{wind} \left[\frac{N}{m} \right] = \text{basic wind pressure or suction}$$

$$\rho_a \left[\frac{kg}{m^3} \right] = \text{mass density of air for dry air at } 15^\circ C = 1.226$$

$$U_T \left[\frac{m}{s} \right] = \text{the wind velocity averaged over a time interval } T \text{ at a height } z \text{ meter above the mean water level}$$

$$F_W = C_s * q_{wind} * A * \sin(\alpha) \quad 6-12$$

In which:

$$C_s [-] = \text{shape coefficient}$$

$$q_{wind} \left[\frac{N}{m} \right] = \text{basic wind pressure or suction}$$

$$A [m^2] = \text{projected area of the member normal to the direction of the force}$$

$$\alpha [^\circ] = \text{angle between the direction of the wind and the axis of the exposed member or surface}$$

6.7 Load Combinations

Five different load cases have been applied within SACS to the MIF. First of all the dead load of the MIF has been determined. Furthermore, four different environmental combinations have been specified. These four environmental conditions include wave, wind and current forces acting in four different directions on the MIF. The directions in which each combination is applied are stated in Table 6-4 and explained in Figure 6-3. Since the MIF is symmetric, only the right hand side of load directions has been applied to the model in SACS.

It can be assumed that the same load conditions apply for the left hand side.

Environmental load case 2 and 4 are the most severe, since the MIF has the most steel surface in these directions. Therefore, the loads in these directions will be normative. Environmental load condition 1 and 3 will result in torsional forces in the MIF, in which load case 3 will be normative.

Table 6-4 - Direction of Environmental Load Conditions

Environmental Condition	Direction
EN1	45°
EN2	0°
EN3	90°
EN4	180°

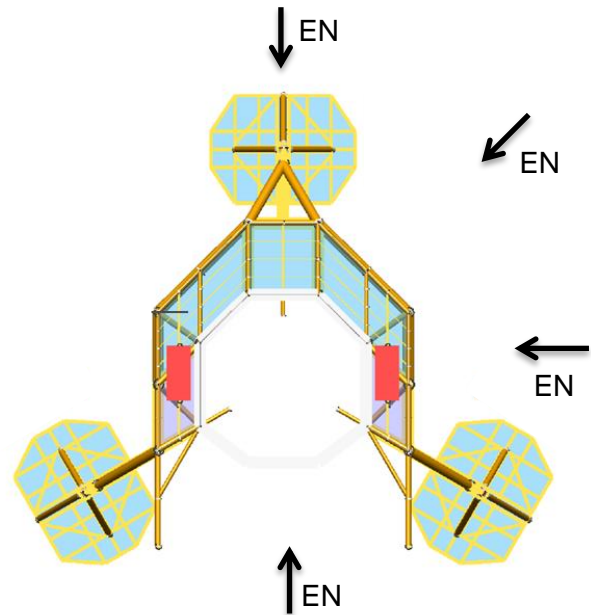


Figure 6-3 – Direction of Environmental Load Conditions Acting on the MIF

The five different load cases have been converted into four load combinations. These combinations include the four different environmental load cases that have been combined with the dead load. Also, a load safety factor has been applied within these combinations:

$$CM_{1,2,3,4} = 1.3 * EN_{1,2,3,4} + 1.0 * Dead Load \tag{6-13}$$

These combinations can be applied to the structure in the calculation program SACS. After running the analysis in SACS, the response of the structure per member to these loads is known and can be used in the next stages of the thesis. All the details and values of the load cases have been summarized in Attachment 12.1.2. The connection will be optimized first for the ultimate load case.

The loads acting on the structure can be determined with help of SACS, which has been earlier described in 6.7.

6.8 Loads Applied on the Connection

The loads that are acting on the members in the ultimate load case can be obtained from the SACS analysis. In SACS, a model of the MIF has been used with extension piece. This will lead to the highest forces applied to the structure, since more surface area will be exposed to wind, wave and currents loading.

The loads that will be evaluated are the loads acting at the ends of the members that will be connected with the bolted flange connection. These members have been colored red in Figure 6-4. The member end forces of these red members have been evaluated. It was clear to notice that the member end forces of the lower members were higher than the member end forces of the upper members.

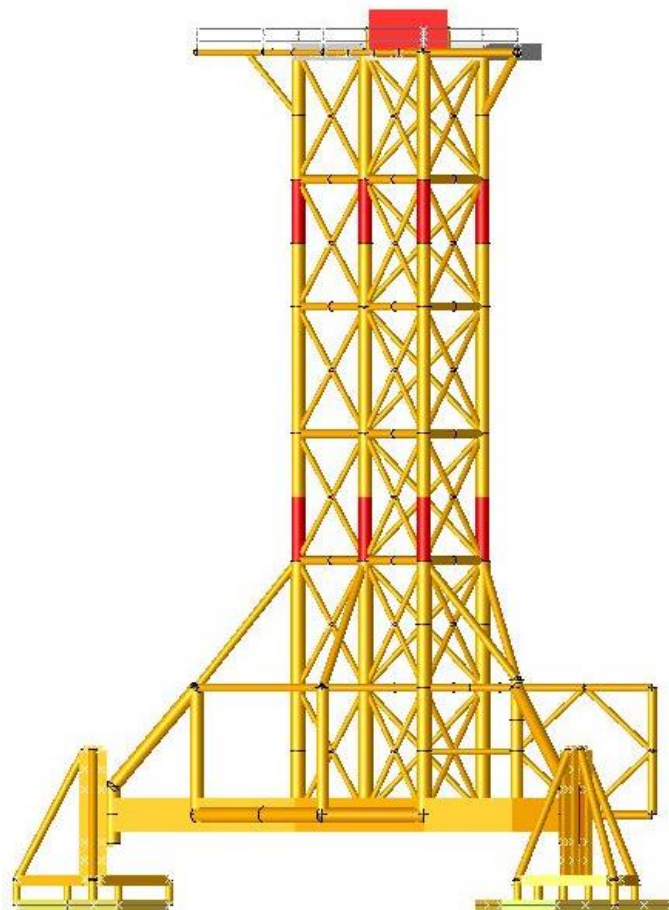


Figure 6-4 - Evaluated Members

7 Verification Failure Modes

In order to verify the connection with respect to the failure modes, the ultimate load case values and the initial geometry are necessary input. The ultimate load case values are stated in 6.8, the initial geometry is obtained using design rules and further explained in the following section.

7.1 Initial Geometry

The initial geometry is based on the rules stated by Ir. M. Seidel in Reference [24], see also Figure 3-12. As a starting point, it is assumed that M24 bolts will be used for the design. The design of the connection has been made based on a set size of the tube. The tube will have an outer diameter of 914 mm and the thickness of the shell of the tube will be 20 mm.

With the given rules, an initial geometry has been determined which is summarized in Table 7-1. Further details of the connection such as the bolt type and the corresponding sizes are also given in Table 7-1. Furthermore, the steel quality used for the flange and shell is S355. The number of bolts assumed is 16.

With these parameters of the geometry known, the fatigue analysis can be made and if necessary optimized.

Table 7-1 - Geometry Details

Geometry detail	Size [mm]
outer diameter tube	914
outer diameter flange	1134
tube thickness	20
a	87
b	50
c	223
c'	197
t	80
b _D	50
b _E	32.5
R	447
bolt diameter	24
bolt hole diameter	26
washer diameter	44
height of bolt head	20
height of washer	4

7.2 Failure Modes Bolted Flange Connection

The following sections will explain the failure modes and state the corresponding formulas.

7.2.1 Failure Modes A, B and C

Before the initial design can be used as starting point for the fatigue analysis, it has to be checked for certain failure modes. These failure modes are stated and explained in the following sections. The check with respect to the failure modes of the initial design has been given in the Attachment 12.4. Three different failure modes can be distinguished of which failure mode C can be replaced by two other failure modes, failure modes D and E. Failure modes D and E will be explained in the next section.

7.2.1.1 Failure Mode A

Failure mode A focuses on failure of the bolt and therefore assumes a very stiff flange and a relatively weak bolt. The ultimate force that can be applied until failure is 90% of the yield strength of the bolt. In failure mode A, prying effects due to elastic deformation of the shell and the flange are neglected; see Figure 7-1.

The ultimate load can be determined as follows:

$$F_{U,A} [kN] = F_{t,Rd} = \frac{0.9 * A_s * f_{ub}}{\gamma_{M2}} * 10^{-3} \tag{7-1}$$

In which:

$A_s [mm^2]$ = tensile stress area of the bolt

$f_{ub} [\frac{N}{mm^2}]$ = ultimate tensile strength of the bolt

$\gamma_{M2} [-]$ = safety factor bolt = 1.25

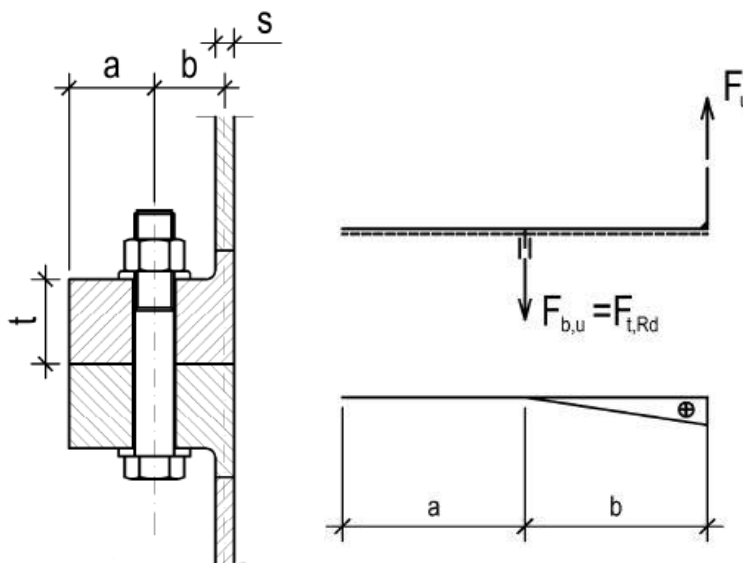


Figure 7-1 - Failure Mode A [24]

7.2.1.2 Failure Mode B

Failure mode B focuses on bolt failure and the formation of a plastic hinge in the shell, which can occur simultaneously; see Figure 7-2. The ultimate force that can be applied depends therefore on a combination of failure of the bolt and prying effects in the connection.

The ultimate load can be determined with a moment equilibrium:

$$F_{U,B} [kN] = \frac{F_{t,Rd} * a + M_{pl,3}}{a+b'} * 10^{-3} \quad 7-2$$

In which:

$F_{t,Rd} [kN]$ = tensile strength of bolt

$M_{pl,3} [Nmm]$ = bending resistance of shell or flange, considering $M - N$ and $M - V$ interaction respectively

$a [mm]$ = flange end to bolt axis

$b [mm]$ = bolt axis to halfway shell thickness

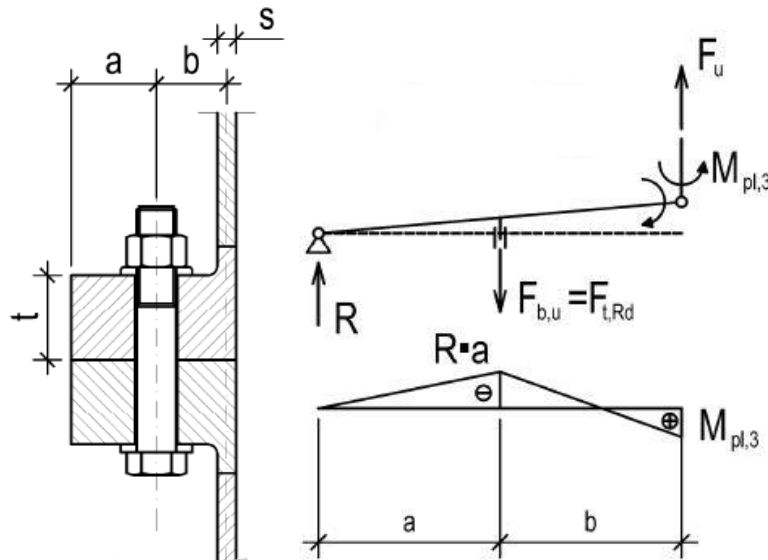


Figure 7-2 - Failure Mode B [24]

The bending resistance of the shell or the flange, $M_{pl,3}$ can be determined as follows:

$$M_{pl,3} = \min \left\{ \begin{array}{l} \left(1 - \left(\frac{F_u}{N_{pl,Rd,shell}} \right)^2 \right) * M_{pl,Rd,shell} \\ \left(\sqrt{1 - \left(\frac{F_u}{c * t * f_{yd,flange}} \right)^2} \right) * M_{pl,Rd,flange} \end{array} \right. \quad 7-3$$

In which:

$$M_{pl,Rd,shell} [Nmm] = \frac{c * s^2}{4} * f_{yd,shell}$$

$$N_{pl,Rd,shell} [N] = c * s * f_{yd,shell}$$

$$M_{pl,Rd,flange} [Nmm] = \frac{c * t^2}{4} * f_{yd,flange}$$

$$c [mm] = \text{width of the segment} = \frac{(d_{outer,flange} - s) * \pi}{n_{bolts}}$$

$$t [mm] = \text{flange thickness}$$

$$s [mm] = \text{shell thickness}$$

$$f_{yd,shell} \left[\frac{N}{mm^2} \right] = \text{design strength shell} = \frac{f_{y,shell}}{\gamma_{M0}}$$

$$f_{y,shell} \left[\frac{N}{mm^2} \right] = \text{yield strength of steel}$$

$$f_{yd,flange} \left[\frac{N}{mm^2} \right] = \text{design strength flange} = \frac{f_{y,shell}}{\gamma_{M0}}$$

$$f_{y,flange} \left[\frac{N}{mm^2} \right] = \text{yield strength of steel}$$

$$\gamma_{m0} [-] = \text{safety factor steel} = 1.15$$

$$n_{bolts} [-] = \text{bolt number}$$

7.2.1.3 Failure Mode C

Failure mode C focuses on the formation of plastic hinges in both the shell and in the flange at the centerline of the bolt; see Figure 7-3. Due to the formation of the plastic hinge in the bolt axis, no prying effects are taken into account. Since the assumption that the plastic hinge will form at the bolt axis is conservative, failure mode C can be replaced by failure mode D and E.

The ultimate load can be determined with a moment equilibrium:

$$F_{U,C} [kN] = \frac{M'_{pl,2} + M_{pl,3}}{b} * 10^{-3} \quad 7-4$$

In which:

$$M'_{pl,2} [Nmm] = \text{reduced bending resistance of flange at the bolt axis}$$

$$M_{pl,3} [Nmm] = \text{bending resistance of shell or flange, considering } M - N \text{ and } M - V \text{ interaction respectively}$$

The reduced bending resistance of the flange can be determined as follows:

$$M'_{pl,2} = M_{pl,Rd,flange,net} = \frac{c' * t^2}{4} * f_{yd,flange} \tag{7-5}$$

In which:

$$c' [mm] = \text{reduced segment width} = \frac{(d_{outer,flange} - s) * \pi}{n_{bolts}} - d_{bolt}$$

$$d_{bolt} [mm] = \text{bolt diameter}$$

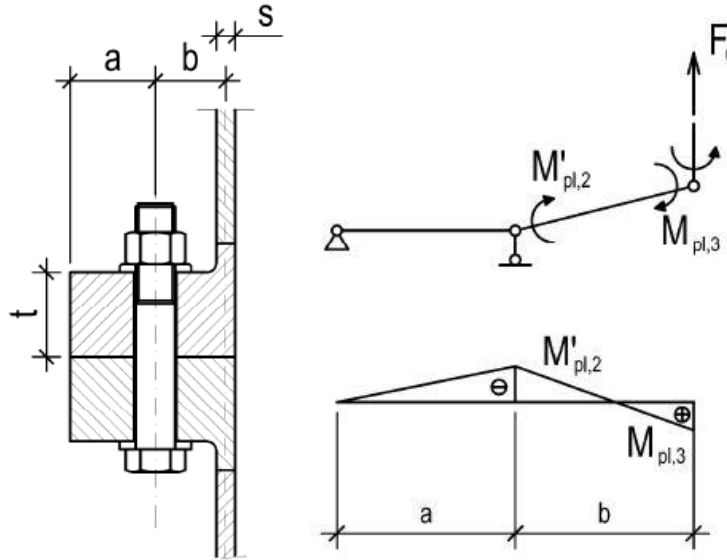


Figure 7-3 - Failure Mode C [24]

7.2.2 Failure Modes D and E

Failure modes D and E can be used instead of failure mode C. these failure modes take the presence of the washer into account. However, the failure modes are allowed to use only when the requirements as stated in the following sections are met.

7.2.2.1 Failure Mode D

Failure mode D focuses on the formation of a plastic hinge in both the shell and the flange while taking into account the presence of the washer; see Figure 7-4. This is done by the use of an additional resistance moment in the line of the washer.

The ultimate load can be determined with a moment equilibrium:

$$F_{U,D} [kN] = \frac{M'_{pl,2} + \Delta M_{pl,2} + M_{pl,3}}{b'_D} * 10^{-3} \tag{7-6}$$

In which:

$M'_{pl,2}$ [Nmm] = reduced bending resistance of flange at the bolt axis

$\Delta M_{pl,2}$ [Nmm] = additional resistance moment

$M_{pl,3}$ [Nmm] = bending resistance of shell or flange, considering $M - N$ and $M - V$ interaction respectively

In which the additional resistance moment can be determined as follows:

$$\Delta M_{pl,2} = \frac{F_{t,Rd}}{2} * \frac{d_w + d_H}{4} \quad 7-7$$

In which:

d_w [mm] = diameter of washer

d_H [mm] = diameter of bolt hole

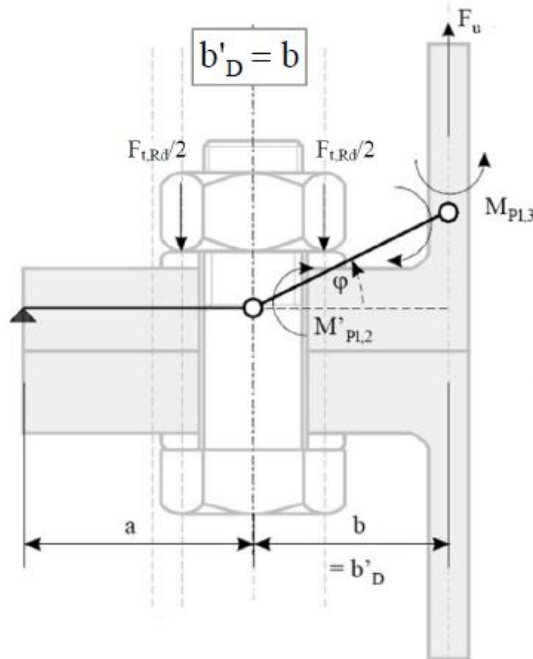


Figure 7-4 - Failure Mode D [24]

Failure mode C can only be replaced by failure mode D when the following conditions are met:

- The full bending moment of the flange does not exceed $M_{pl,2}$ at mid-washer:

$$\left(\frac{F_{t,Rd}}{2} - F_{U,D} \right) * \frac{d_w + d_H}{4} \leq M_{pl,2} - M'_{pl,2} \quad 7-8$$

If this condition is not met, failure mode E will be normative.

- The reaction force r has to act on the flange:

$$r = \frac{(M'_{pl,2} + \Delta M_{pl,2})}{F_{t,Rd} - F_{U,D}} \leq a \quad 7-9$$

7.2.2.2 Failure Mode E

Failure mode E focuses on the formation of a plastic hinge in both the shell and the flange while taking into account the gross-section next to the bolt hole instead of the net cross-section in the bolt line. This has as result that the lever arm is also reduced; see Figure 7-5.

The ultimate load can be determined with a moment equilibrium:

$$F_U = \frac{M_{pl,2} + M_{pl,3}}{b'_E} * 10^{-3} \tag{7-10}$$

In which:

$$b'_E \text{ [mm]} = b - \frac{d_W + d_H}{4}$$

$$M_{pl,2} \text{ [Nmm]} = \text{full bending moment resistance of flange}$$

The full bending moment resistance of the flange can be determined as follows:

$$M_{pl,2} = M_{pl,Rd,flange} = \frac{c * t^2}{4} * f_{yd,flange} \tag{7-11}$$

Failure mode C can only be replaced by failure mode E when the following conditions are met:

- The bending moment in the bolt axis does not exceed $M'_{pl,2}$:

$$\left(\frac{F_{t,Rd}}{2} - F_{U,E} \right) * \frac{d_W + d_H}{4} \geq M_{pl,2} - M'_{pl,2} \tag{7-12}$$

- The reaction force r has to act on the flange:

$$r = \frac{(M'_{pl,2} + 2 * \Delta M_{pl,2})}{F_{t,Rd} - F_U} - \frac{d_W + d_H}{4} \leq a \tag{7-13}$$

If the requirements of failure mode D and failure mode E cannot be met, failure mode C has to be used.

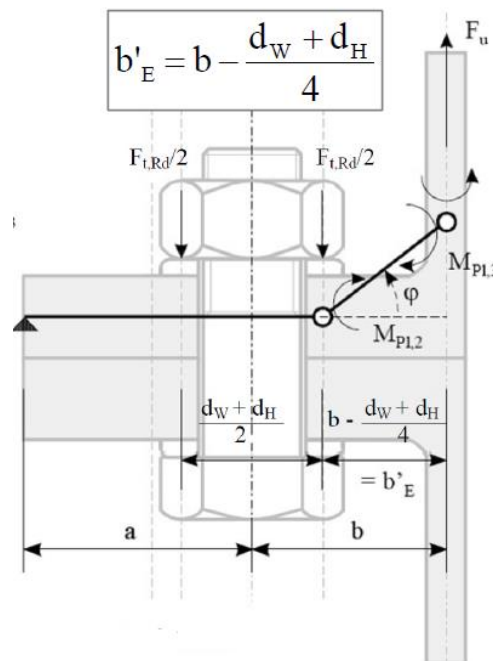


Figure 7-5 - Failure Mode E [24]

8 Fatigue Lifetime

The determination of the lifetime of the MIF will be done using a fatigue analysis. This fatigue analysis will be executed for the machined connection. The MIF will undergo different types and magnitudes of loading. The stress ranges that occur during the different cycles can be determined per member with help of SACS which has been earlier described in 6.7. The different cycles can be used to determine a lifetime for the structure.

8.1 Introduction

The fatigue analysis consists of different steps for which input is needed. This needed input exists of the SCF of the connection and a wave scatter diagram. The SCF will be obtained from ANSYS, the wave scatter diagram is obtained from data provided by Seaway Heavy Lifting.

The fatigue analysis is done only considering environmental loadings: wind, waves and currents. Besides these loadings, vibrations due to hammering of the monopiles will occur. The hammering of the monopile is expected to have an impact on the structure. However, the vibrations due to hammering will be absorbed by the water, the monopile, the soil and the lower part of the MIF. It is assumed for this fatigue analysis that the influence of hammering loads on the connection is negligible.

For the fatigue analysis first of all the type of structural category must be determined. This will be done with help of EN-1993-1-9: Design of Steel Structures. When the structural category is known, the corresponding S-N-curve can be determined. Then, the amount of actual cycles must be calculated for a certain time period with help of the wave scatter diagram after which the corresponding stress ranges during these cycles can be obtained. These stress ranges can be multiplied with the SCF, which is obtained using ANSYS.

When the stress ranges are known, the amount of cycles until failure can be calculated. The actual damage to the structure can then be determined by dividing the actual number of cycles by the amount of cycles until failure. With the damage known for a certain time period, the life time of the structure can be calculated.

If the lifetime is less than wanted, or a lot more than wanted the model needs to be optimized. This can be done by changing the SCF, see Figure 5-1.

8.2 Structural Detail Category

For the determination of the structural detail category, the EN-1993-1-9: Design of Steel Structures is used. [36] In this document several structural detail categories are stated, with their corresponding S-N-curve. When the structural category is known, the necessary data for the calculation of the amount of cycles until failure can be calculated with help of the given S-N-curve of the particular category.

For the structural detail category, the machined part of the connection is observed, see Figure 8-1. The determination of structural detail categories is done for both the tube-to-flange junction and the tube-to-flange junction, see Figure 8-2.

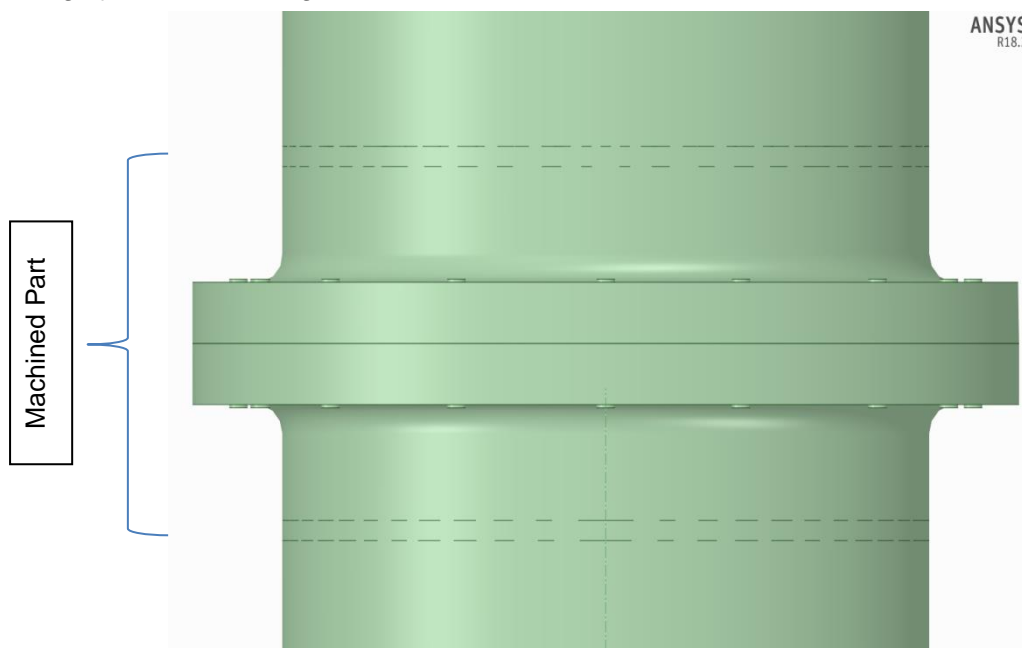


Figure 8-1 - Machined Part

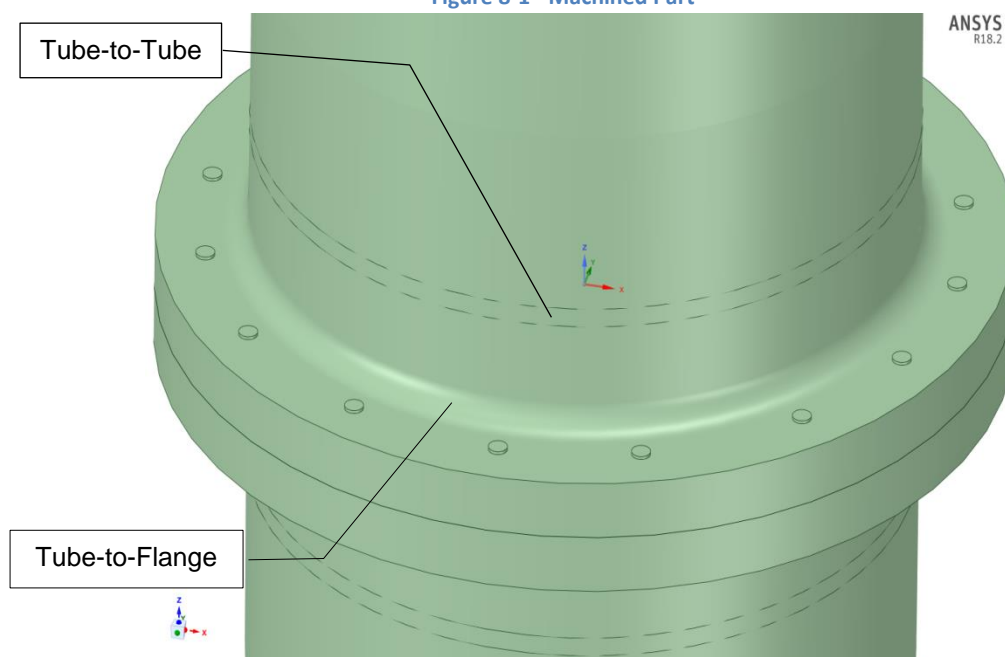


Figure 8-2 - Junctions of the Connection

8.2.1 Derivation Structural Detail Category Tube-to-Flange Junction

The machined tube-to-flange junction that is studied during the thesis is not present in the structural detail categories. An interesting option to choose is detail category 160, see Figure 8-3. Category 160 focuses on rolled sections that have not been modified. When applying a stress concentration factor, detail category 160 would be a good assumption. However, since the connection is not an unmodified section but a machined section, this choice for category 160 would be too optimistic. Therefore, the assumption is made to go for detail category 140, see Figure 8-4.

160	<p>NOTE The fatigue strength curve associated with category 160 is the highest. No detail can reach a better fatigue strength at any number of cycles.</p>	<p><u>Rolled and extruded products:</u></p> <ol style="list-style-type: none"> 1) Plates and flats; 2) Rolled sections; 3) Seamless hollow sections, either rectangular or circular. 	<p><u>Details 1) to 3):</u></p> <p>Sharp edges, surface and rolling flaws to be improved by grinding until removed and smooth transition achieved.</p>
-----	---	---	--

Figure 8-3 - Structural Detail Category 160 [36]

140		<p><u>Sheared or gas cut plates:</u></p> <ol style="list-style-type: none"> 4) Machine gas cut or sheared material with subsequent dressing. 5) Material with machine gas cut edges having shallow and regular drag lines or manual gas cut material, subsequently dressed to remove all edge discontinuities. <p>Machine gas cut with cut quality according to EN 1090.</p>	<p>4) All visible signs of edge discontinuities to be removed. The cut areas are to be machined or ground and all burrs to be removed.</p> <p>Any machinery scratches for example from grinding operations, can only be parallel to the stresses.</p> <p><u>Details 4) and 5):</u></p> <ul style="list-style-type: none"> - Re-entrant corners to be improved by grinding (slope $\leq \frac{1}{4}$) or evaluated using the appropriate stress concentration factors. - No repair by weld refill.
125		<p>Machine gas cut with cut quality according to EN 1090.</p>	<p>Machine gas cut with cut quality according to EN 1090.</p>

Figure 8-4 - Structural Detail Category 140 [36]

Category 140 is applicable to rolled sections, but in this category it is assumed that the sections are modified. The modification is assumed to be a machined gas cut. The gas cutting process is associated with high temperatures and pollution of the steel, which will affect the properties of the material along the cut.

The machining process and the gas cut process will both lead to a different roughness of the surface. This surface roughness is important in order to predict the chance on crack initiations. The surface roughness due to machining is in between 6.3 μm and 0.8 μm . The surface roughness due to gas cutting is between 50 μm and 6.3 μm , see Figure 8-5. Seaway Heavy Lifting requires a surface roughness of 3.2 μm . The surface roughness of machining will be well below the surface roughness of gas cutting. The result is that the chance of crack initiation for the machined part is lower than for a gas cut part. This means that the detail category is actually accounting for a surface roughness that is worse than the machined surface roughness. This has as a consequence that the S-N-curve of category 140 will result in pessimistic results regarding the life time.

It can be concluded that a special category derived from category 140 is the most representative and safe choice for the machined part although it will lead to conservative results. Since the bolted flange connection will be machined and will not have gas cuts, it is likely that the properties of the studied bolted flange connection will in reality be better than assumed in category 140. When using detail the derived category based on category 140, the SCF must be applied to the stress ranges in order to take into account the presence of the tube-to-flange connection. It is expected that the SCF will have a significance influence on the lifetime.

Detail 140 is used in case of a seamless hollow section; in this case a circular hollow section. This is an optimistic assumption, since the connection studied in the thesis is not a seamless hollow section as given in Figure 8-4. It is assumed that the connection that is studied can only be compared with a seamless circular hollow section if the SCF is taken into account. This can be done by multiplying all stress ranges by their SCF values. This will take into account the influence that the tube-to-flange junction has on the distribution of stresses. Using the SCF in the structural detail category changes the structural detail category. This means that for the tube-to-flange junction a special category is derived, that can be used in case of bolted flanges.

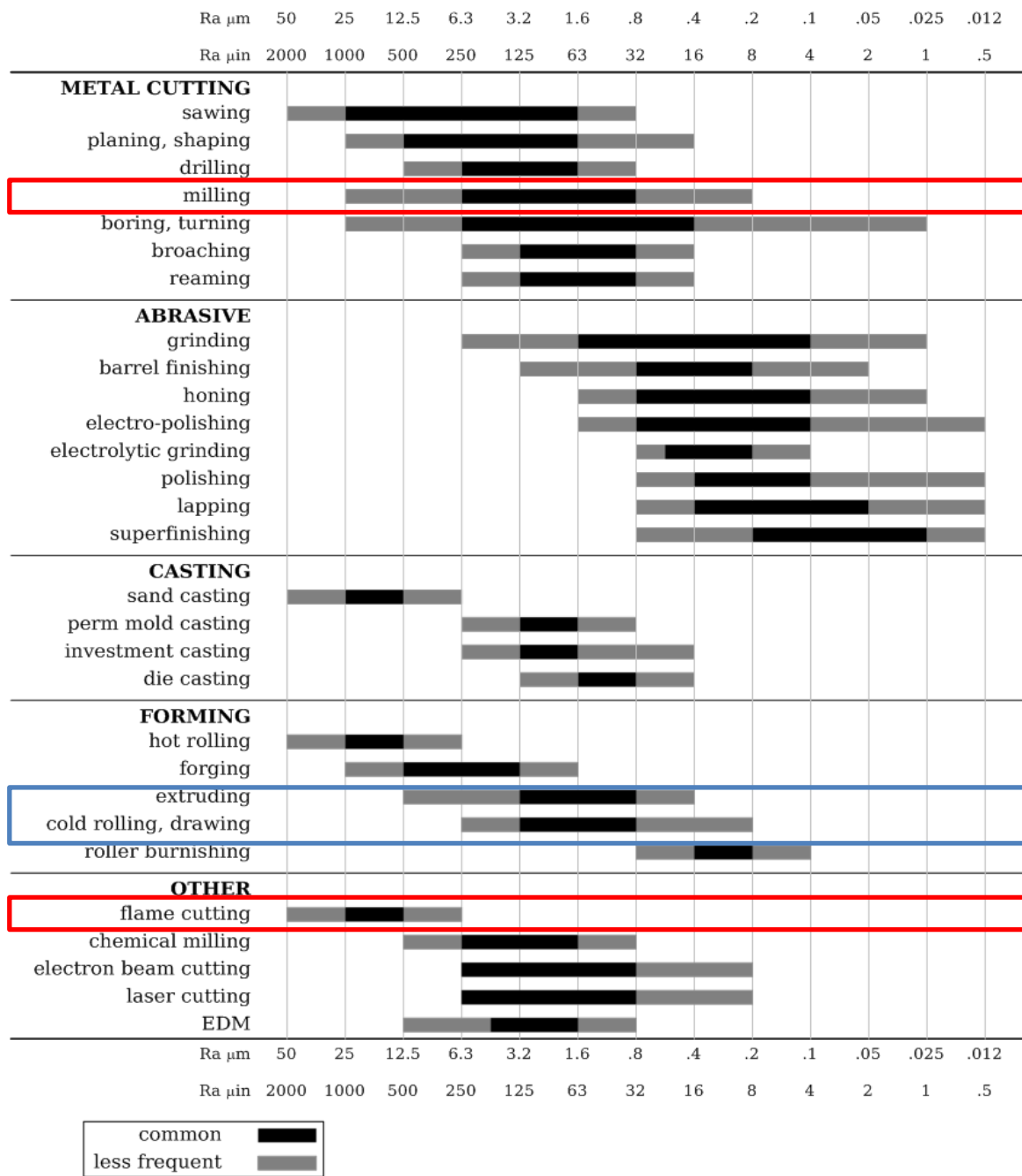


Figure 8-5 - Surface Roughnesses per Modification Process

8.2.2 Structural Detail Category Tube-to-Tube Connection

The machined part with the bolted flange connection will be connected to the main member by welding. This connection, the tube-to-tube connection, also needs a fatigue analysis. It is important that the calculated life time of the tube-to-tube connection is not lower than the life time calculated for the tube-to-flange connection.

The tube-to-tube connection is represented by detail category 71. Due to the weld, the structural detail class is much lower than for a rolled section. The zone around the weld is a heat affected zone, where the properties of the material are less good than in the rest of the section. Therefore, the structural properties of the zone will be lower. This results in a lower S-N-curve compared to detail category 140, see Figure 8-14.

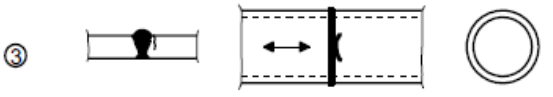
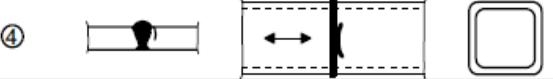
71		<p><u>Transverse butt welds:</u></p> <p>3) Butt-welded end-to-end connections between circular structural hollow sections.</p>	<p><u>Details 3) and 4):</u></p> <ul style="list-style-type: none"> - Weld convexity $\leq 10\%$ of weld width, with smooth transitions. - Welded in flat position, inspected and found free from defects outside the tolerances EN 1090.
56		<p>4) Butt-welded end-to-end connections between rectangular structural hollow sections.</p>	<ul style="list-style-type: none"> - Classify 2 detail categories higher if $t > 8$ mm.

Figure 8-6 - Structural Detail Category 71 [36]

The machining of the connection instead of welding will result in a more smooth distribution of stresses. When using detail 71, it isn't necessary to apply the SCF to the stress ranges, since this is already implemented in the S-N-curve of the structural category.

8.3 Stress Concentration Factor

The stress concentration factor, SCF, can be obtained by using ANSYS. The initial geometry is modelled in ANSYS and two load steps are applied: first a pretension load applied to the bolt and second a tension load applied to the tube. The assumption is made, based on experience by Seaway Heavy Lifting, that the maximum pretension value is a too high assumption, since they don't want to pretension the bolt to that value. The maximum pretension value is given by:

$$F_p = 70\% * \text{ultimate tensile strength bolt} = 0.7 * A_{\text{bolt}} * f_{\text{ultimate, bolt}}$$

For the pretension load, the following value is assumed which is equal to 50% of the ultimate tensile strength of the bolt:

$$F_p = 50\% * \text{ultimate tensile strength bolt} = 0.5 * A_{\text{bolt}} * f_{\text{ultimate, bolt}}$$

For the tensile loading to the tube, the highest occurring load has been used. As earlier stated, the highest loads to the structure occur during the operational load case. With help of SACS, the highest occurring tensile load has been obtained in the members which will be connected by the bolted flange connection, see Figure 8-7.

In this case, the highest axial tensile stress has been chosen. However, also moments occur in the member. These moments have been decoupled and added to the axial tensile force. In reality, half of the member will be loaded in tension and half of it in compression. The assumption that the full

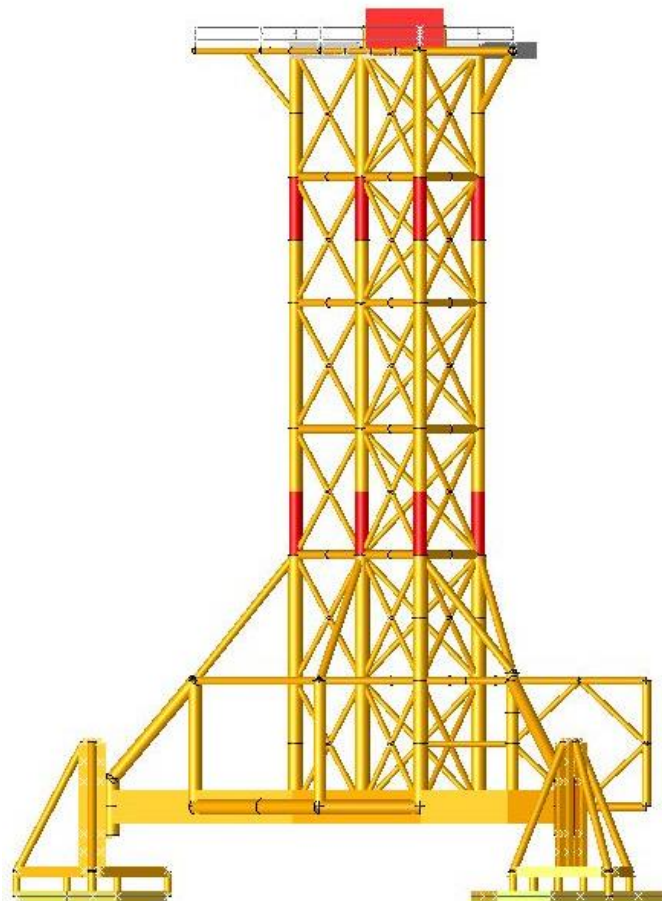


Figure 8-7 - Locations Connection Members

decoupled moment will result in tension is therefore conservative.

8.3.1.1 Determination SCF

The total axial tensile load has been converted into a stress, by dividing the axial force over the surface area of the tube. This resulted in a stress of 34.7 MPa, which has been applied to the model in ANSYS; see Figure 8-8.

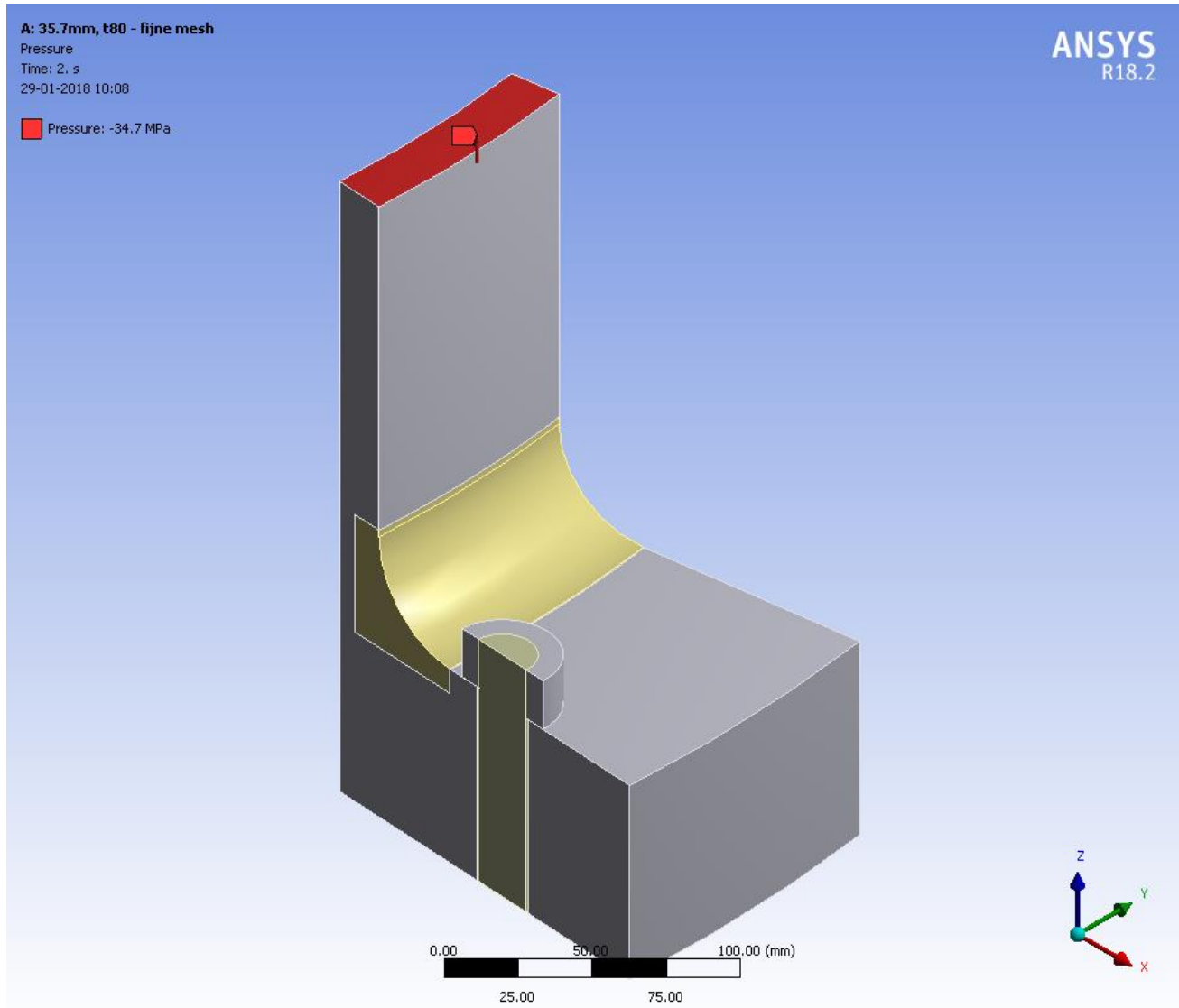


Figure 8-8 - Pressure Applied to the Model in ANSYS

Besides tensile loading, also compression loading occurs in the members. Since the distribution of compression stress will be different compared to tensile stresses, a SCF for compression must be calculated. This has been done in the same way as for the tensile stresses.

Once the finite element calculation is completed, the stress distribution in the model can be studied. The distribution of stresses in case of a tensile load applied to the structure is displayed globally in Figure 8-9 and more detailed in Figure 8-10.

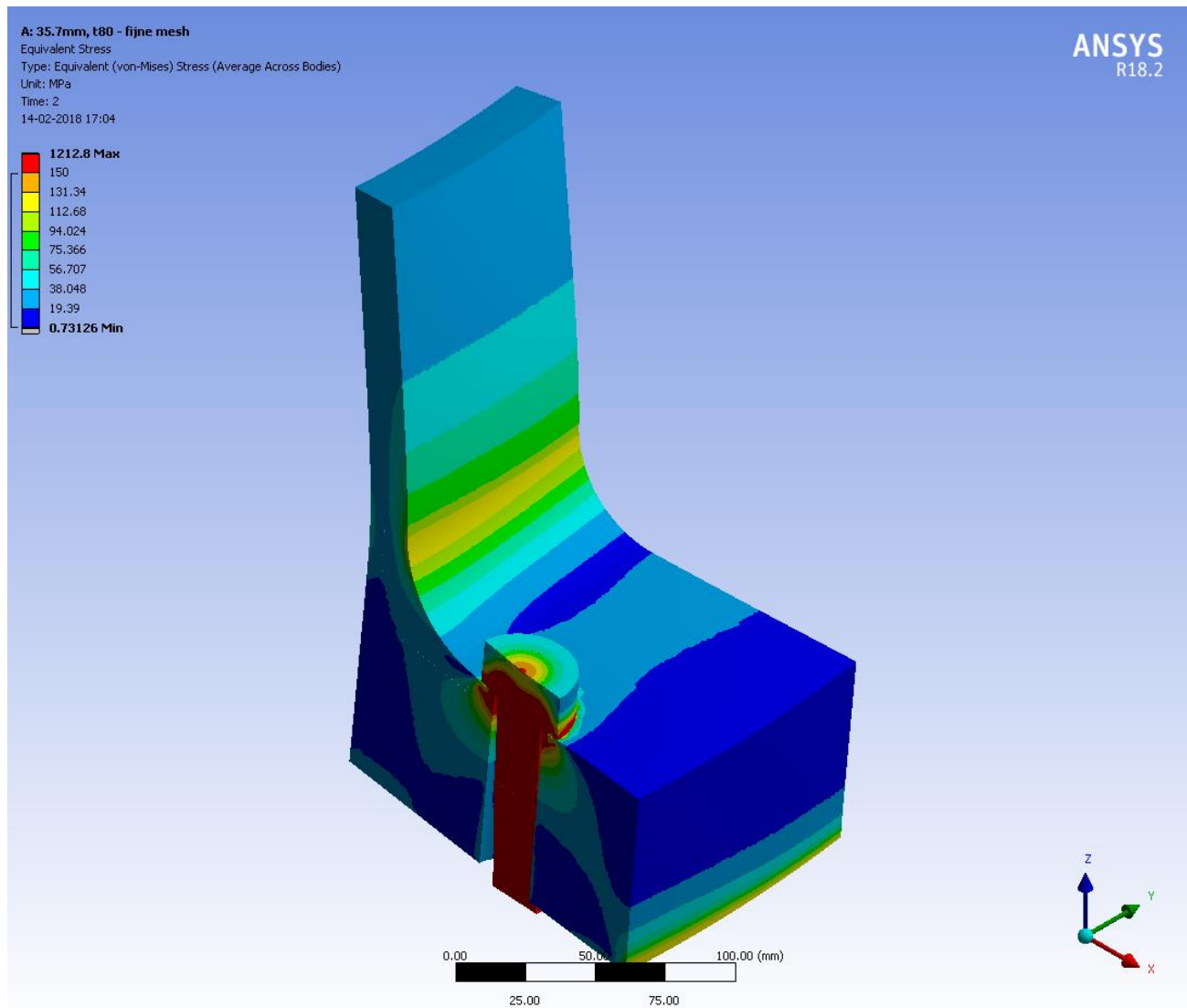


Figure 8-9 - Stress Distribution for Tensile Loading

The SCF for both tension and compression stresses can be found using the stress distribution in the tube-to-flange junction. The SCF is found by dividing the maximum stress found in the radius by the applied stress:

$$SCF = \frac{\text{Maximum stress}}{\text{applied stress}} = \frac{122.77}{35} = 3.51$$

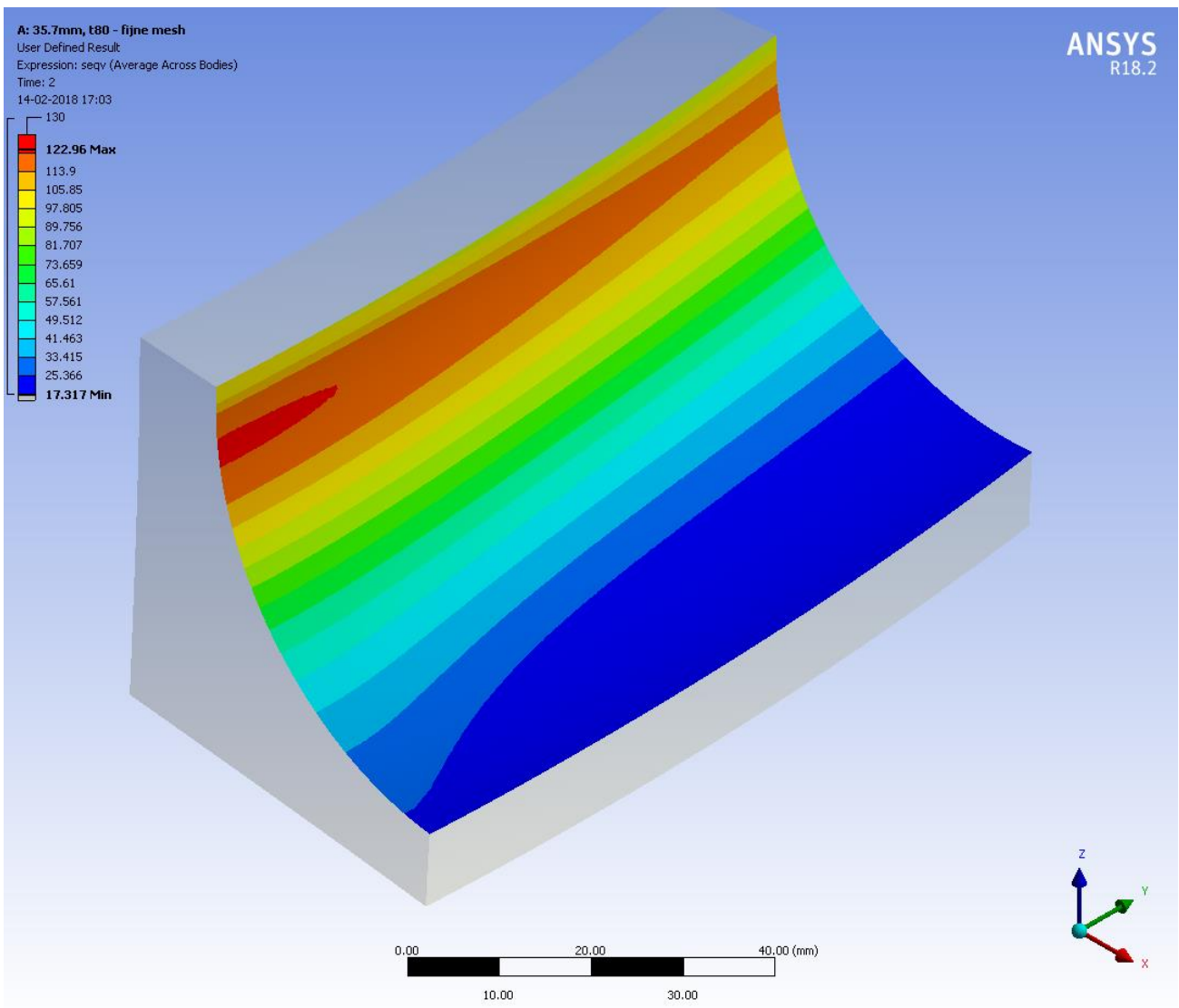


Figure 8-10 - Stress Distribution for Tensile Loading – Radius Tube-to-Flange Junction

8.3.1.2 SCF Refinement

It is found that the accuracy of the SCF depends on the refinement of the mesh applied to the model. The finer the mesh, the more accurate the SCF results are. A coarser mesh will give less accurate values for the stress distribution. Using a coarse element size requires the FEM-calculation to average lots of results to get one elemental average. This has as a consequence that the final value isn't accurate. The use of smaller elements results in less values being used to obtain the elemental average.

A refinement study has been done for both the SCF in case of tensional loading and the SCF in case of compressional loading, see Figure 8-11 and Figure 8-12. The results are obtained from ANSYS and shown in Attachment 12.5.1.

From Figure 8-11 and Figure 8-12 it can be seen that the influence of the mesh refinement is more significant in case of tensional loading. This can be explained by the concentration of stresses that occurs when applying tensional loading. Therefore, the tensional SCF is governing for the fatigue analysis since it will have a significant influence on the results. The compressional SCF needs to be used to multiply the compression stresses with.

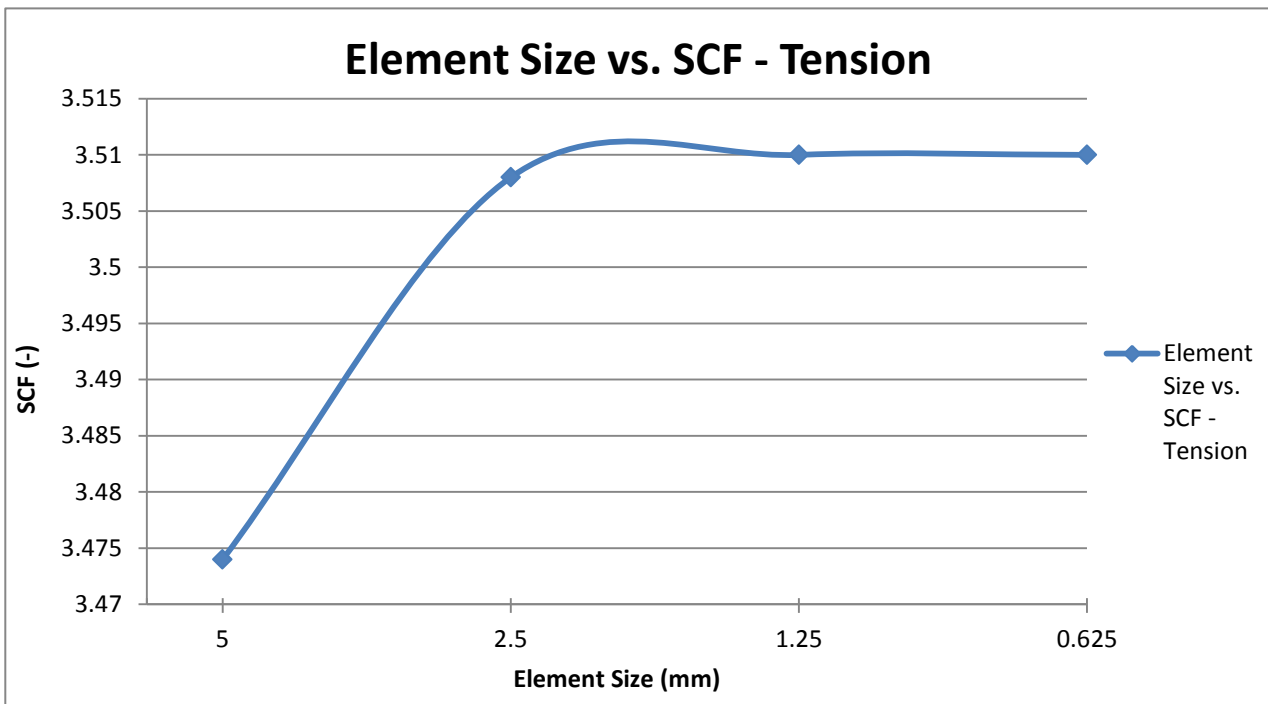


Figure 8-11 - Influence of Mesh Refinement on SCF- Tension

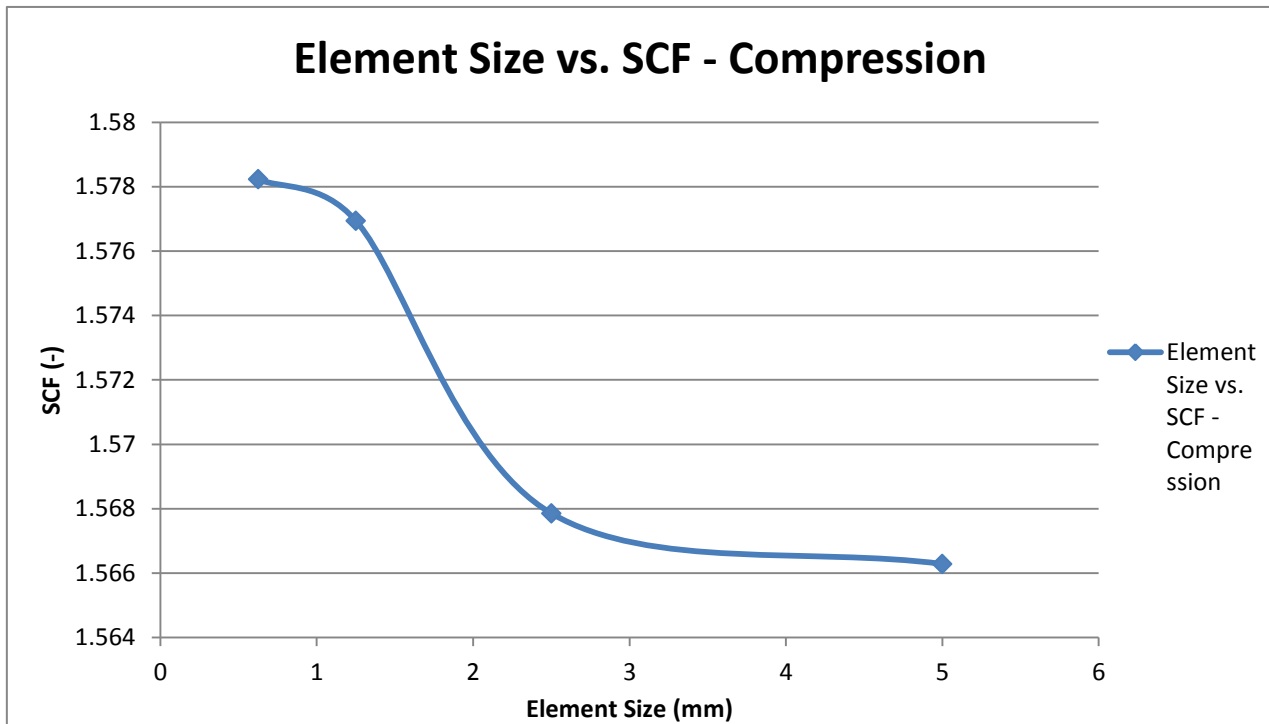


Figure 8-12 - Influence of Mesh Refinement on SCF - Compression

8.4 Wave Scatter Diagram

The wave scatter diagram is based on the data of certain wave heights with certain time periods in a period of 6 months. This data has been obtained by measurements of Seaway Heavy Lifting. In a wave scatter diagram, the amount of waves with a particular wave height and time period have been stated, see Figure 12-8 .

Per time period, different wave heights occur. All different wave heights between $H_s = 0.10$ m and $H_s = 4.40$ m with an interval of 0.10 m have been counted. This results in a diagram in which for each time period all waves are counted with a certain wave height. In a time period, waves with a certain wave height occur the most often, which is for that time period the equivalent wave height, H_{eq} . These governing, or equivalent, wave heights can be calculated with help of stated rules in DNV-GL-RP-C205: Environmental Conditions and Environmental Loads. [30]

In order to determine the stress ranges that occur in the MIF during its lifetime, all equivalent wave heights must be calculated. Then, these 19 equivalent wave heights and their time periods have been used as input for SACS. With help of SACS, the stress ranges in the members that will be connected by the bolted flange connection, see Figure 8-7, can be determined. For each equivalent wave height the stress range can be obtained which will be used to determine the amount of cycles to failure of the MIF.

8.5 Actual Cycles

The actual amount of cycles happening during 6 months can be determined with help of the wave scatter diagram. In the wave scatter diagram 19 equivalent wave heights with their corresponding time periods have been stated. The equivalent wave heights and their time periods have been marked by a trend line, see Figure 12-8. Each occurring wave with a certain wave height and period has been counted.

Per time period, the equivalent wave height has an occurrence of the total amount of waves that occurs in 6 months with that time period. This means that in the wave scatter diagram, the sum of a column is the total amount of waves with the equivalent wave height of that column. The different significant wave heights and their period and occurrence are stated in Table 12-23.

8.6 Stress Ranges

In order to calculate the influence of fatigue onto the structure, the stress ranges that occur during the 19 different equivalent wave heights need to be determined. The stress range of a member is the difference of its maximum tensile stress and its maximum compression stress. These stress ranges of the 19 different equivalent wave heights are displayed in Figure 8-13.

In case of using a structural detail category that doesn't include a SCF, first the tensile stresses need to be multiplied by their tensile SCF and the compression stresses by their compression SCF before calculating the stress range. Once these stress ranges are known, the amount of cycles until failure can be calculated.

The stress ranges during the equivalent wave heights can be determined with help of SACS. The different wave heights with their corresponding wave period have been put into SACS as load input. Then, with help of SACS, the member forces can be determined for each member that will be a part of the connection, see Figure 8-7.

This results in 19 different SACS calculations, each with 16 observed members. For all these 19 calculations, the member with the highest stress range is picked. These 19 stress ranges are then used to calculate the amount of cycles to failure. When determining the stress ranges, the decoupled moments have been added to the tension stress. This is a conservative assumption, since half of the decoupled moments will cause compression stress and the other half tension stresses.

For the calculation of the cycles to failure for detail category 140, the stress ranges need to be multiplied with the SCF. This is necessary since the detail category doesn't account for the concentration of stresses since the category has been design for a tube without any changes of geometry. Detail category 71 doesn't need any additional SCF, since that is implemented in the detail already.

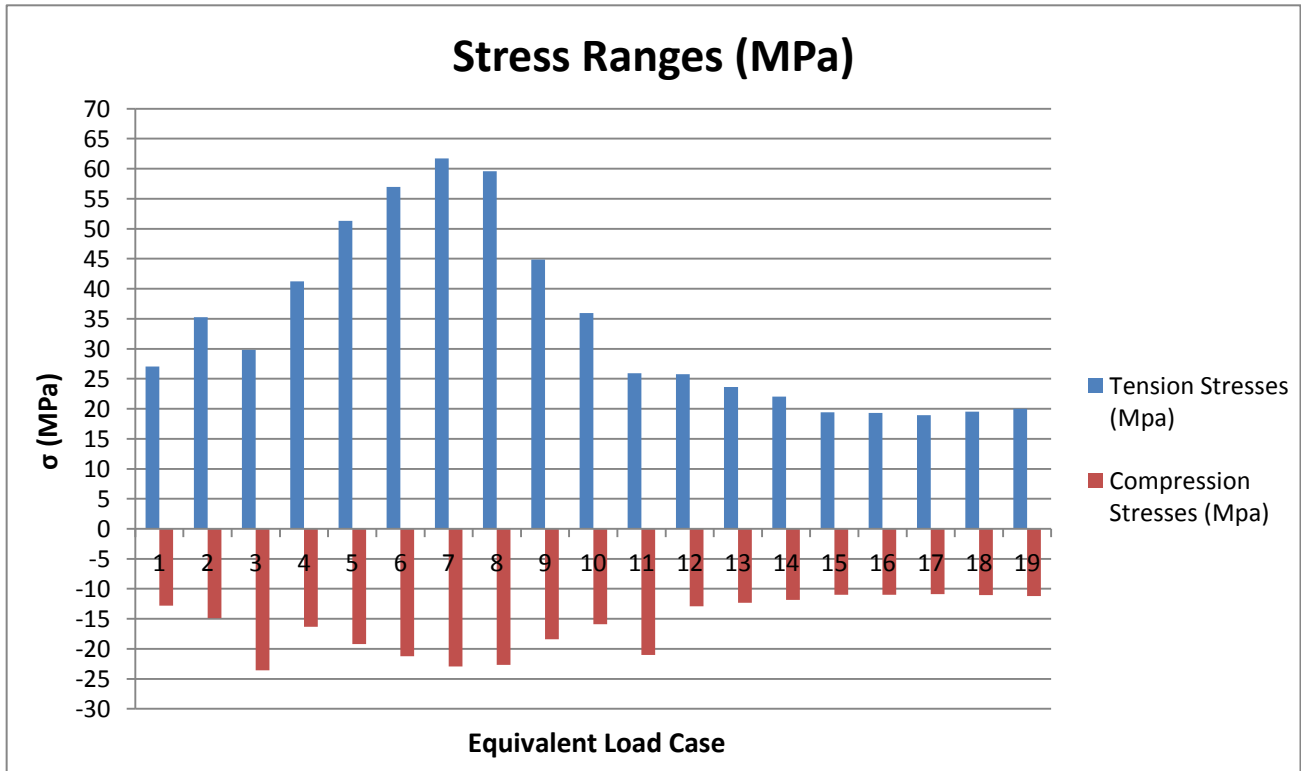


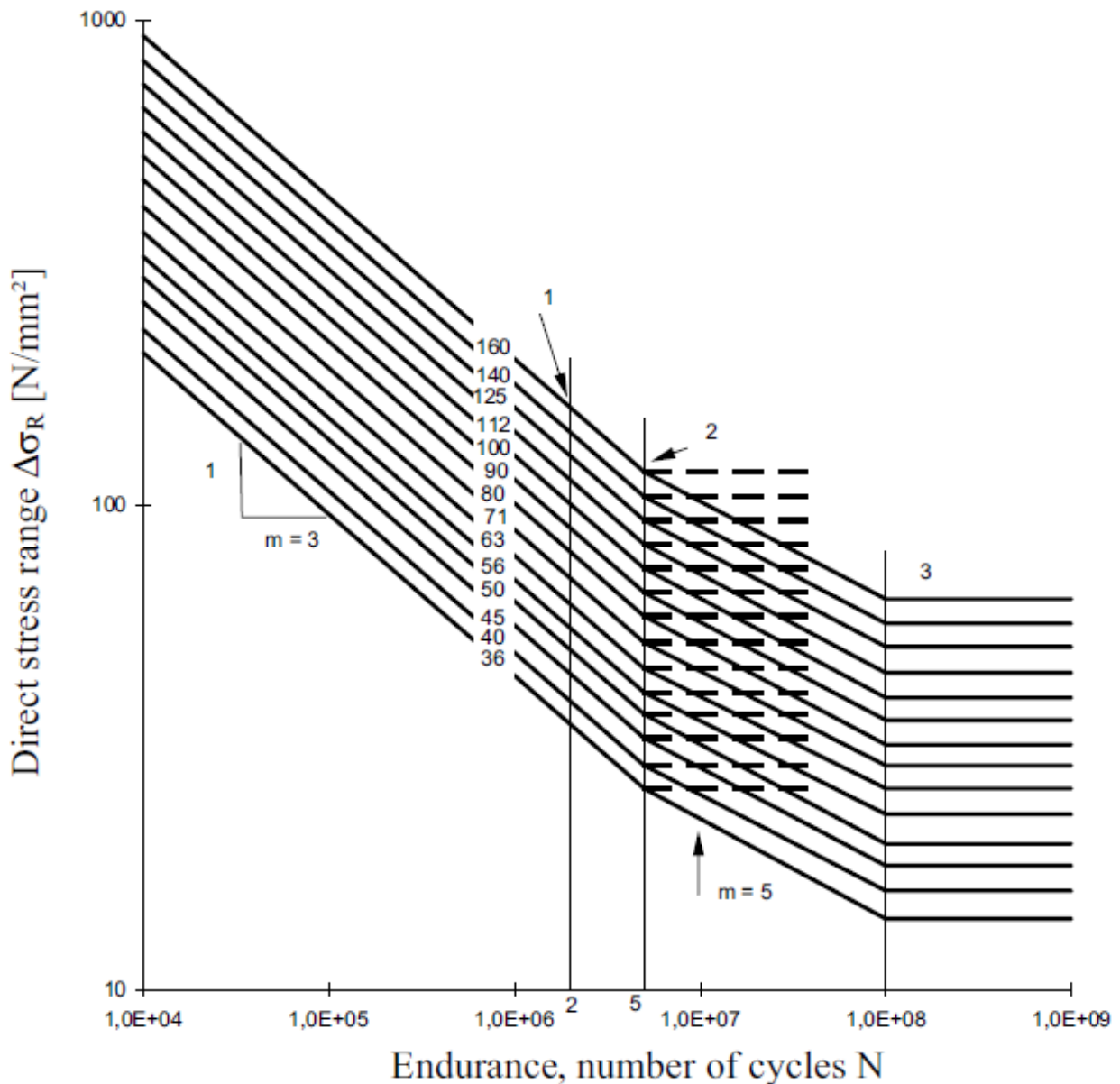
Figure 8-13 - Stress Ranges (MPa)

8.7 Cycles to Failure

The amount of cycles to failure needs to be calculated in order to calculate the damage that is done to a structure in a certain time period. The amount of cycles that is occurring during the 6 months' time period that is observed in the thesis is already known. With help of the rules stated in DNV-GL-RP-C203: Fatigue Design of Offshore Steel Structures, [37], the amount of cycles to failure can be calculated with:

$$\log N = \log a - m * \log \Delta\sigma$$

In which log a and m are parameters that can be obtained from the S-N-curves since the stress ranges are known, see Figure 8-14. For the amount of cycles to failure for the connection observed in this thesis, the S-N-curve of detail category 140 and 71 is observed.



8.8 Damage and Lifetime

Once the amount of cycles to failure is known, together with the amount of cycles that is happening during 6 months, the damage can be calculated. This will give the percentage of damage that occurs in 6 months' time. Then, it can be calculated how many months need to pass in order to get a 100% damage to the structure. This amount of months is the lifetime of the structure. An example calculation for one equivalent wave height has been given in 12.5.1.

8.9 Optimization Fatigue Lifetime

The fatigue lifetime will be calculated for two structural categories: number 140 and 71. For detail category 140, the stress ranges need to be multiplied with the SCF. This has a big influence on the lifetime of the structure. The higher the SCF is, the shorter the lifetime will be. Therefore, if the lifetime isn't satisfying, it can be optimized by decreasing the SCF. This can be done by optimizing the radius of the tube-to-flange junction, which will lower the stress concentration. However, the amount of increase of the radius is bound by both the failure mode unity checks and the execution of fastening the bolts. In order to fasten the bolts, there must be some space between the bolt and the tube wall. Also, the fastener cannot be used on a tilted surface. It is assumed that a spacing of 15 mm is sufficient. [38] It is expected that the structure will be used for a time period of more or less 8 years. Therefore, it is desirable to have a fatigue life time around 9 years. The first model that has been made in ANSYS has been made according to the initial geometry, which is given in Table 7-1.

This initial geometry resulted in a high SCF, since the initial geometry has been designed with a negligible radius. Therefore, an optimized model has been made in which the radius of the tube-to-flange junction was increased. This was done by moving the location of the bolt farther away from the tube. However, this second attempt still gave a relatively high SCF in case of tension and thus a low lifetime. A third, and final model, was made with a radius of 36 mm. This gave satisfying results for both the SCF and the fatigue lifetime. The optimization is bound by the failure modes. Changing the position of the bolt changes the geometry of the connection and will therefore has an influence on the unity checks of the three failure modes. It was found that failure mode B is governing. The unity check of failure mode B, see also 7.2.1.2, has for the final design a value of 0.82.

The influence of the increasing radius on the SCF-values is shown in Figure 8-16. The influence of the SCF on the lifetime of the structure has been displayed in the graph in Figure 8-17. For the final model, also a failure mode validation has been made. The different SCF values for the different used geometries are given in Table 8-1.

Table 8-1 - SCF - Values per Geometry

Geometry	a	b	radius (mm)	SCF - compression	SCF - tension
Initial Geometry	87	50	5	2.36	7.50
Optimized Geometry	72	65	26	1.66	5.15
Final Geometry	65	72	36	0.5	3.51

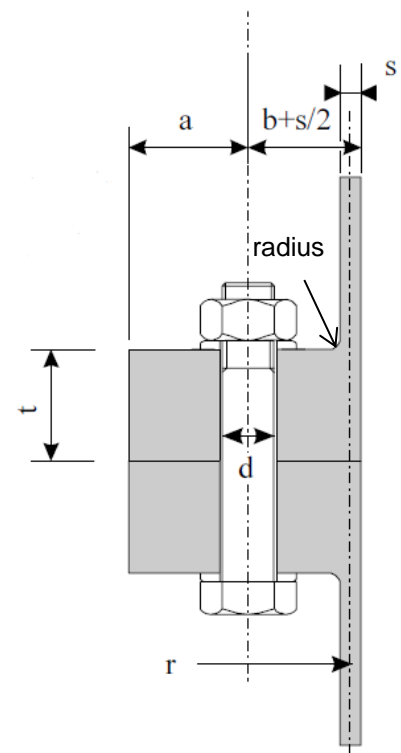


Figure 8-15 - Geometry Details

The different lifetimes per structural detail are given in Table 8-2.

Table 8-2 - Lifetime per Geometry

Geometry	Category 71	Category 140
Initial Geometry	17 years	0.8 years
Optimized Geometry	17 years	2.4 years
Final Geometry	17 years	9 years

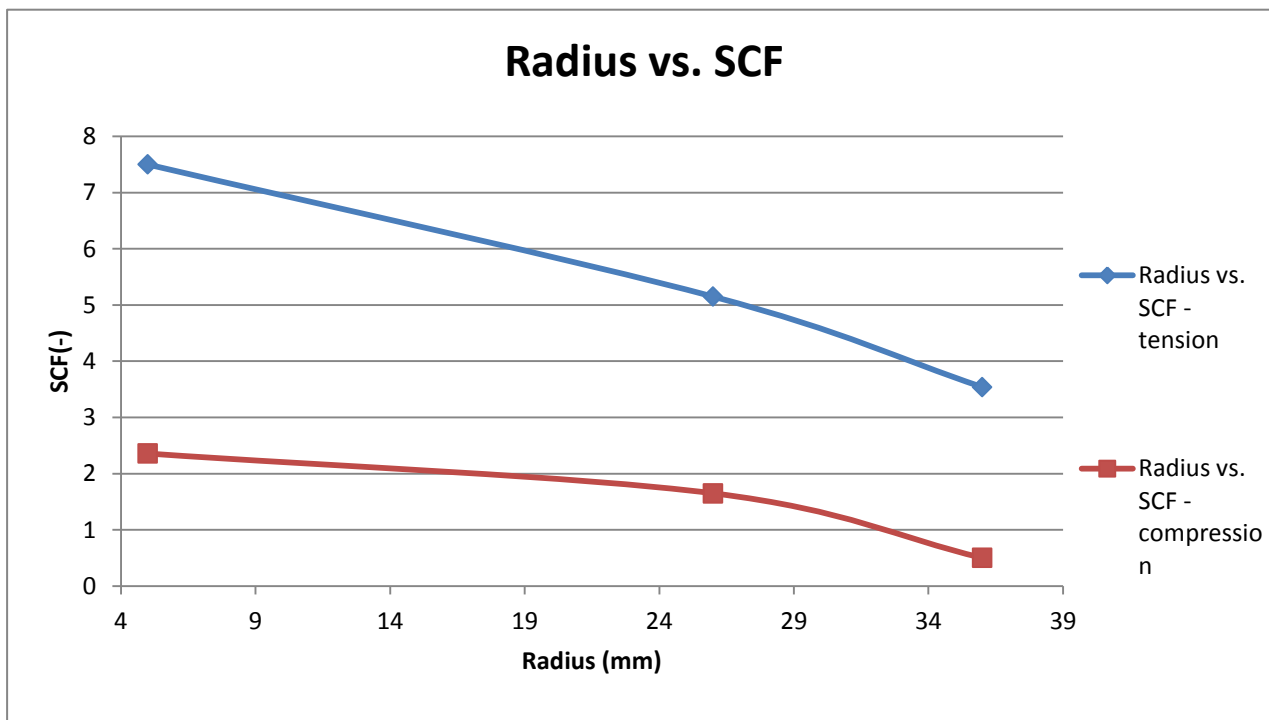


Figure 8-16 - Influence Radius on Stress Concentration Factor

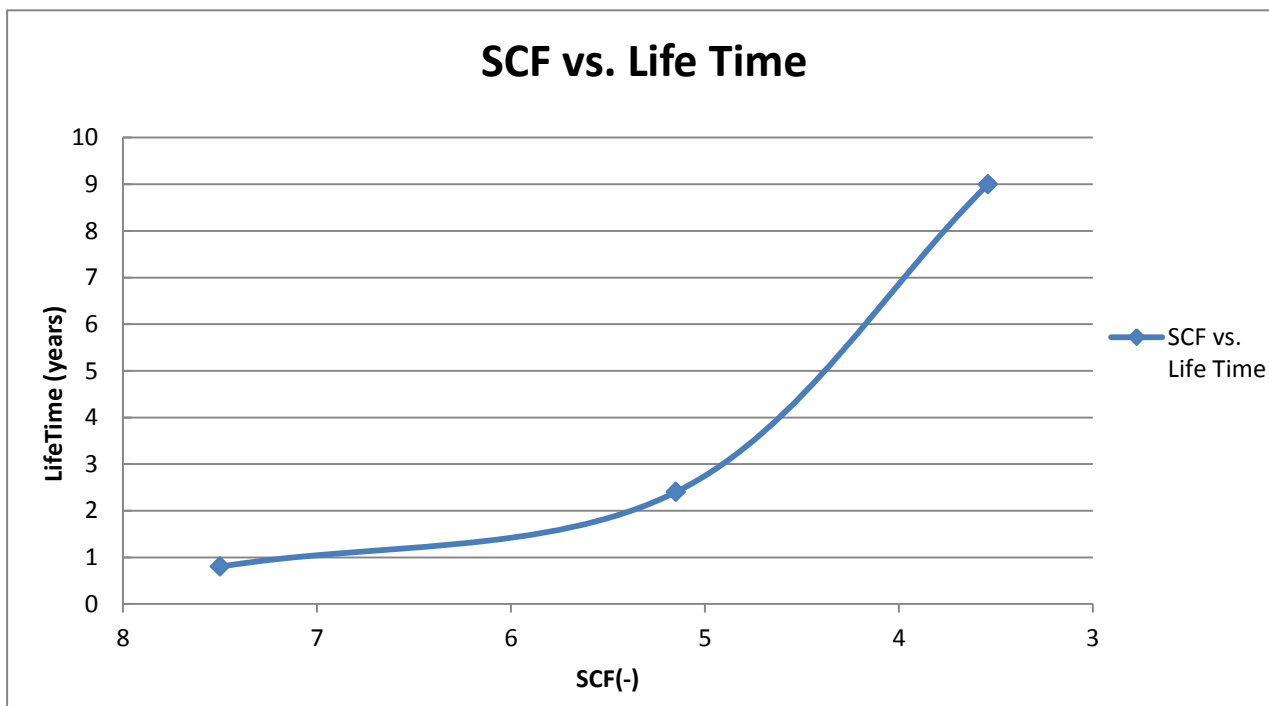


Figure 8-17 - Influence SCF - Tension on Lifetime

8.10 Validation Failure Modes Final Model

In order to be sure the final model can be safely used in the MIF, it has to be checked with respect to the failure modes.

8.10.1 Geometry Final Design

The tube will have an outer diameter of 914 mm and the thickness of the shell of the tube will be 20 mm. All final geometry characteristics are summarized in Table 8-3. For the final design, the bolt size, bolt quality and bolt number is set, which is respectively M24, 8.8 and 16.

Table 8-3 - Geometry Characteristics Final Design

Geometry detail	Size [mm]
outer diameter tube	914
outer diameter flange	1134
tube thickness	20
a	65
b	72
c	229
c'	203
t	80
b _D	72
b _E	54.5
R	447
bolt diameter	24
bolt hole diameter	26
washer diameter	44
height of bolt head	20
height of washer	4

8.10.2 Material Properties

The ultimate tensile strength (f_{ub}) of the bolt is 800 N/mm² and the yield strength (f_{yb}) is 640 N/mm², see Reference [39]. The tensile stress area of the M24 bolt is 353 mm². It is assumed that the bolt has been pre-tensioned with a pretension force of:

$$F_p = 0.5 * A_s * f_{ub} \approx 141200 \text{ N} \approx 141 \text{ kN}$$

The flange has a thickness of 80 mm, which results in a yield strength ($f_{y,flange}$) of 325 N/mm²; see Reference [2]. The shell of the tube has a thickness of 20 mm, which results in a yield strength ($f_{y,shell}$) of 355 N/mm².

8.10.3 Calculation Ultimate Force

For the different failure modes the ultimate force has been calculated which is stated in the following sections.

Failure Mode A

For failure mode A, the ultimate force is equal to:

$$F_{U,A} = F_{t,Rd} = \frac{0.9 * A_s * f_{ub}}{\gamma_{M2}} \approx 203000 \text{ N} \approx 203 \text{ kN}$$

Failure Mode B

The ultimate force for failure mode B can be determined with an iterative process or by substituting $M_{pl,3}$ into the ultimate force equation. In these calculations the latter has been chosen. The bending resistance of the shell has been substituted into the ultimate force equation.

$$\begin{aligned} F_{U,B} &= \frac{F_{t,Rd} * a + M_{pl,3}}{a + b'} \\ &= -\frac{N_{pl,Rd,shell}^2 * (a + b)}{2 * M_{pl,Rd,shell}} + N_{pl,Rd,shell} * \sqrt{1 + \frac{N_{pl,Rd,shell}^2 * (a + b)^2 + 4 * F_{t,Rd} * a * M_{pl,Rd,shell}}{4 * M_{pl,Rd,shell}^2}} \\ &\approx 148 \text{ kN} \end{aligned}$$

Failure Mode C

The ultimate force that is determined for failure mode C is governing when the requirements of failure modes D and E cannot be met. For failure mode C, $M_{pl,3}$ has been substituted into the ultimate force equation.

$$\begin{aligned} F_{U,C} &= \frac{M'_{pl,2} + M_{pl,3}}{b} \\ &= \frac{N_{pl,Rd,shell}^2 * b}{2 * M_{pl,Rd,shell}} + \sqrt{\frac{(N_{pl,Rd,shell}^4 * b^2)}{4 * M_{pl,Rd,shell}^2} + \frac{M_{pl,Rd,flange,net} + M_{pl,Rd,shell}}{M_{pl,Rd,shell}} * N_{pl,Rd,shell}^2} \approx 1293 \text{ kN} \end{aligned}$$

Since the requirements of failure mode D have not been met, see following sections, failure mode C will be used in order to verify the connection.

Failure Mode D

In order to see whether failure mode C can be replaced by failure mode D, the stated requirements have been checked. The requirements can be checked after the ultimate force has been determined. The ultimate force has been determined by substituting $M_{pl,3}$ into the ultimate force equation.

$$F_{U,D} = \frac{M'_{pl,2} + \Delta M_{pl,2} + M_{pl,3}}{b'_D}$$

$$= -\frac{b'_D * N_{pl,Rd,shell}^2}{2 * M_{pl,Rd,shell}} + \frac{b'_D * N_{pl,Rd,shell}^2 * \sqrt{1 - 4 * \frac{M_{pl,Rd,shell}}{b'_D * N_{pl,Rd,shell}^2} * -\frac{M'_{pl,2} + \Delta M_{pl,2} + M_{pl,Rd,shell}}{b'_D}}}{2 * M_{pl,Rd,shell}}$$

$$\approx 1315 \text{ kN}$$

The requirements that need to be met have been checked:

- The full bending moment of the flange does not exceed $M_{pl,2}$ at mid-washer:

$$\left(\frac{F_{t,Rd}}{2} - F_{U,D}\right) * \frac{d_W + d_H}{4} \approx -21200000 \text{ Nmm} \approx -21.2 \text{ kNm}$$

$$M_{pl,2} - M'_{pl,2} \approx 11760000 \text{ Nmm} \approx 11.76 \text{ kNm}$$

The requirement is not met since: $\left(\frac{F_{t,Rd}}{2} - F_{U,D}\right) * \frac{d_W + d_H}{4} > M_{pl,2} - M'_{pl,2}$

- The reaction force r has to act on the flange:

$$\frac{(M'_{pl,2} + \Delta M_{pl,2})}{F_{t,Rd} - F_{U,D}} \approx -84 \text{ mm}$$

$$a = 87 \text{ mm}$$

Due to the relatively small ultimate force in the bolt, this requirement is met.

Failure Mode E

In order to see whether failure mode C can be replaced by failure mode E, the stated requirements have been checked. The requirements can be checked after the ultimate force has been determined. The ultimate force has been determined by substituting $M_{pl,3}$ into the ultimate force equation.

$$F_{U,E} = \frac{M_{pl,2} + M_{pl,3}}{b'_E}$$

$$= -\frac{b'_E * N_{pl,Rd,shell}^2}{2 * M_{pl,Rd,shell}} + \frac{b'_E * N_{pl,Rd,shell}^2 * \sqrt{1 - 4 * \frac{M_{pl,Rd,shell}}{b'_E * N_{pl,Rd,shell}^2} * -\frac{M_{pl,2} + M_{pl,Rd,shell}}{b'_E}}}{2 * M_{pl,Rd,shell}} \approx 1818 \text{ kN}$$

The requirements that need to be met have been checked:

- The bending moment in the bolt axis does not exceed $M'_{pl,2}$:

$$\left(\frac{F_{t,Rd}}{2} - F_{U,E}\right) * \frac{d_W + d_H}{4} = -30040000 \text{ Nmm} = -30.04 \text{ kNm}$$

$$M_{pl,2} - M'_{pl,2} \approx 11760000 \text{ Nmm} \approx 11.76 \text{ kNm}$$

The requirement is met since: $\left(\frac{F_{t,Rd}}{2} - F_{U,E}\right) * \frac{d_W + d_H}{4} > M_{pl,2} - M'_{pl,2}$

- The reaction force r has to act on the flange:

$$\frac{(M'_{pl,2} + 2 * \Delta M_{pl,2})}{F_{t,Rd} - F_{U,E}} - \frac{d_W + d_H}{4} \approx -77 \text{ mm}$$

$$a = 87 \text{ mm}$$

Due to the relatively small ultimate force in the bolt, this requirement is met.

8.10.4 Verification Final Design

The ultimate load case for the monopile installation frame has been determined to be the operational load case. During this load case, the monopile is present within the installation frame. With help of the program 'SACS' a global load analysis has been done. From the global load analysis it was obtained that the values for the ultimate load case are as stated in Table 8-4.

Table 8-4 - Ultimate Load Case

F _{axial} [kN]	F _{y,z} [kN]	F _{total, actual} [kN]
1504	443	1947

8.10.4.1 Unity Check

The final design can be verified by performing a unity check between the actual forces present in the member and the ultimate forces for the different failure modes. The actual force in the member needs to be divided by 16, since the ultimate forces have been calculated per segment of the connection, which is 1/16th.

$$Unity\ Check = \frac{F_{actual}}{F_{ultimate}} \tag{8-1}$$

In which:

$$F_{actual} [kN] = 1947 \text{ kN}$$

$$F_{ultimate} [kN] = \text{Ultimate force for each failure mode}$$

The ultimate forces per failure mode are summarized in Table 8-5.

Table 8-5 - Ultimate Force per Failure Mode

Failure Mode	Ultimate Force [kN]
A	203
B	148
C	1293

The unity checks per failure mode are summarized in Table 8-6.

Table 8-6 - Unity Check per Failure Mode

Failure Mode	Unity Check [-]
A	0.60
B	0.82
C	0.09

From the unity check values in Table 8-6 it can be concluded that the strength requirements for the final model of the connection are fulfilled. In this case failure mode B is the governing failure mode, which means bolt failure and the formation of a plastic hinge in the shell, which can occur simultaneously.

9 Results and Discussion

9.1 Results

The objective of the thesis is to obtain a design of the critical section of the MIF optimized for fatigue. For the connections used to connect the extension piece, which is the critical section of the MIF, a bolted flange connection is chosen. This connection has first been designed with an initial geometry, which has been modelled in ANSYS in order to obtain a stress concentration factor in the tube-to-flange junction. After that, this initial model has been used as a starting point for the fatigue analysis. The radius of the tube-to-flange junction has then been optimized in order to improve the life time of the connection. The result of the analysis is an optimized MIF model, with a fatigue lifetime of 9 years.

9.1.1 Geometry Final Design

The geometry of the final model is shown in Figure 9-2 and summarized in Table 9-1. Figure 9-2 only shows half of one segment of the connection. Due to symmetry, it is sufficient to only model a segment in ANSYS. Therefore, the connection has been split in 16 segments in which one bolt is present, after which this segment has been split in half.

Table 9-1 - Geometry Details Final Model

Geometry detail	Size [mm]
outer diameter tube	914
outer diameter flange	1134
tube thickness	20
a	65
b	72
c	223
c'	197
t	80
b _D	50
b _E	32.5
R	447
bolt diameter	24
bolt hole diameter	26
washer diameter	44
height of bolt head	20
height of washer	4

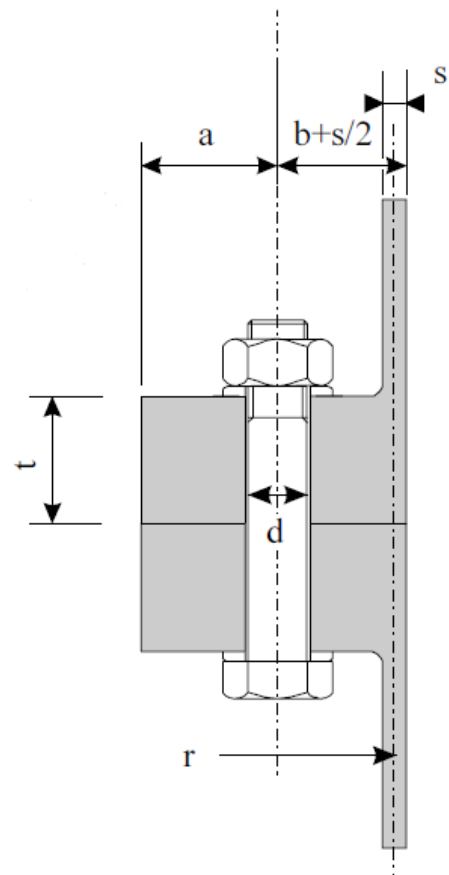


Figure 9-1 - Geometry Characteristics Bolted Flange Connection [24]

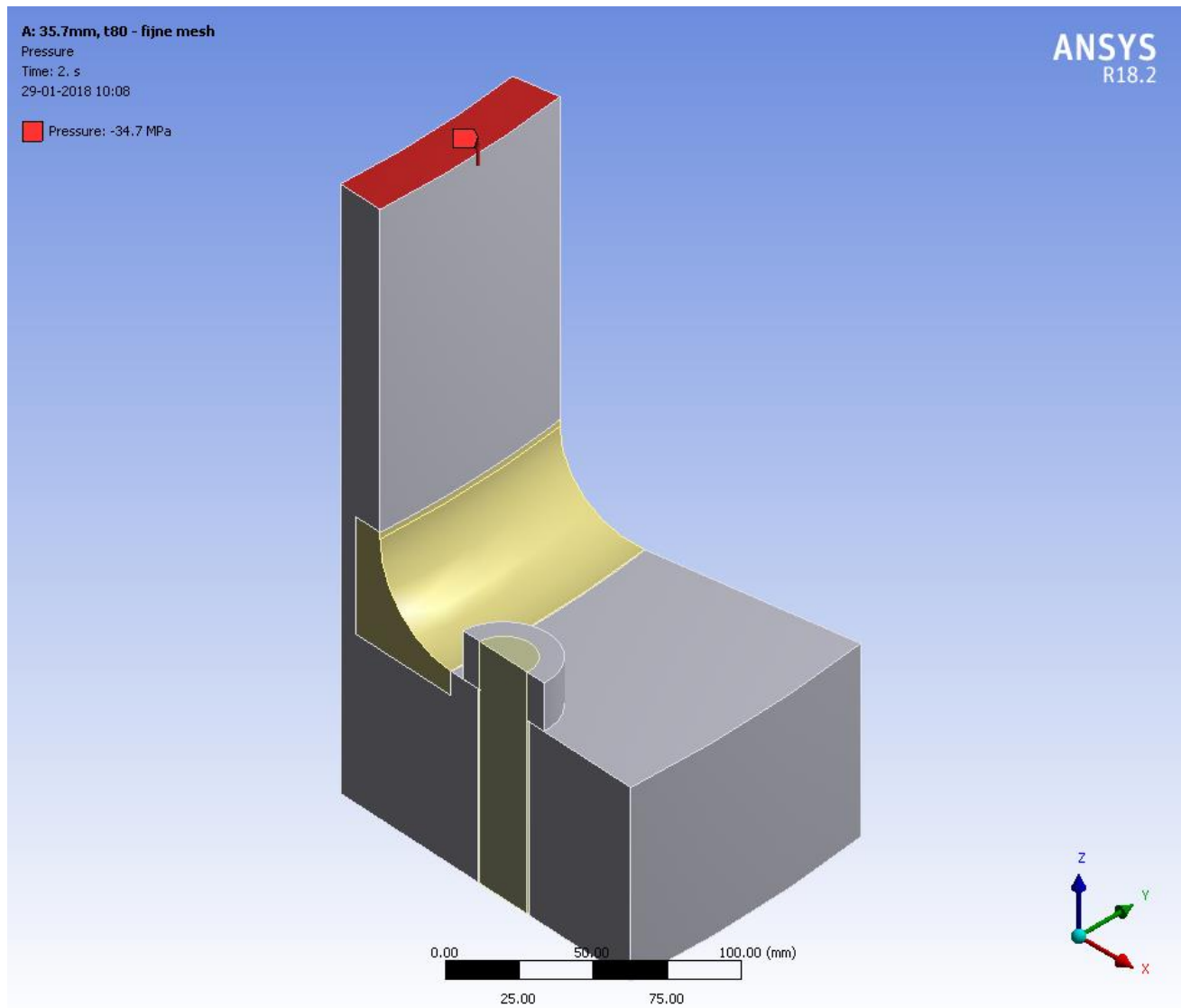


Figure 9-2 - Geometry Final Design

9.1.2 Fatigue Life Time

The fatigue life time has been improved compared to the initial geometry. This has been done by increasing the radius of the tube-to-flange junction. The fatigue life time of the tube-to-tube connection, which is categorized as structural detail 71, has a life time of 17 years. The tube-to-flange junction, which is categorized as structural detail 140, has a life time of 9 years. The MIF is expected to be used over a period of more or less 8 years. Both of the connections meet this life time requirement.

It has been found that the influence of the SCF on the lifetime is significant, and the SCF is highly dependent of the radius. It is found that the bigger the radius, the lower the SCF. The decreasing values for the SCF per optimized model resulted in a longer lifetime for the flange as a whole. The final SCF found has a value of 3.51.

9.1.3 Failure Modes

In order to be sure that the final design meets all strength requirements, the design has been checked with respect to the failure modes. The final design meets the requirements of all 3 failure modes of which failure mode B is governing. The final design meeting the requirements means that the design is safe to be implemented in the structure of the MIF.

9.2 Discussion

The initial geometry has been obtained using the rules stated by ir. M. Seidel. During the design of the initial geometry, not only the rules are of interest but also the installation process of the connection has to be taken into account. The tools used to fasten the bolts need to be able to fit between the bolt and the radius.

The fatigue life has been calculated to be 9 years. However, in this period of 9 years, the MIF will not be standing on the seabed all the time. The MIF will only be used during projects, which usually last for 2 to 3 months, with approximately 2 projects per year. This means that the calculated fatigue life time, which is based on full-time environmental loading, is a minimum value. In reality, it can be expected that it will take longer than the calculated 9 years for the connection to get crack initiations. Checking the connection regularly will avoid the initiations of cracks going unnoticed.

10 Conclusions and Recommendations

During this thesis the bolted flange connection between two members has been studied. First, a global load analysis has been done which resulted in the values of the internal loads per member. These loads have been used in the ANSYS finite element calculation, from which the SCF in the tube-to-flange junction was obtained. A fatigue analysis of the bolted flange connection has been done using the SCF. The initial geometry is optimized in order to get an optimum fatigue life time while still satisfying the failure modes. The following sections will discuss the conclusions and the recommendations that follow from the study.

10.1 Conclusions

The main focus of this thesis was to access the fatigue life of the bolted flange connection in order to optimize the radius between the flange and the tubular part of the flange. For the fatigue analysis of this thesis, only the flange has been observed. In order to get the lifetime of the complete connection and not only the flange, it is recommended to do a fatigue analysis of both the bolt and the flange. The radius between the flange and the tubular part of the flange has a value of 36 mm in the final design. All geometrical details of the final design are stated in Table 9-1.

The optimization of the flange has been done taking into account the failure modes, which are explained in chapter 7. The geometrical optimization of the flange is bounded by the unity checks of the failure modes. It can be concluded that for the final design failure mode B is governing: failure of the bolt and the formation of a plastic hinge in the shell. The unity check for the final design considering the governing failure mode B has a value of 0.82, which is well below 1, and therefore can be considered safe.

The element size of the mesh used in ANSYS for the determination of the SCF has a significant influence on the accuracy of the results. It can be clearly seen in Figure 8-11 that a coarser mesh results in less accurate SCF values. The mesh has been refined until the SCF values converged to a constant value of 3.51. The final chosen element size of the mesh is 0.625 mm. It can be concluded that the size of the mesh has a significant influence on the accuracy of the results. If the

mesh is not refined up to a constant value for the SCF, the results can't be considered being accurate.

The fatigue life has first been calculated for the initial geometry in which a radius of 5 mm was assumed, which resulted in a short life time of 0.8 years. The lifetime is increased by decreasing the value of the SCF. This was done by increasing the radius of the tube-to-flange junction. The first optimized model was designed with a radius of 26 mm which resulted in a lifetime of 2.4 years. The final model was designed with a radius of 36 mm which resulted in a satisfying lifetime of 9 years, see Figure 8-16 and Figure 8-17. It can be concluded that the value of the SCF has a significant influence on the fatigue analysis and therefore on the lifetime of the connection.

The fatigue analysis has been done for two details: the circumferential butt weld between the machined part and the tube and the radius between the tube and the flange. For the optimum shape of the radius, the butt weld would become governing for the fatigue life of the complete connection. For the circumferential butt weld, structural detail category 71 was used. However, due to the geometrical boundaries given by the failure modes, the radius between the flange and the tubular part of the flange is found to be governing. The structural detail category used for the radius has been derived using detail category 140 and by implementing the SCF. It is concluded that the fatigue life of the tube-to-flange junction is governing due to the implementation of the SCF to incorporate the effect of the radius.

10.2 Recommendations

Several recommendations regarding the fatigue analysis can be stated. First of all, for the fatigue analysis of this thesis, only the flange has been observed. In order to get the lifetime of the complete connection and not only the flange, it is recommended to do a fatigue analysis of both the bolt and the flange.

The wave scatter data provided by Seaway Heavy Lifting has been observed in one field of the North Sea only. If the fatigue analysis is used in case of another wave field, it is recommended to compare the wave scatter diagrams. The wave scatter diagram that is used in this thesis needs to be compared with the wave scatter diagram that will be used for the new case. If these are of comparable values, the fatigue analysis of this thesis can be used. Otherwise, the analysis needs to be modified in order to be accurate.

The fatigue analysis has only been done for the environmental loading: waves, wind and currents. The influences of the cyclic motions the MIF will undergo during transportation aren't taken into

account. It is recommended to take these motions into account, since they can have an influence on the fatigue life.

Seaway Heavy Lifting has experienced with other structures that the mudmats at the lower part of the MIF are sensitive to fatigue. Therefore, it is recommended to research the fatigue life of the mudmats as well in order to be able to determine the fatigue life of the complete structure.

11 Bibliography

- [1] Seaway Heavy Lifting, "Renewables," 2017. [Online]. Available: https://www.seawayheavylifting.com.cy/uploads/media/SHL015_Brochure_Renewables_DEF_WT_LOW.pdf. [Accessed 16 June 2017].
- [2] REN21, "Renewables 2016, global status report," Renewable Energy Policy Network for the 21st Century, Paris, 2016.
- [3] Global Wind Energy Council, "Global Wind Report, annual market update," Brussels, 2016.
- [4] WindEurope, "About us - History," 2017. [Online]. Available: <https://windeurope.org/about-us/history/>. [Accessed 19 June 2017].
- [5] IEA, "Energy Policies of IEA Countries - European Union," International Energy Agency, Paris, 2014.
- [6] European Commission, "Impact assessment for a 2030 climate and energy policy framework," European Commission, Brussels, 2014.
- [7] WindEurope, "The European Offshore Wind Industry - Key and Statistics 2016," WindEurope, Brussels, 2016.
- [8] WindEurope, "Wind Energy Today," 2017. [Online]. Available: <https://windeurope.org/about-wind/wind-energy-today/>. [Accessed 19 June 2017].
- [9] WindEurope, "Unleashing Europe's offshore wind potential - A new resource assessment," WindEurope, Brussels, 2017.
- [10] S.-P. Breton and G. Moe, "Status, plans and technologies for offshore wind turbines in Europe and North-America," *Renewable Energy*, pp. 646 - 654, 2008.
- [11] Z. Saleem, "Alternatives and modifications of monopile foundation or its installation technique for noise mitigation - Thesis," TU Delft, Delft, 2011.
- [12] Seaway Heavy Lifting, "Offshore Transportation and Installation Manual for Monopiles and Transition Pieces," Unpublished Report Seaway Heavy Lifting, Zoetermeer, 2016.
- [13] Seaway Heavy Lifting, "Vessels - Stanislav Yudin," 2017. [Online]. Available: <https://www.seawayheavylifting.com.cy/vessels/stanislav-yudin#>.
- [14] Seaway Heavy Lifting, "Vessels - Oleg Strashnov," 2017. [Online]. Available: <https://www.seawayheavylifting.com.cy/vessels/oleg-strashnov#>. [Accessed 19 June 2017].
- [15] DNV GL, Support Structures for Wind Turbines, Oslo: Det Norske Veritas Germanischer Lloyd, 2016.
- [16] The Nautical Institute, "Dynamic positioning," 19 June 2017. [Online]. Available: <http://www.nautinst.org/en/forums/dynamic-positioning/>.
- [17] International Maritime Organization, "Guidelines for Vessels with Dynamic Positioning Systems," International Maritime Organization, London, 1994.
- [18] Seaway Heavy Lifting, "Installation of Monopiles on Dynamic Positioning," Unpublished Report Seaway Heavy Lifting, Zoetermeer, 2014.
- [19] Seaway Heavy Lifting, "Dudgeon Monopile Trial Installation on DP," Unpublished Report Seaway Heavy Lifting, Zoetermeer, 2016.

- [20 Seaway Heavy Lifting, "Monopile Installation Frame for DP Operation," Unpublished Report
] Seaway Heavy Lifting, Zoetermeer, 2017.
- [21 MTHøjgaard, "Offshore - Uploads," 01 November 2013. [Online]. Available:
] [http://www.ewea.org/offshore2013/wp-content/uploads/exhibitor-prs/2013.11.01%20%20MT%20Hoejgaard%20-%20untapped%20XL%20monopile%20potential%20\(11-01-13-02-50-54\).pdf](http://www.ewea.org/offshore2013/wp-content/uploads/exhibitor-prs/2013.11.01%20%20MT%20Hoejgaard%20-%20untapped%20XL%20monopile%20potential%20(11-01-13-02-50-54).pdf).
- [22 H. -. Force, "Flange Bolting at Petrochemical Plants in Azerbaijan," Hi - Force, [Online].
] Available: <http://www.hi-force.com/en-uk/project-details/15/flange-bolting-at-petrochemical-plants-in-azerbaijan>. [Accessed 14 02 2018].
- [23 J. Wardenier, X. -L. Z. J. A. Packer and G. J. v. d. Vegte, Hollow Sections in Structural
] Applications, Zoetermeer: Bouwen met Staal, 2010.
- [24 M. Seidel, "Zur Bemessung geschraubter Ringflanschverbindungen von Windenergieanlagen,"
] Shaker, Aachen, 2001.
- [25 M. Couchaux, I. Ryan and M. Hjjaj, "Stress Concentration Factors for the Fatigue Design of
] Tubular Flange Connections," in *Nordic Steel Construction Conference*, Malmö , 2009.
- [26 Seaway Heavy Lifting, "Design Requirements Monopile Installation Frame - Proposed,"
] Unpublished Report Seaway Heavy Lifting, Zoetermeer, 2017.
- [27 DNV GL, Design of Offshore Wind Turbine Structure, Oslo: Det Norkse Veritas Germanischer
] Lloyd, 2013.
- [28 J. M. J. Journée, W. W. Massie and R. H. M. Huijsmans, Offshore Hydromechanics, Delft: Delft
] University of Technology, 2015.
- [29 International Organization for Standardization, Petroleum and Natural Gas Industries - Fixed
] Steel Offshore Structures - (ISO - 19902), Geneva: ISO, 2011.
- [30 DNV GL, Environmental Conditions and Environmental Loads, Oslo: Det Norkse Veritas
] Germanischer Lloyd, 2010.
- [31 S. Chandrasekaran and A. K. Jain, Ocean Structures - Construction, Materials and Operations,
] Abingdon: Taylor and Francis Group, 2017.
- [32 B. D. Chandler and J. B. Hinwood, "Combined Wave-Current Forces on Horizontal Cylinders,"
] Monash University, Clayton, 1982.
- [33 C.-C. Teng, "Hydrodynamic Forces on a Horizontal Cylinder Under Waves and Current,"
] Oregon State University, Oregon, 1983.
- [34 M. A. Chella, A. Tørum and D. Myrhaug, "An Overview of Wave Impact Forces on Offshore
] Wind Turbine Substructures," *Energy Procedia*, pp. 217 - 226, 2012.
- [35 O. M. Griffin, R. D. Peltzer and H. T. Wang, "Kinematic and Dynamic Evolution of Deep Water
] Breaking Waves," *Journal of Geophysical Research*, pp. 16,515-16,531, 1996.
- [36 European Committee for Standardization, Eurocode 3: Design of Steel Structures - Plated
] Structural Elements (EN - 1993-1-9), Brussels: CEN, 2006.
- [37 DNV-GL, "Fatigue Design of Offshore Steel Structures," Det Norske Veritas Germanischer
] Lloyd, Oslo, 2011.
- [38 Hydratight, "Why Tension?," 2017. [Online]. Available:
] <http://www.hydratight.com/en/products/tension/why-tension>. [Accessed 15 August 2017].
- [39 European Committee for Standardization , Eurocode 3: Design of Steel Structures - Design of
] joints (EN - 1993-1-8), Brussels: CEN, 2011.

- [40 J. S. Bendat and A. G. Piersol, *Random Data: Analysis and Measurement Procedures*, Hoboken: Wiley, 2010.
- [41 P. H. Taylor, H. Santo and Y. S. Choo, "Current Blockage: Reduced Morison Forces on Space Frame Structures With High Hydrodynamic Area, and in Regular Waves and Current," *Ocean Engineering*, pp. 11 - 24, 2013.
- [42 G. Z. Forristall and K. C. Ewans, "Worldwide Measurements of Directional Wave Spreading," *Journal of Atmospheric and Oceanic Technology*, pp. 440 - 469, 1998.
- [43 A. W. Nielsen, J. V. T. Sørensen, F. Schlütter and H. Bredmose, "Wave Loads on a Monopile in 3D Waves," ASME, New York, 2012.
- [44 O. T. Gudmestad and G. Moe, "Hydrodynamic Coefficients for Calculation of Hydrodynamic Loads on Offshore Truss Structures," *Marine Structures*, pp. 745 - 758, 1995.
- [45 GL Noble Denton, *Guidelines for Marine Lifting and Lowering Operations*, Loughborough: Noble Denton Group Limited, 2015.
- [46 K. K. Ling, C. Zhiqian, K. L. Jie, W. C. C. Chye, K. W. An and J. K. S. Hong, "Calculation of Dynamic Amplification Factor During Offshore Lifting," 3 January 2014. [Online]. Available: <https://nusit.nus.edu.sg/technus/hpc/calculation-dynamic-amplification-factor-offshore-lifting/>. [Accessed 4 July 2017].
- [47 B. Zafari, J. Qureshi, J. T. Mottram and R. Rusev, "Static and Fatigue Performance of Resin Injected Bolts for a Slip and Fatigue Resistant Connection in FRP Bridge Engineering," *Structures*, pp. 71 - 84, 2016.
- [48 J. Wardenier, *Hollow Sections In Structural Applications*, Delft: Delft University Press, 2000.
- [49 M. Veljkovic, C. Heistermann, W. Husson, M. Limam, M. Feldmann, J. Naumes, D. Pak, T. Faber, M. Klose, K.-U. Fruhner, L. Krutschinna, C. Baniotopoulos, I. Lavasas, A. Pontes, E. Ribeiro, M. Hadden, R. Sousa, L. d. Silva, C. Rebelo, R. Simoes and J. Henriques, "High-Strength Tower in Steel for Wind Turbines (HISTWIN)," European Union, Luxembourg, 2009.
- [50 Total Material, "Total Materia - 's Werelds Meest Uitgebreide Materiaal Database," August 2010. [Online]. Available: <http://www.totalmateria.com/page.aspx?ID=CheckArticle&site=kts&NM=280>. [Accessed 29 June 2017].
- [51 Subsea Worldnews, "Concept Design of Motion Compensated Piling Gripper," 09 2014. [Online]. Available: <http://subseaworldnews.com/wp-content/uploads/2014/09/TWD-Introduces-Concept-Design-of-Motion-Compensated-Piling-Gripper.jpg>. [Accessed 29 June 2017].
- [52 SteelConstruction, "Material Selection and Product Specification," [Online]. Available: http://www.steelconstruction.info/Material_selection_and_product_specification. [Accessed 28 June 2017].
- [53 Seaway Heavy Lifting, "Sheringham Shoal Photos," Unpublished Report Seaway Heavy Lifting, Zoetermeer, 2011.
- [54 Seaway Heavy Lifting, "Monopile Installation on DP - Alignment Meeting," Unpublished Report Seaway Heavy Lifting, Zoetermeer, 2014.
- [55 Seaway Heavy Lifting, "Installation of Monopiles on Dynamic Positioning," Unpublished Report Seaway Heavy Lifting, Zoetermeer, 2014.
- [56 Seaway Heavy Lifting, "Gwynt Y Môr," Unpublished Report Seaway Heavy Lifting, Zoetermeer, 2013.

- [57 Seaway Heavy Lifting, "Durations Sheringham Shoal," Unpublished Report Seaway Heavy Lifting, Zoetermeer, 2011.
- [58 R. Scharff and M. Siems, "Pushing the Limits - Mega Monopile Foundations for Off-Shore Wind Turbines," *Steel Construction*, pp. 178 - 185, 2013.
- [59 T. B. Quimby, "Basic Design Concepts - ASD vs. LRFD," 11 April 2014. [Online]. Available: <http://www.bgstructuralengineering.com/BGDesign/BGDesign05.htm>. [Accessed 29 June 2017].
- [60 Oil & Gas News, "Saudi Arabia Review," 2017. [Online]. Available: http://www.oilandgasnewsworldwide.com/Article/38899/Hi-Force_launches_SBT_bolt_tensioners. [Accessed 17 August 2017].
- [61 Norsok Standard , Compact Flanged Connections, Lysaker: Standards Norway, 2006.
- [62 N. A. P. M. and C. F. O. Sanguinetti, "Scale Model Tests of a Fishing Vessel in Roll Motion Parametric Resonance," Universidad Austral de Chile, Valdivia, 2006.
- [63 D. Y. C. Leung and Y. Yang, "Wind energy development and its invironmental impact: A review," *Renewable and Sustainable Energy Reviews*, pp. 1031 - 1039, 2011.
- [64 O. B. Leite, "Review of Design Procedures for Monopile Offshore Wind Structures," Universidade do Porto, Porto, 2015.
- [65 Y. Kurobane, J. A. Packer, J. Wardenier and N. Yeomans, Design Guide for Structural Hollow Section Column Connections, Köln: TÜV - Verlag GmbH, 2004.
- [66 Kongsberg Maritime AS, "Kongsberg K-Pos DP - Dynamic Positioning System," Kongsberg Maritime AS, Kongsberg, 2007.
- [67 B. Kato and R. Hirose, "Bolted Tension Flanges Joining Circular Hollow Section Members," *Journal of Constructional Steel Research*, pp. 79 - 101, 1985.
- [68 J. K. Kaldellis and D. Zafirakis, "The wind energy (r)evolution: A short review of a long history," *Renewable Energy*, pp. 1887 - 1901, 2011.
- [69 International Organization for Standardization, Petroleum and Natural Gas Industries - (ISO - 19901 - Part 5), Geneva: ISO, 2016.
- [70 L. H. Holthuijsen, *Waves in Oceanic and Coastal Waters`*, New York: Cambridge University Press , 2007.
- [71 A. M. Gresnigt and J. W. B. Stark, "Design of Bolted Connections with Injection Bolts," in *Connections in Steel Structures III* , Exeter, Pergamon, 1996, pp. 77 - 87.
- [72 J. W. Gooch, *Encyclopedic Dictionary of Polymers*, Atlanta: Springer, 2011.
- [73 GL Noble Denton, *Guidelines for Marine Transportations*, Loughborough: Noble Denton Group Limited, 2015.
- [74 European Committee for Standardization, *Weldable structural steels for fixed offshore structures - (EN - 10225)*, Brussels: CEN, 2009.
- [75 European Committee for Standardization, *Steel products with improved deformation properties perpendicular to the surface of the product - (EN - 10164)*, Brussels: CEN, 2004.
- [76 European Committee for Standardization, *Hot rolled products of structural steels - (EN - 10025)*, Brussels: CEN, 2004.
- [77 European Committee for Standardization, *Hot Finished Structural Hollow Sections of Non-Alloy*

-] and Fine Grain Steels, Brussels: CEN, 2006.
- [78 European Committee for Standardization, Flanges and Their Joints - Design Rules for
] Gasketed Circular Flange Connections, Brussels: CEN, 2014.
- [79 European Commission , "Research and Innovation," June 2009. [Online]. Available:
] http://ec.europa.eu/research/infocentre/article_en.cfm?id=/research/star/index_en.cfm?p=ss-histwin&item=Infocentre&artid=26973. [Accessed 18 August 2017].
- [80 DNV GL, Design of Offshore Steel Structures - General, Oslo: Det Norske Veritas
] Germanischer Lloyd, 2011.
- [81 Denso, "Denso Marine Piling Tape," Denso, Houston, 2017.
]
- [82 M. Couchaux, I. Ryan and M. Hjjaj, "Stress Concentration Factors for the Fatigue Design of
] Tubular Flange Connections," in *Nordic Steel Construction Conference*, Malmö, 2009.
- [83 B. Chabrolin and I. Ryan, "Tenue à la Fatigue des Pylônes de Remontées Mécaniques,"
] CTICM, Saint-Aubin, 1993.
- [84 L. P. Bouwman, "Het monteren, het injecteren en het demonteren van injectiebouten," TU Delft,
] Delft , 1972.
- [85 S. Bhattacharya, "Challenges in Design of Foundations for Offshore Wind Turbines,"
] *Engineering & Technology Reference*, pp. 1 - 9, 2014.
- [86 American Institute of Steel Construction, Specification for Structural Steel Buildings`, Chicago:
] AISC, 2010.
- [87 D. N. V. G. Lloyd, "Fatigue Design of Offshore Steel Structures," DNV GL, Oslo, 2011.
]
- [88 Seatower, "Seatower," Seatower, 2014. [Online]. Available:
] <http://market.ecosummit.net/c/Seatower>. [Accessed 6 February 2018].
- [89 Statoil, "Statoil," Statoil, May 2008. [Online]. Available:
] <https://www.statoil.com/en/news/archive/2008/05/22/hywindfullscale.html>. [Accessed 6 February 2018].
- [90 L. P. Eng., "Bolted Joints," Little P. Eng. , May 2017. [Online]. Available:
] <https://www.littlepeng.com/single-post/2017/05/18/Bolted-Joints>. [Accessed 7 February 2018].

12 Appendix

12.1 Design Loads MIF

12.1.1 Variable Loads

Variable loads are loads that vary in direction, position and magnitude during the period of consideration. These loads are related to operations and normal use of the installation. During installation, the maximum allowed inclination of the monopile is 0.5°. The inclination will cause a momentum. It is important to account for the load the momentum will exceed on the structure. [27]; [26]

12.1.1.1 Live Loads

For the design of walkways, stairs and platforms live load has to be applied in addition to the dead load. For the design of walkways and stairs, live loads on unoccupied areas is given to be a distributed load of 4 kN/m² and for the design of (storage) platforms, live loads on unoccupied areas is given to be a 5 kN/m² distributed load. [27]

12.1.2 Wave Loads

The follow sections state different parameters used for the determination and calculation of respectively the wave theory and wave loading.

12.1.2.1 Water Depths

The following design water depths are stated:

Table 12-1 - Design Water Depths

Description	Components	Water Depth [m]
Maximum Water Depth	Maximum mean seabed level [m Lowest Astronomical Tide]	42
Minimum Water Depth	Minimum seabed level [m Lowest Astronomical Tide]	20

Water depth is considered to be deep when the following condition is met:

$$d > \frac{\lambda}{2}$$

12-1

12.1.2.2 Wave Heights and Wave Periods

The wave heights and wave periods are stated for the operational state, the survival state and the standalone state of the MIF. The maximum wave height is obtained by multiplying the significant wave height with a factor 1.86. [40]

Table 12-2 - Wave Heights and Wave Periods

Description		Operational Condition	Survival Condition	Standalone Condition
Significant Wave Height H_s	[m]	2.50	3.50	6.00
Maximum Wave Height H_{max}	[m]	4.65	6.50	11.25
Wave Period T	[s]	6.90	8.20	7.50

12.1.2.3 Shallow Water Parameter

The values of the shallow water parameter have been calculated with the following formula:

$$\text{Shallow Water Parameter } \left[\frac{m}{s^2} \right] = \frac{d}{T^2} \tag{12-2}$$

The calculated values for the shallow water parameter are given in Table 12-3 for both the operational condition and the survival condition.

Table 12-3 - Values Shallow Water Parameter

Depth [m]	Operational Condition [m/s ²]	Survival Condition [m/s ²]	Standalone Condition [m/s ²]
20	0.42	0.30	0.36
42	0.88	0.62	0.75

12.1.2.4 Wave Steepness Parameter

$$\text{Wave Steepness Parameter } \left[\frac{m}{s^2} \right] = \frac{H_{max}}{T^2} \tag{12-3}$$

The values for the wave steepness parameter have been calculated with the following formula:

In Table 12-4 the values of the wave steepness parameter are given for the operational condition, the survival condition and the standalone condition.

Table 12-4 - Values Wave Steepness Parameter

Wave height [m]	Wave Steepness Parameter [m/s ²]
4.65	0.098
6.50	0.097
11.25	0.20

12.1.2.5 Determination of the Wave Theory per Load Case

On the horizontal axis of Figure 12-1 are the values drawn for the shallow wave parameter for the operational, survival and standalone conditions. On the vertical axis the values for the wave steepness parameter are drawn for the operational, survival and standalone conditions.

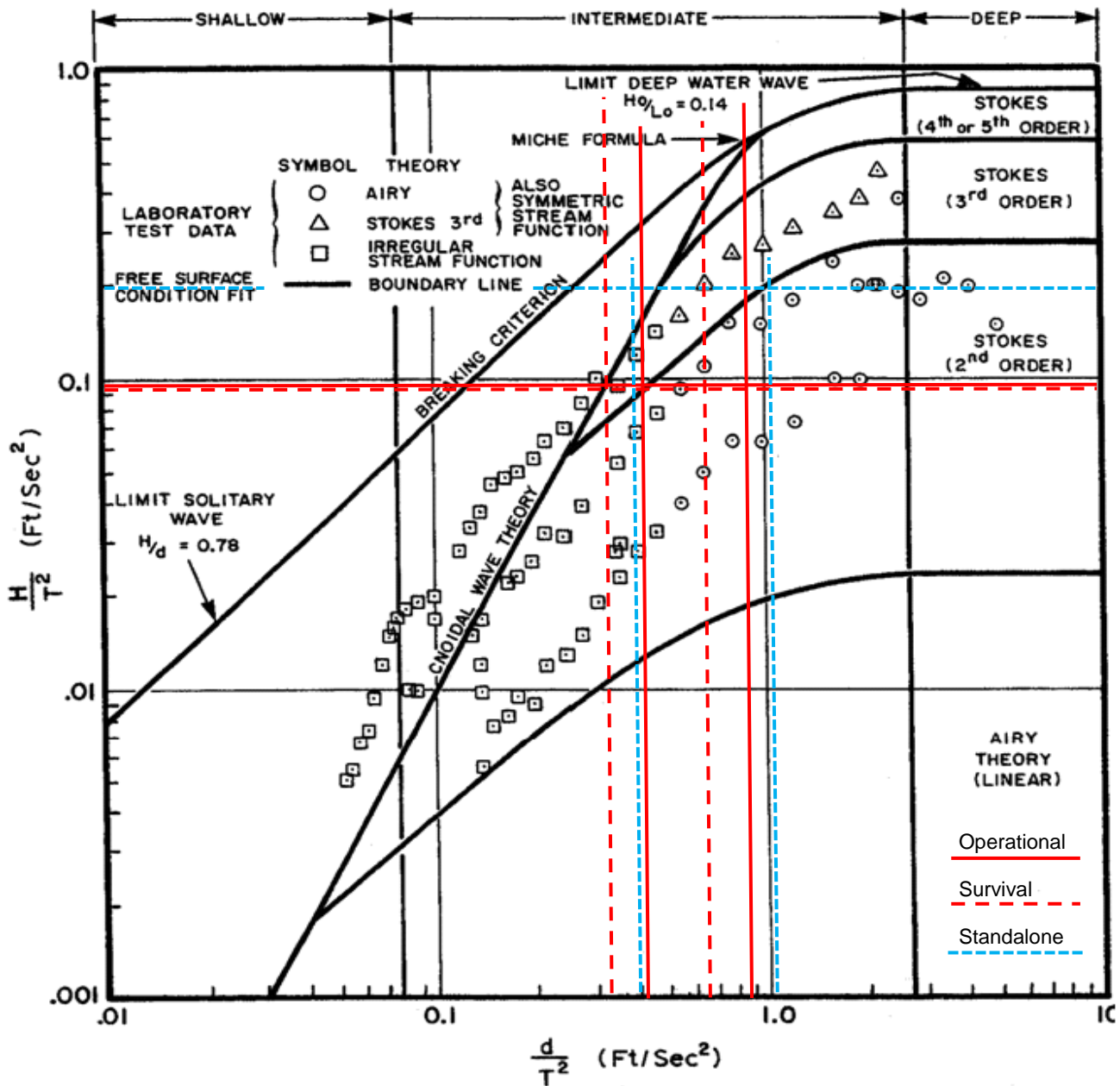


Figure 12-1 - Ranges of Validity for Various Wave Theories [30]

12.1.3 Morison's Load Formula Parameters

12.1.3.1 Particle velocity and acceleration

According to *Det Norske Veritas* the particle velocity and accelerations is as follows:

1. Particle velocity

$$u \left[\frac{m}{s} \right] = \frac{(\pi * H_{max})}{T} * e^{k*z} * \cos(\theta)$$

12-4

In which:

$$\theta = (k * x - \omega * t)$$

$$k \text{ [-]} = \text{wave number} = \frac{2\pi}{\lambda}$$

$$x \text{ [m]} = \text{distance of propagation}$$

$$\omega \left[\frac{rad}{s} \right] = \text{angular wave frequency} = \frac{2\pi}{T}$$

$$t \text{ [s]} = \text{time}$$

2. Particle acceleration

$$\frac{du}{dt} \left[\frac{m}{s^2} \right] = \frac{2 * \pi^2 * H_{max}}{T^2} * e^{k*z} * \sin(\theta)$$

12-5

12.1.3.2 Keulegan-Carpenter number

In some cases, it is not necessary to use both terms of Morison's Load Formula. In order to determine if both terms will be used or not the Keulegan-Carpenter number should be calculated.

$$\text{Keulegan - Carpenter number} = K - C = u * \frac{T}{D}$$

12-6

The following conditions are stated:

$K - C < 3$: The inertia force is dominant, drag can be neglected.

$3 < K - C < 15$: The drag can be linearized.

$15 < K - C < 45$: Both terms of the Morison Load Formula are important.

12.1.3.3 Current Blockage Factor

The Morison Load Formula takes into account both waves and currents. The standard method to calculate the total load is to sum up the load on each individual member of the structure, as if the rest of the structure is not present. Usually, the flow velocity used in the calculation of forces is taken to be the free stream current, measured at open sea. However, the structure will modify the flow field, so the calculation of forces with the free stream current velocity will lead to an overestimation of the peak loading. Therefore, a 'current blockage factor' has to be used in order to account for reduction of the flow velocity by flow divergence. [41]

The current blockage factor is given by:

$$\text{Blockage Factor } [-] = \frac{1}{1 + \left(\frac{\text{hydrodynamic area}}{4 * \text{frontal area}} \right)} \quad 12-7$$

In which:

$$\text{hydrodynamic area } [m^2] = 2 * \pi * r$$

$$r [m] = \text{radius}$$

$$\text{frontal area } [m^2] = D * d$$

12.1.3.4 Directional Wave Spreading Factor

The loads issued on a structure caused by waves may be reduced due to directional spreading of waves. This reduction is executed by applying a directional wave spreading factor in Morison's Load Formula. The directional wave spreading factor gives a measure of the degree of directional wave spreading in the wave spectrum and predicts the reduction in the particle velocities under waves due to directional spreading of the waves. [42]

The wave spreading factor is given by:

$$\varphi = \frac{\alpha_{aa}}{\alpha} \quad 12-8$$

In which:

$$\alpha_{aa} = \text{the velocity variance at zero lag}$$

$$\alpha = \text{the standard deviation of the velocity distribution in case of all waves coming from the one direction}$$

Typical values for the wave spreading factor for the North Sea are around 0.73 to 0.96, depending on location and wave height. An average value to use is therefore the mean value, which is 0.845. [42]; [43]

12.1.3.5 Inertia Coefficient

In order to calculate the wave loads with the Morison Load Formula the inertia coefficient have to be determined. The inertia coefficient can be calculated with the following formula:

$$C_m = 1 + C_A \quad 12-9$$

In which:

$$C_A [-] = \text{added mass coefficient} = \frac{m_a}{\rho * A}$$

$$m_a \left[\frac{kg}{m} \right] = \text{added mass per unit length}$$

$$A [m^2] = \text{cross - sectional area}$$

It is important to realize that when the design of the braces changes, i.e. the diameter changes, the inertia coefficient changes as well. A change in the diameter only causes a change in the area component of the inertia coefficient.

12.1.3.6 Drag Coefficient

In order to calculate the wave loads with the Morison Load Formula the drag coefficient has to be determined. For the MIF the following values are given:

Table 12-5 - Given Values C_d and C_m

Member type	Hydrodynamic drag coefficient C_d	Hydrodynamic inertia coefficient C_m
Smooth members	0.65	2.06
Rough members	1.05	1.2

The values given in Table 12-5 are said to be appropriate in the following cases:

- A steady current with negligible waves
- Large waves with:

$$\frac{(U_{m0} * T_{app})}{D} > 30 \quad 12-10$$

In which:

$$U_{m0} \left[\frac{m}{s} \right] = \text{maximum horizontal particle velocity at storm mean water level under the wave crest from a 2 - D wave kinematics theory}$$

$$T_{app} [s] = \text{apparent wave period}$$

$$D [m] = \text{Diameter member at storm mean water level}$$

It is important to realize that when the design of the braces changes, i.e. the diameter changes, the drag coefficients changes as well. The change in the drag coefficient is more elaborate than that in the inertia coefficient. The drag coefficient depends on the Reynolds number, which has to be recalculated. Therefore, an explanation of the determination of the drag coefficient is discussed in the following section. [30]; [44]

12.1.3.7 Determination C_d

The drag coefficient can be determined with the Reynolds number $[-]$, the diameter and the roughness of the member.

$$Re = \frac{u * D}{\nu} \quad 12-11$$

The Reynolds number is calculated as follows:

In which:

$$u \left[\frac{m}{s} \right] = \text{fluid particle velocity}$$

$$D [m] = \text{diameter of typical cross - sectional dimension}$$

$$\nu \left[\frac{m^2}{s} \right] = \text{kinematic viscosity of the fluid}$$

The following values are provided for the kinematic viscosity of sea water:

Table 12-6 - Kinematic Viscosities at Different Temperatures

Temperature [°C]	Kinematic viscosity ν [m ² /s]
0	1.83×10^{-6}
5	1.56×10^{-6}
10	1.35×10^{-6}
15	1.19×10^{-6}
20	1.05×10^{-6}
25	0.94×10^{-6}
30	0.85×10^{-6}

The values for the roughness of materials are given in the following table:

Table 12-7 - Surface Roughnesses

Material	k [m]
Steel, new uncoated	5×10^{-5}
Steel, painted	5×10^{-6}
Steel, highly corroded	3×10^{-3}
Concrete	3×10^{-3}
Marine Growth	$5 \times 10^{-3} - 5 \times 10^{-2}$

In order to determine the drag coefficient Figure 12-2 will be used.

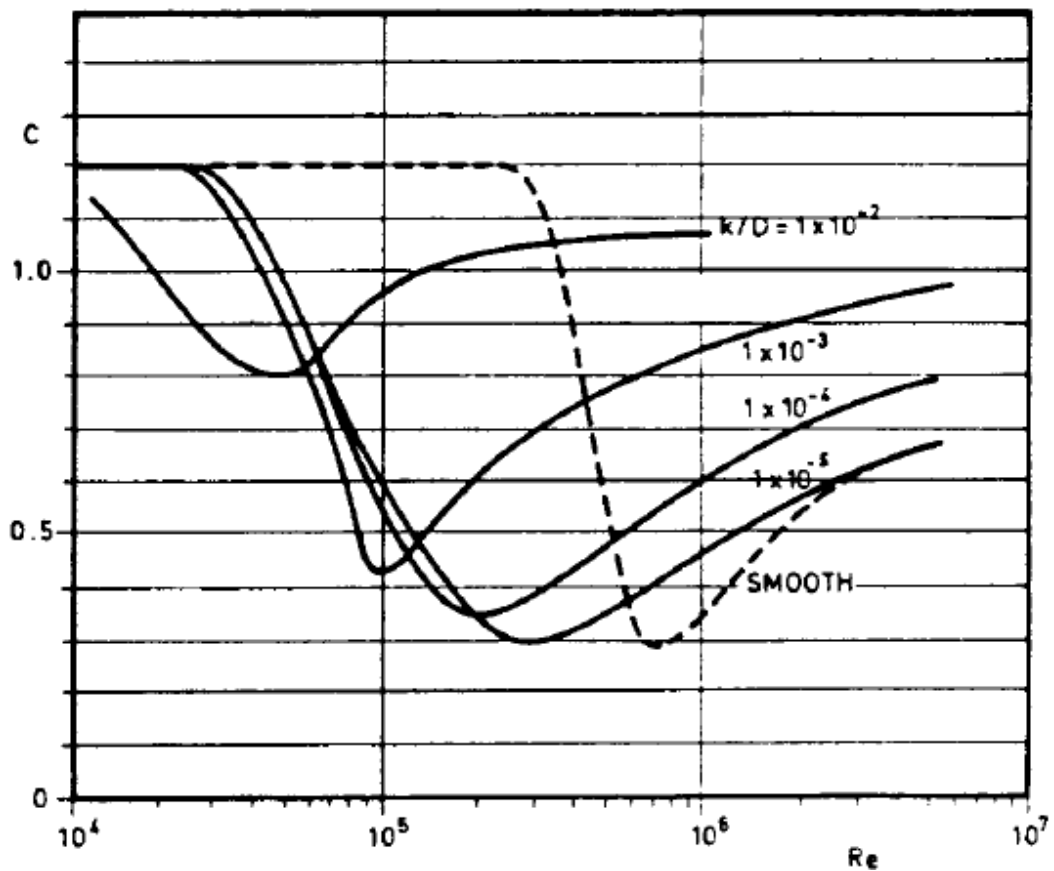


Figure 12-2 - Drag Coefficient for Fixed Circular Cylinder for Steady Flow in Critical Flow Regime for Various Roughnesses [30]

12.1.3.1 Second Order Stokes Wave Theory

The Stokes' wave theory is of use for non-linear, periodic surface waves. Assumed during the use of the Stokes' wave theory, is that the fluid layer has a constant mean water depth and that the fluid is inviscid. The Stokes' wave theory is accurate for small ratios of wave length to water depth. In shallow water, the Stokes' expansion will break down, which means it will give unrealistic values.

The surface elevation [m] for a second order Stokes wave is given by:

$$\eta(x, y, t) = \frac{H}{2} * \cos(\theta) + \frac{\pi * H^2}{8\lambda} * \frac{\cosh(k * d)}{\sinh^3(k * d)} * [2 + \cosh(2 * k * d)] * \cos(2\theta) \quad 12-12$$

In which:

$$\theta = k(x * \cos(\beta) + y * \sin(\beta)) - \omega t$$

$$k \left[\frac{rad}{m} \right] = wave\ number = \frac{2\pi}{\lambda}$$

The other used variables have been stated in the prior sections. In deep water the surface elevation [m] for a second order Stokes wave is given by:

$$\eta(x, y, t) = \frac{H}{2} * \cos(\theta) + \frac{\pi * H^2}{4\lambda} * \cos(2\theta) \quad 12-13$$

Second order Stokes waves are not symmetric, with a wave crest height (A_{crest}) higher than the wave trough (A_{trough}) height. The crests of Stokes waves are steeper than for Airy waves and the troughs of Stokes waves are wider than for Airy waves. The following formulas are stated for the crest and trough heights for deep water Stokes waves:

$$A_{crest} = \eta(\theta = 0) = \frac{H}{2} * \left(1 + \frac{\pi H}{2\lambda} \right) \quad 12-14$$


$$A_{trough} = |\eta(\theta = \pi)| = \frac{H}{2} * \left(1 - \frac{\pi H}{2\lambda} \right) \quad 12-15$$

12.1.4 Wind Loading

12.1.4.1 Shape Coefficient

The shape coefficients for a cylinder are given in Table 12-8. The value of shape coefficient is dependent of the value of the Reynolds number, of which the calculation has been described in 12.1.3.7. The kinematic velocity [m^2/s] of air is 1.45×10^{-5} when the air temperature is 15 °C.

Table 12-8 - Shape Coefficients [30]

Shape Coefficients C_s for Sphere-Shaped Structures		
	Boundaries	Shape coefficient C_s
	Sphere	
	$Re \leq 4.2 * 10^5$	0.50
	$4.2 * 10^5 < Re < 10^6$	0.15
	$Re \geq 10^6$	0.20

12.1.5 Lifting and Positioning Dynamic Loads

Lifting operations will be assessed while taking into account the ‘Noble Denton Guidelines for marine lifting and lowering operations’. [45]

During lifting operations offshore by the heavy lift vessels crane, the structure passes through the ‘splash-zone’. This passage causes the object to undergo heave and pitch motions due to hydrodynamic forces; see Figure 12-3. These motions cause the lifting strings to undergo motions of loosening and tightening. Motions of loosening and tightening can be expected while hoisting through the air and transport in the field. A dynamic amplification factor has to be applied to

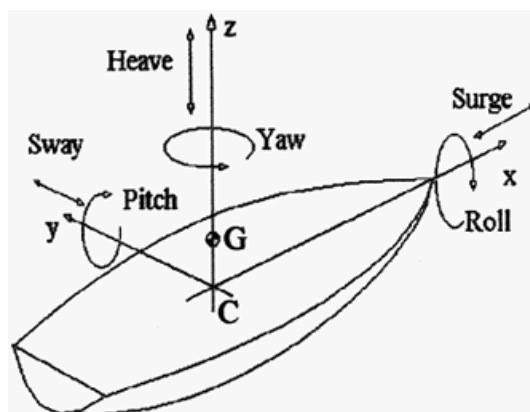


Figure 12-3 - Heave and Pitch [62]

account for these motions and in order to prevent snapping of hoisting lines. [46]

The dynamic amplification factor is the factor by which the gross weight is multiplied to account for accelerations and impacts during the lifting operation.

$$DAF = \frac{F_{total}}{m * g} \tag{12-16}$$

In which:

$$F_{total} [N] = \max ((F_{static-max} + F_{hyd}), (F_{static-max} + F_{snap}))$$

$$m [kg] = \text{mass of object in the air}$$

For the lifting operations, the following dynamic amplification factors will be considered:

Table 12-9 - Dynamic Amplification Factors [45]

Operation	Dynamic Amplification Factor
Lifting in the air	1.2
Lifting through splash zone	1.5
Lifting / Transport in field for repositioning	1.3

The environmental criteria for lifting through the splash zone shall be such that the dynamic amplification factor does not exceed 1.5.

Lifting analyses shall be performed for the design of the MIF for mobilization and demobilization as well as positioning and repositioning in the field. For the lift analyses and lift point designs the calculations have to include the following loads:

1. Dead loads (structure, ballast etc.)
2. Temporary steel works (guides and bumpers etc.)
3. Wet load (wet and filled structure weight)

The wet weight has to be applied for positioning and repositioning and in field transport. This includes the added weight due to wet buoyant members as well as all floated members weight.

12.1.1 Load Combinations

In this section the values per load combination are given.

12.1.1.1 Dead Load Case

The values for the dead load case are stated in Table 12-10. Since some member of the MIF will be buoyant when the MIF is placed on the seabed, a moment can be expected.

Table 12-10 - Dead Load

Dead Load					
Fx (kN)	Fy (kN)	Fz (kN)	Mx (kNm)	My (kNm)	Mz (kNm)
0	0	-4073.272	-0.213	-8886.582	0

12.1.1.2 Environmental Load Cases

The values for the different environmental load cases for the Operational Conditions, the Stand Alone Conditions and the Survival Conditions are stated in Table 12-11, Table 12-12 and Table 12-13.

Table 12-11 - Environmental Loads - Operational

Environmental Loads – Operational Conditions						
	Fx (kN)	Fy (kN)	Fz (kN)	Mx (kNm)	My (kNm)	Mz (kNm)
EN1	2709.89	2705.09	27.04	-82363.83	83112.78	198.25
EN2	3820.23	0	28.83	0	117942.63	-0.0023
EN3	1.483	3790.82	28.73	-115328.26	201.41	-851.03
EN4	-3777.09	0	54.037	0.01	-116177.48	0.0023

Table 12-12 - Environmental Loads - Stand Alone Conditions

Environmental Loads – Stand Alone Conditions						
	Fx (kN)	Fy (kN)	Fz (kN)	Mx (kNm)	My (kNm)	Mz (kNm)
EN1	3706.95	3709.04	54.14	-101634.93	102446.95	103.69
EN2	5248.97	0	62.99	0	145088.86	-0.0031
EN3	-1.80	5211.74	55.10	-142541.11	239.39	-1210.03
EN4	-5194.09	-0.0008	87.51	0.012	-142868.45	0.0031

Table 12-13 - Environmental Loads - Survival Conditions

Environmental Loads – Survival Conditions						
	Fx (kN)	Fy (kN)	Fz (kN)	Mx (kNm)	My (kNm)	Mz (kNm)
EN1	1405.87	1408.96	-79.84	-45434.07	47371.99	-617.22
EN2	2131.798	0	-32.89	-0.0016	71900.45	-0.012
EN3	-16.05	1840.93	-76.90	-57197.21	174.64	-3443.38
EN4	-2064.17	0	-106.34	0.0054	-70897.07	0.01

12.1.2 Load Combinations

The load combinations include both the dead load and the different environmental conditions and are stated in Table 12-14, Table 12-15 and Table 12-16.

Table 12-14 - Load Combinations - Operational Conditions

Load Combinations – Operational Conditions						
	F _x (kN)	F _y (kN)	F _z (kN)	M _x (kNm)	M _y (kNm)	M _z (kNm)
CM1	3522.852	3516.618	-4038.121	-107073.195	99160.031	257.720
CM2	4966.293	0	-4035.792	-0.213	144438.844	-0.003
CM3	1.928	4928.063	-4035.919	-149926.953	-8624.751	-1106.336
CM4	-4910.223	0	-4003.022	-0.200	-159917.297	0.003

Table 12-15 - Load Combinations – Stand Alone

Load Combinations – Stand Alone Conditions						
	F _x (kN)	F _y (kN)	F _z (kN)	M _x (kNm)	M _y (kNm)	M _z (kNm)
CM1	4819.030	4821.753	-4002.886	-132125.63	124294.453	134.793
CM2	6823.667	0	-3991.390	-0.213	179728.938	-0.004
CM3	-2.342	6775.259	-4001.645	-185303.66	-8575.379	-1573.036
CM4	-6752.314	-0.001	-3959.508	-0.197	-194615.56	0.004

Table 12-16 - Load Combinations - Survival Conditions

Environmental Loads – Survival Conditions						
	F _x (kN)	F _y (kN)	F _z (kN)	M _x (kNm)	M _y (kNm)	M _z (kNm)
CM1	1827.635	1831.645	-5491.296	-59064.496	52697.004	-802.384
CM2	2771.338	0	-5430.262	-0.214	84584.00	-0.015
CM3	-20.865	2393.213	-5487.481	-74356.578	-8659.551	-4476.397
CM4	-2683.427	0	-5525.742	-0.206	-101052.77	0.013

12.2 Model Verification

12.2.1 Chabrolin and Ryan

The method of Chabrolin and Ryan is based on the following formula:

$$SCF = 4.11 * \left(\frac{t_t}{6}\right)^{0.46} * \left(\frac{25}{t_f}\right)^{1.11} * \left(\frac{2*\pi*e}{n_b*243}\right)^{0.38} * \left(\frac{e-R}{56}\right)^{0.1} * \left(\frac{2R}{508}\right)^{0.21} \quad 12-17$$

12.3 ANSYS Model Details

Applied Loads:

Table 12-17 - Applied Loads to Model

Geometrical Part	Type of Loading	Magnitude Loading
Upper Flange	Compression – Tension	35 MPa
Bolt	Pretension	70600 N

Boundary conditions:

Table 12-18 - Boundary Conditions of Model

Geometrical Part	Boundary Condition
Sides of All Parts	Frictionless
Bottom Flange	Compression Only
Bottom Bolt	Fixed

The following mesh types and element sizes are used in the final model:

Table 12-19 - Used Mesh Types and Element Sizes

Geometrical Part	Mesh type	Element Size (mm)
Tube	Automatic	3.0
Flange	Automatic	3.0
Bolt	Sweep	1.0
Body of Radius	Sweep	0.625

12.4 Failure Modes

12.4.1 Validation Failure Modes Initial Geometry

In order to be sure the final model can be safely used in the MIF, it has to be checked with respect to the failure modes.

12.4.1.1 Geometry Initial Design

The design of the connection has been made based on a set size of the tube. The tube will have an outer diameter of 914 mm and the thickness of the shell of the tube will be 20 mm. For the final design, the bolt size, bolt quality and bolt number is set, which is respectively M24, 8.8 and 16.

12.4.1.2 Material Properties

The ultimate tensile strength (f_{ub}) of the bolt is 800 N/mm² and the yield strength (f_{yb}) is 640 N/mm², see Reference [1]. The tensile stress area of the M24 bolt is 353 mm². It is assumed that the bolt has been pre-tensioned with a pretension force of:

$$F_P = 0.5 * A_s * f_{ub} \approx 141200 \text{ N} \approx 141 \text{ kN}$$

The flange has a thickness of 80 mm, which results in a yield strength ($f_{y,flange}$) of 325 N/mm²; see Reference [2]. The shell of the tube has a thickness of 20 mm, which results in a yield strength ($f_{y,shell}$) of 355 N/mm².

12.4.1.3 Calculation Ultimate Force

For the different failure modes the ultimate force has been calculated which is stated in the following sections.

Failure Mode A

For failure mode A, the ultimate force is equal to:

$$F_{U,A} = F_{t,Rd} = \frac{0.9 * A_s * f_{ub}}{\gamma_{M2}} \approx 203000 \text{ N} \approx 203 \text{ kN}$$

Failure Mode B

The ultimate force for failure mode B can be determined with an iterative process or by substituting $M_{pl,3}$ into the ultimate force equation. In these calculations the latter has been chosen. The bending resistance of the shell has been substituted into the ultimate force equation.

$$\begin{aligned} F_{U,B} &= \frac{F_{t,Rd} * a + M_{pl,3}}{a + b'} \\ &= -\frac{N_{pl,Rd,shell}^2 * (a + b)}{2 * M_{pl,Rd,shell}} + N_{pl,Rd,shell} * \sqrt{1 + \frac{N_{pl,Rd,shell}^2 * (a + b)^2 + 4 * F_{t,Rd} * a * M_{pl,Rd,shell}}{4 * M_{pl,Rd,shell}^2}} \\ &\approx 175000 \text{ N} \approx 175 \text{ kN} \end{aligned}$$

Failure Mode C

The ultimate force that is determined for failure mode C is governing when the requirements of failure modes D and E cannot be met. For failure mode C, $M_{pl,3}$ has been substituted into the ultimate force equation.

$$F_U = \frac{M'_{pl,2} + M_{pl,3}}{b}$$

$$= \frac{N_{pl,Rd,shell}^2 * b}{2 * M_{pl,Rd,shell}} + \sqrt{\frac{(N_{pl,Rd,shell}^4 * b^2)}{4 * M_{pl,Rd,shell}^2} + \frac{M_{pl,Rd,flange,net} + M_{pl,Rd,shell}}{M_{pl,Rd,shell}} * N_{pl,Rd,shell}^2} \approx 1705000 \text{ N}$$

$$\approx 1705 \text{ kN}$$

Since the requirements of failure mode D have not been met, see following sections, failure mode C will be used in order to verify the connection.

Failure Mode D

In order to see whether failure mode C can be replaced by failure mode D, the stated requirements have been checked. The requirements can be checked after the ultimate force has been determined. The ultimate force has been determined by substituting $M_{pl,3}$ into the ultimate force equation.

$$F_{U,D} = \frac{M'_{pl,2} + \Delta M_{pl,2} + M_{pl,3}}{b'_D}$$

$$= -\frac{b'_D * N_{pl,Rd,shell}^2}{2 * M_{pl,Rd,shell}} + \frac{b'_D * N_{pl,Rd,shell}^2 * \sqrt{1 - 4 * \frac{M_{pl,Rd,shell}}{b'_D * N_{pl,Rd,shell}^2} * -\frac{M'_{pl,2} + \Delta M_{pl,2} + M_{pl,Rd,shell}}{b'_D}}}{2 * M_{pl,Rd,shell}}$$

$$\approx 1733000 \text{ N} \approx 1733 \text{ kN}$$

The requirements that need to be met have been checked:

- The full bending moment of the flange does not exceed $M_{pl,2}$ at mid-washer:

$$\left(\frac{F_{t,Rd}}{2} - F_{U,D}\right) * \frac{d_W + d_H}{4} \approx -28500000 \text{ Nmm} \approx -28.5 \text{ kNm}$$

$$M_{pl,2} - M'_{pl,2} \approx 11800000 \text{ Nmm} \approx 11.8 \text{ kNm}$$

The requirement is not met since: $\left(\frac{F_{t,Rd}}{2} - F_{U,D}\right) * \frac{d_W + d_H}{4} > M_{pl,2} - M'_{pl,2}$

- The reaction force r has to act on the flange:

$$\frac{(M'_{pl,2} + \Delta M_{pl,2})}{F_{t,Rd} - F_{U,D}} \approx -59 \text{ mm}$$

$$a = 70 \text{ mm}$$

Due to the relatively small ultimate force in the bolt, this requirement is met.

Failure Mode E

In order to see whether failure mode C can be replaced by failure mode E, the stated requirements have been checked. The requirements can be checked after the ultimate force has been determined. The ultimate force has been determined by substituting $M_{pl,3}$ into the ultimate force equation.

$$F_{U,E} = \frac{M_{pl,2} + M_{pl,3}}{b'_E}$$

$$= -\frac{b'_E * N_{pl,Rd,shell}^2}{2 * M_{pl,Rd,shell}} + \frac{b'_E * N_{pl,Rd,shell}^2 * \sqrt{1 - 4 * \frac{M_{pl,Rd,shell}}{b'_E * N_{pl,Rd,shell}^2} * -\frac{M_{pl,2} + M_{pl,Rd,shell}}{b'_E}}}{2 * M_{pl,Rd,shell}} \approx 2570000 \text{ N}$$

$$\approx 2570 \text{ kN}$$

The requirements that need to be met have been checked:

- The bending moment in the bolt axis does not exceed $M'_{pl,2}$:

$$\left(\frac{F_{t,Rd}}{2} - F_{U,E}\right) * \frac{d_W + d_H}{4} = -43200000 \text{ Nmm} = -43.2 \text{ kNm}$$

$$M_{pl,2} - M'_{pl,2} \approx 11800000 \text{ Nmm} \approx 11.8 \text{ kNm}$$

The requirement is met since: $\left(\frac{F_{t,Rd}}{2} - F_{U,E}\right) * \frac{d_W + d_H}{4} > M_{pl,2} - M'_{pl,2}$

- The reaction force r has to act on the flange:

$$\frac{(M'_{pl,2} + 2 * \Delta M_{pl,2})}{F_{t,Rd} - F_{U,E}} - \frac{d_W + d_H}{4} \approx -57 \text{ mm}$$

$$a = 70 \text{ mm}$$

Due to the relatively small ultimate force in the bolt, this requirement is met.

12.4.1.4 Verification Initial Geometry

The forces that are present in the ultimate load case have to be compared to the ultimate forces for each failure mode.

12.4.1.5 Ultimate Load Case

The ultimate load case for the monopile installation frame has been determined to be the operational load case. During this load case, the monopile is present within the installation frame. With help of the program 'SACS' a global load analysis has been done. From the global load analysis it was obtained that the values for the ultimate load case are as stated in Table 12-20.

Table 12-20 - Ultimate Load Case

F _{axial} [kN]	F _{y,z} [kN]	F _{total} [kN]
1504	443	1947

12.4.1.6 Unity Check

The initial design can be verified by performing a unity check between the actual forces present in the member and the ultimate forces for the different failure modes.

$$Unity\ Check = \frac{F_{actual}}{F_{ultimate}}$$

In which:

$$F_{actual} [kN] = 1947\ kN$$

$$F_{ultimate} [kN] = \text{Ultimate force for each failure mode}$$

The ultimate forces per failure mode are summarized in Table 12-21.

Table 12-21 - Ultimate Force per Failure Mode

Failure Mode	Ultimate Force [kN]
A	203
B	175
C	1705

The unity checks per failure mode are summarized in Table 12-22.

Table 12-22 - Unity Check per Failure Mode

Failure Mode	Unity Check [-]
A	0.60
B	0.70
C	0.07

From the unity check values in Table 12-22 it can be concluded that the strength requirements for the initial design of the connection are fulfilled. In this case failure mode A is the governing failure mode, which means failure of the bolt.

12.5 Fatigue Analysis

12.5.1 SCF Refinement

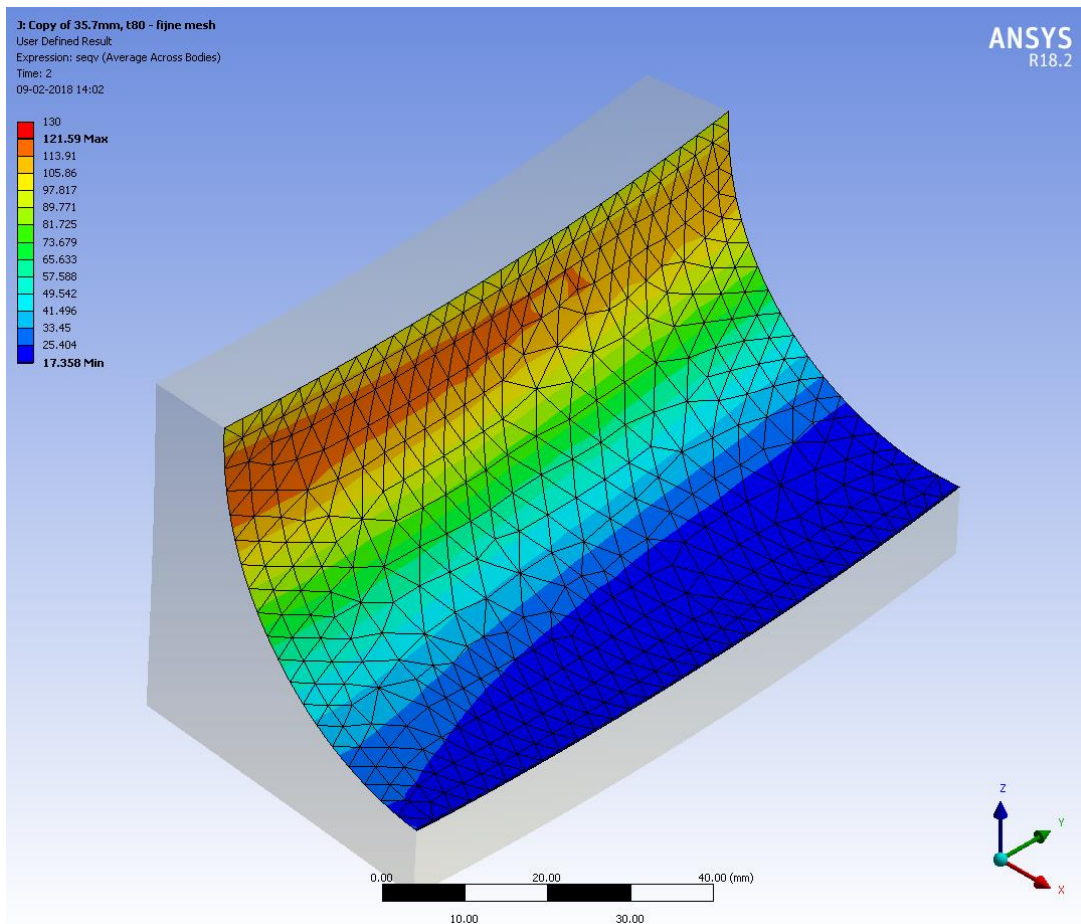


Figure 12-4 - Stress Distribution with Element Size of 5 mm

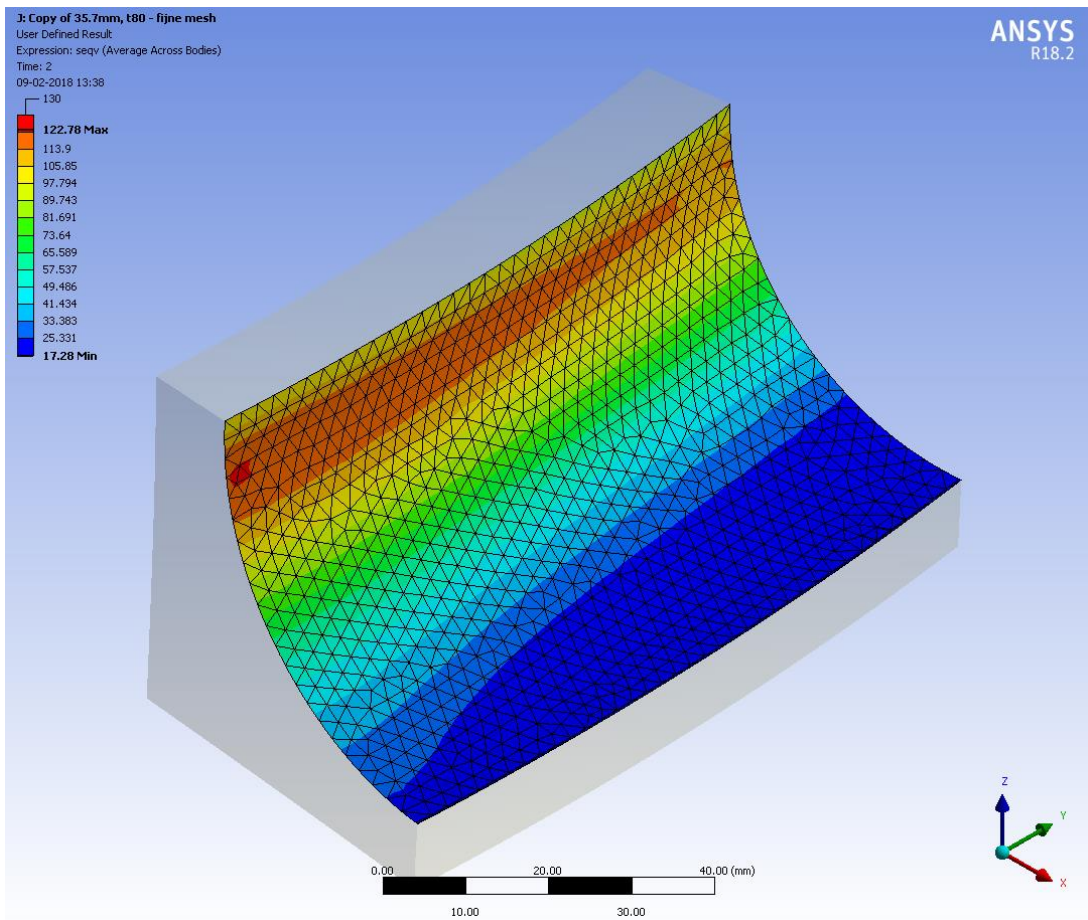


Figure 12-5 - Stress Distribution with Element Size of 2.5 mm

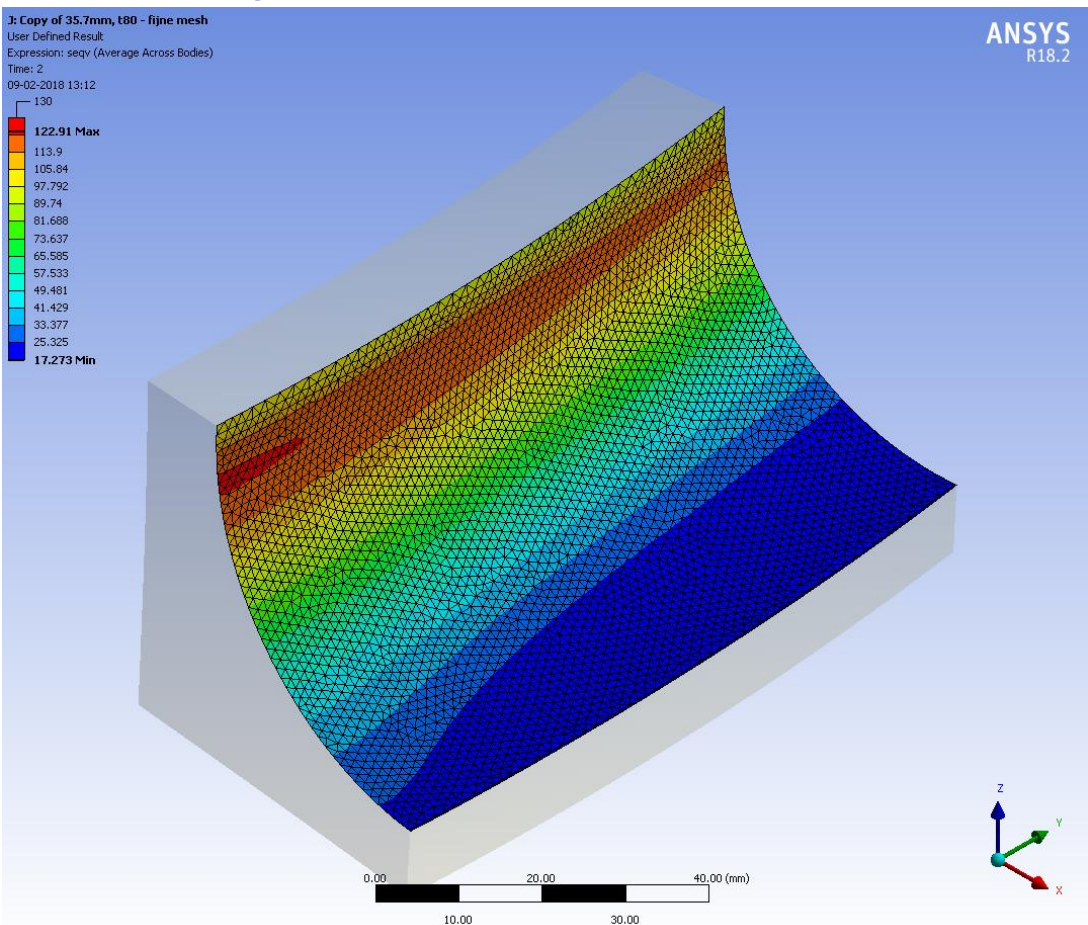


Figure 12-6 - Stress Distribution with Element Size of 1.25 mm

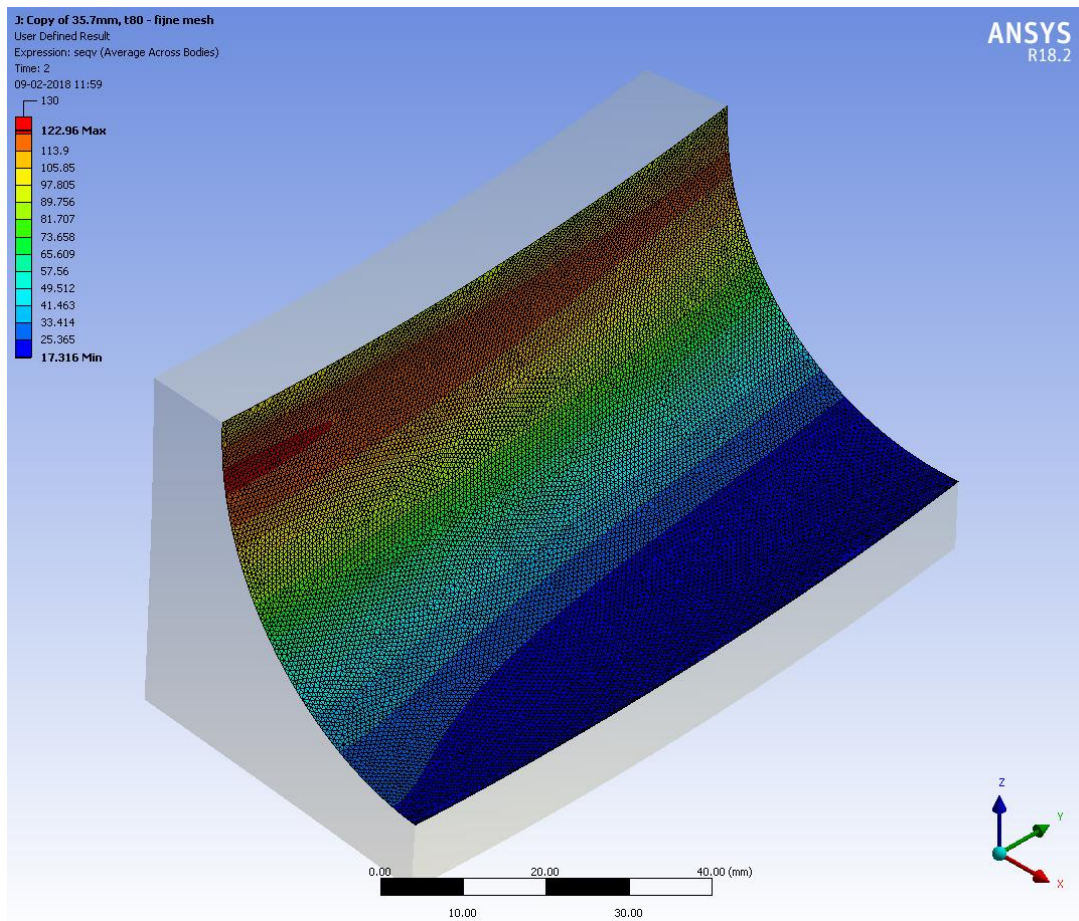


Figure 12-7 - Stress Distribution with Element Size of 0.625 mm

12.5.2 Wave Scatter Diagram

Wave Scatter diagram from 2000-2011, March-September, (53.26N, 138E)

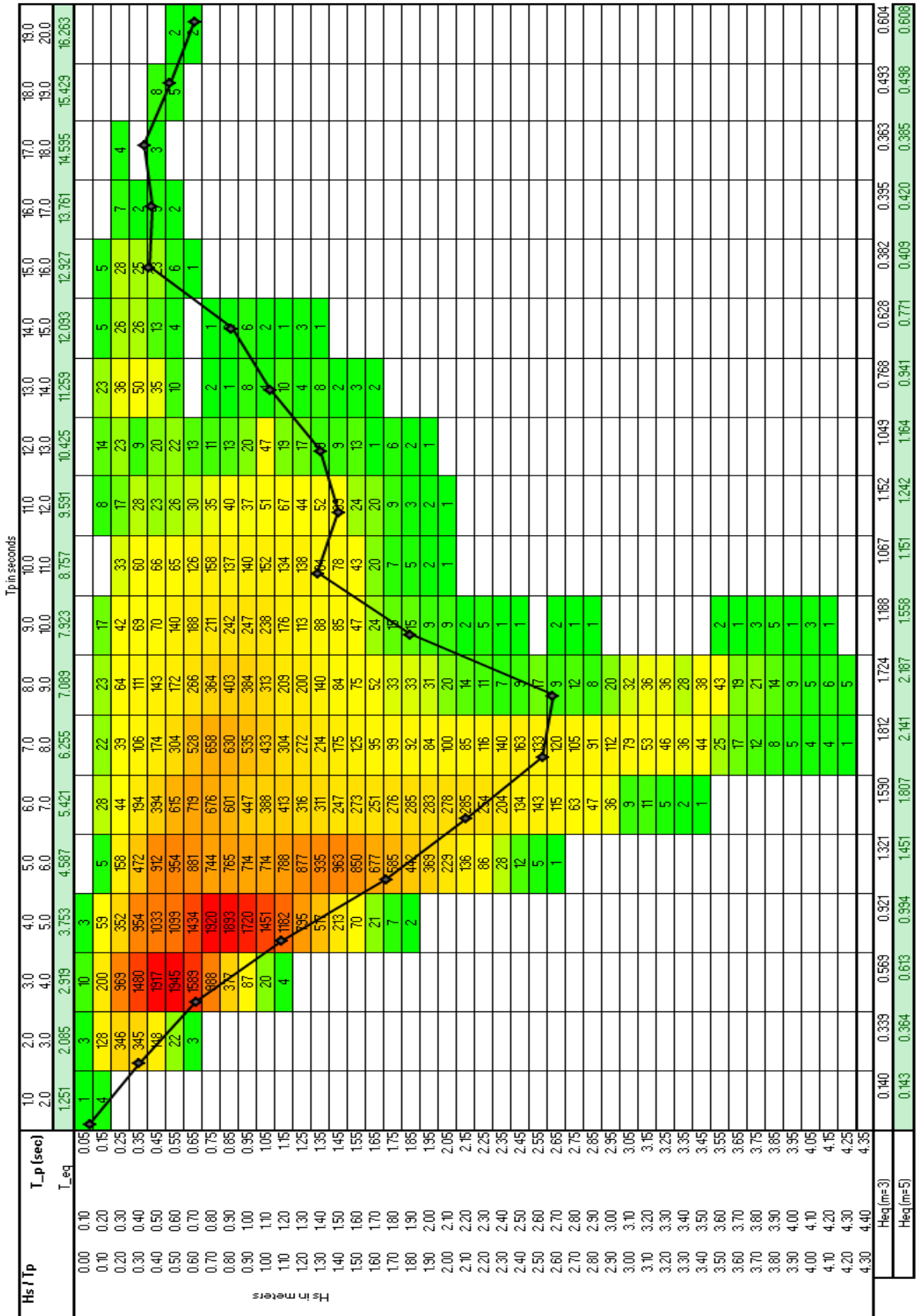


Figure 12-8 - Wave Scatter Diagram

12.5.3 Equivalent Wave Heights and Periods

Table 12-23 - Equivalent Wave Heights and Periods

Significant Height	Wave Period	Accumulative Cycles	Amount of
$H_s = 0.143\text{m}$	$T_p = 1.251\text{sec}$	5	
$H_s = 0.364\text{m}$	$T_p = 2.085\text{sec}$	995	
$H_s = 0.613\text{m}$	$T_p = 2.919\text{sec}$	9586	
$H_s = 0.994\text{m}$	$T_p = 3.753\text{sec}$	14725	
$H_s = 1.451\text{m}$	$T_p = 4.587\text{sec}$	13302	
$H_s = 1.807\text{m}$	$T_p = 5.421\text{sec}$	8348	
$H_s = 2.141\text{m}$	$T_p = 6.255\text{sec}$	6388	
$H_s = 2.187\text{m}$	$T_p = 7.089\text{sec}$	3519	
$H_s = 1.558\text{m}$	$T_p = 7.923\text{sec}$	2074	
$H_s = 1.151\text{m}$	$T_p = 8.757\text{sec}$	1449	
$H_s = 1.242\text{m}$	$T_p = 9.591\text{sec}$	556	
$H_s = 1.164\text{m}$	$T_p = 10.425\text{sec}$	269	
$H_s = 0.941\text{m}$	$T_p = 11.259\text{sec}$	198	
$H_s = 0.771\text{m}$	$T_p = 12.093\text{sec}$	90	
$H_s = 0.409\text{m}$	$T_p = 12.927\text{sec}$	88	
$H_s = 0.420\text{m}$	$T_p = 13.761\text{sec}$	16	
$H_s = 0.385\text{m}$	$T_p = 14.595\text{sec}$	7	
$H_s = 0.498\text{m}$	$T_p = 15.429\text{sec}$	13	
$H_s = 0.608\text{m}$	$T_p = 16.263\text{sec}$	4	
	Total	61632	

12.5.1 Example Calculation Lifetime

In order to clarify the above stated method of calculating the fatigue life, an example calculation is stated below. This has been done for the first equivalent load case: $H_{eq} = 0.143$ and $T_{eq} = 1.251$.

12.5.1.1 Structural Detail Category

The calculation will be done for both the tube-to-flange junction and the tube-to-tube junction, respectively detail category 140 and 71.

12.5.1.2 Stress Concentration Factor

As earlier stated in 8.3 the SCF for tensile stresses is 3.51 and the SCF for compression stresses is 0.5. This means that for detail category 140 the highest stress range that is found needs to be multiplied with a tensile SCF and a compression SCF. For detail category 71, no SCF is necessary.

12.5.1.3 Actual cycles

The actual amount of cycles happening during 6 months for the equivalent wave height of 0.143 meters is 5 cycles. This will have as a consequence that the damage of this wave height will be relatively low.

12.5.1.4 Stress Ranges

All member forces have been studied, after which one member is picked with the highest stress ranges. This case has 4 stress ranges because of the 4 different environmental load cases, see also 6.7.

The stress ranges including the SCF have been calculated as follows:

$$\sigma_{max} * SCF_{tension} - \sigma_{min} * SCF_{compression} =$$

$$20.25 * 3.51 - -15.99 * 0.5 = 79.07 \text{ MPa}$$

This has been done for all 4 environmental load cases. It can be seen that environmental load case 3 gives the highest stress range. Thus, for detail category 140 a stress range of 101.01 MPa will be used and for category 71 a stress range of 39.84 MPa.

Table 12-24 - Stress Ranges Example Case

Environmental Condition	σ_{max} [MPa]	σ_{min} [MPa]	Stress Ranges $\Delta\sigma$ without SCF	Stress Ranges $\Delta\sigma$ with SCF
EN1	20.25	-15.99	36.24	79.07
EN2	13.17	-16.75	29.92	54.47
EN3	27.03	-12.81	39.84	101.01
EN4	18.11	-9.03	27.14	67.90

12.5.1.5 Cycles to Failure

To calculate the cycles to failure, first the parameters $\log(a)$ and m need to be determined with help of Figure 8-14 and the known stress ranges. The values for $\log a$ and m are stated in Table 12-25.

Table 12-25 - Parameters S-N-Curve

Parameter	Detail Category 71	Detail Category 140
Log a	11.85	16.70
m	3	5

With the values known for $\log a$ and m , the amount of cycles to failure can be calculated as follows:

$$\log N = \log a - m * \log \Delta\sigma$$

$$N = 10^{\log a - m * \log \Delta\sigma}$$

For category 71, the amount of cycles until failure is then:

$$N = 10^{11.85 - 3 * \log(39.84)}$$

$$N = 11200000 \text{ cycles}$$

For category 140, the amount of cycles until failure is then:

$$N = 10^{16.70 - 5 * \log(101.01)}$$

$$N = 4770000 \text{ cycles}$$

12.5.1.6 Damage and Lifetime

The damage that occurs due to this equivalent wave can be calculated by dividing the actual amount of cycles occurring by the amount of cycles until failure.

$$Damage = \left(\frac{n_{actual}}{N_{failure}} \right)$$

In case structural detail 71 is observed, the damage in 6 months' time is:

$$Damage = \left(\frac{5}{11200000} \right) = 4.46 * 10^{-7} = 4.46 * 10^{-5} \% \text{ damage}$$

In case structural detail 140 is observed, the damage in 6 months' time is:

$$Damage = \left(\frac{5}{4770000} \right) = 1.05 * 10^{-6} = 1.05 * 10^{-4} \% \text{ damage}$$

For both detail categories the damage is very small. This will not have a significance influence on the lifetime.